# Statistical analysis of APXS-derived chemistry of the clay-bearing Glen Torridon region and Mount Sharp group, Gale crater, Mars

C. D. O'Connell-Cooper[1], L. M. Thompson[2], J. G. Spray[2], J. A. Berger[3], R. Gellert[4], M. McCraig[4], S. J. VanBommel[5], and A. Yen[6]

[1]University New Brunswick, NB, Canada
[2]University New Brunswick
[3]NASA Johnson Space Center: Houston
[4]University of Guelph
[5]Washington University
[6]Jet Propulsion Laboratory

November 24, 2022



## Abstract

The Glen Torridon stratigraphic sequence marks the transition from the low energy lacustrine-dominated Murray formation (Mf) (Jura member: Jm) to the more diverse Carolyn Shoemaker formation (CSf) (Knockfarril Hill member: KHm; Glasgow member: Gm), indicating a change in overall depositional setting. Alpha Particle X-ray Spectrometer (APXS) results and statistical analysis reveals that the bulk primary geochemistry of Mf targets are broadly in family with CSf targets, but with subtle compositional and diagenetic trends with increasing elevation. APXS results reveal significant compositional differences between Jm_GT and the stratigraphically equivalent Jura on Vera Rubin ridge (Jm_VRR). APXS data defines two geochemical facies (high-K or high-Mg) with a strong bimodal grain distribution in Jm_GT and KHm. The contact between KHm to Gm is marked by abrupt sedimentological changes but a similar composition for both. Away from the contact, the KHm and Gm plot discretely, suggesting a zone of common alteration at the transition and/or a gradual transition in provenance with increasing elevation in the Gm. APXS results point to a complex history of diagenesis within Glen Torridon, with increasing diagenesis close to the Basal Siccar Point unconformity on the Greenheugh pediment, and with proximity to the beginning of the clay sulfate transition. Elemental mobility is evident in localized enrichments or depletions of Ca, S, Mn, P, Zn, Ni. The highly altered Hutton interval, in contact with the unconformity on Tower butte, is also identified on Western Butte, indicating that the "interval" was once laterally extensive.

# Statistical analysis of APXS-derived chemistry of the clay-bearing Glen Torridon region and Mount Sharp group, Gale crater, Mars

C. D. O'Connell-Cooper[1*] L. M. Thompson[1], J. G. Spray[1], J. A. Berger[2], R. Gellert[3], M. McCraig[3], S. J. VanBommel[4], A. Yen[5]

[1]Planetary and Space Science Centre, University of New Brunswick, Fredericton, Canada

[2]NASA Johnson Space Center, Houston, TX, USA

[3]University of Guelph, Ontario, Canada

[4]Washington University, St Louis, MO, USA

[5]Jet Propulsion Laboratory, California Institute of Technology, Pasadena, CA, USA

Corresponding author: Catherine O'Connell-Cooper oconnell.cooper@unb.ca

Key points:

1. Alpha Particle X-ray Spectrometer data for Glen Torridon, Gale crater documents subtle compositional changes

2. Multiple episodes of alteration and diagenesis identified

3. Compositional similarities between Glen Torridon members confirms the highly localized nature of the Vera Rubin ridge alteration

Abstract

The Glen Torridon stratigraphic sequence marks the transition from the low energy lacustrine-dominated Murray formation (Mf) (Jura member: Jm) to the more diverse Carolyn Shoemaker formation (CSf) (Knockfarril Hill member: KHm; Glasgow member: Gm), indicating a change in overall depositional setting. Alpha Particle X-ray Spectrometer (APXS) results and statistical analysis reveals that the bulk primary geochemistry of Mf targets are broadly in family with CSf targets, but with subtle compositional and diagenetic trends with increasing elevation. APXS results reveal significant compositional differences between Jm_GT and the stratigraphically equivalent Jura on Vera Rubin ridge (Jm_VRR). APXS data defines two geochemical facies (high-K or high-Mg) with a strong bimodal grain distribution in Jm_GT and KHm. The contact between KHm to Gm is marked by abrupt sedimentological changes but a similar composition for both. Away from the contact, the KHm and Gm plot discretely, suggesting a zone of common alteration at the transition and/or a gradual transition in provenance with increasing elevation in the Gm. APXS results point to a complex history of diagenesis within Glen Torridon, with increasing diagenesis close to the Basal Siccar Point unconformity on the Greenheugh pediment, and with proximity to the beginning of the clay sulfate transition. Elemental mobility is evident in localized enrichments or depletions of Ca, S, Mn, P, Zn, Ni. The highly altered Hutton interval, in contact with the unconformity on Tower butte, is also identified on Western Butte, indicating that the "interval" was once laterally extensive.

**Plain Language Summary**

The MSL Curiosity rover traversed the Glen Torridon locale in Gale crater, Mars, finding evidence in the rocks of a change from a lake setting to a river setting, with increasing elevation through the rock record. Geochemical results from the Alpha Particle X-ray Spectrometer (APXS) confirm a slow change in composition over time as the sediments that formed the rock were laid down. Fluids percolated through the sediments, altering the composition, with localized enrichments of calcium, sulfur, manganese, phosphorus, sodium, zinc, nickel, which are now present as veins or small rectangular nodules and concentrations.

## 1. Introduction

The Mars Science Laboratory (MSL) rover *Curiosity* has been exploring Gale crater, Mars, since August 2012, with the primary mission to seek and characterize past habitable environments [Grotzinger et al., 2012]. Gale crater is a ~155km diameter impact crater, with a 5 km high central mound, Aeolis Mons, (informally known as Mount Sharp) [Milliken et al., 2010; Grotzinger et al., 2012; Golombek et al., 2012], forming close to the Noachian-Hesperian transition, c. 3.7 ± 0.1 Ga [Le Deit et al., 2013; Thomson et al., 2011]. The Mount Sharp Group encompasses a series of sedimentary siliciclastic rocks, deposited under predominantly fluvial and lacustrine conditions (Bradbury, Murray and Carolyn Shoemaker formations) [e.g., Grotzinger et al., 2014, 2015; Rice et al., 2017; Stack et al., 2019; Edgar et al., 2020; Fedo et al., 2020, this issue]. These deposits are overlain unconformably (along the Basal Siccar Point unconformity) by aeolian deposits of the Siccar Point Group [Stimson formation) [e.g., Banham et al., 2018, this issue; Bryk et al., 2019, 2020].

Since descending from the erosion-resistant Vera Rubin ridge (VRR) [e.g., Fraeman et al., 2020] in January 2019, *Curiosity* has been exploring the phyllosilicate unit or trough [Anderson and Bell, 2010; Fraeman et al., 2016], skirting along the edge of VRR in a topographical low (informally called “Glen Torridon”) (Figure 1) below the layered sulfate units identified from orbit [e.g., Milliken et al., 2010]. Glen Torridon comprises a series of units with an Fe/Mg smectite clay-rich spectral signature (orbitally defined, pre landing) [e.g., Fraeman et al., 2016; Milliken et al., 2010], a major objective of MSL’s primary mission, as clay minerals record fluid conditions and can enhance organic matter preservation [Summons et al., 2011]. The change from clay- to sulfate-rich conditions with increasing elevation indicates a fundamental shift in environmental and depositional across the boundary [Bibring et al., 2006; Milliken et al., 2010].

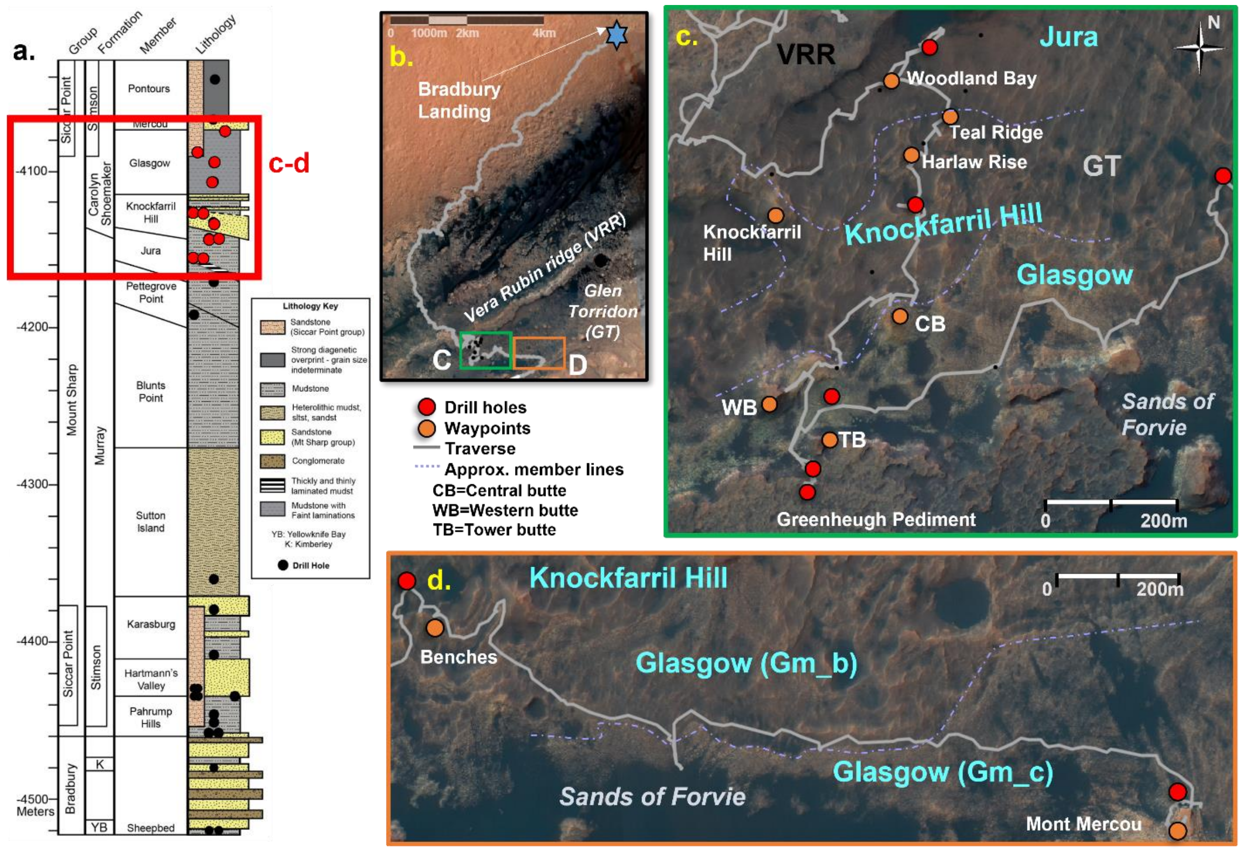


**Figure 1.** Stratigraphic column for Curiosity's traverse in Gale crater, Mars and localization maps. Stratigraphic column after Fedo et al., 2021, this issue. Base maps for images 1b-1d: High Resolution Stereo Camera (HiRise; on board the European Space Agency (ESA) Mars Express orbiter) orbital images of Gale crater, Mars. Image credit: NASA/JPL-Caltech.

**(1a)** Stratigraphic column for Gale crater highlighting in red the area covered by this study. Drill holes for the campaign (red circles) are (in sol order): Aberlady (AL); Kilmarie (KM); Glen Etive 1+2 (GE1+GE2); Hutton (HT); Edinburgh (EB): Glasgow (GG); Mary Anning 1+3 (MA1+MA3); Groken (GR); Nontron (NT). (**1b**)**.** Map of Gale crater, with rover traverse shown in grey, highlighting the study area in Glen Torridon, showing approximate member boundaries (purple dashed lines) between Jura, Knockfarril Hill and Glasgow members. (Fedo et al., this issue for detailed stratigraphic maps). **(1c)** Sols 2300-2921 comprises the descent from VRR to the MA and GR drill locales. **(1d)** Sols 2925-3072 comprises the post-MA traverse to the NT drill at the base of Mont Mercou. Glasgow member is subdivided into Gm_a, Gm_b and Gm_c, based on compositional variations defined herein (Section 4.3.1); subunit boundary (purple dashed line) in **1d.** after Hughes et al., this issue, 2021.

| | Formation | Member | Subunits[10] | Description | Drill targets | Location Notes | Other names | |
|---|---|---|---|---|---|---|---|---|
| Mount Sharp Group[1] | Murray (Mf)[1,3,4] | Jura[9] (Jura in study area = Jm_Gt)[10] | High-K facies | dominant morphology; mudstones; pebbles, some larger boulders and "rubble" | - | main clay-rich trough, lower most Glen Torridon | Phyllosilicate trough[15] phyllosilicate layers[16] phyllosilicate unit[2] Clay-bearing unit[19, 20] | Smooth claybearing unit (sCBU)[17,18] |
| | | | High-Mg facies | fine sandstone; "coherent" beds, in situ | *Aberlady* (AL) | | | |
| | | | | | *Kilmarie* (KM) | | | |
| | Carolyn Shoemaker (CSf)[5,6] | Knockfarril Hill (KHm)[5,6] | High-K facies | finer sandstones, layers within coarser bedrock | *Glen Etive 1* (GE1) *Glen Etive 2* (GE2) | overlying Jm_Gt, to Central butte, and edge of Western butte | | Fractured claybearing unit (fU)[17,18] |
| | | | High-Mg facies | dominant morphology: cross-stratified sandstone ridges and hills | *Mary Anning 1* (MA1) *Mary Anning 3* (MA3) *Groken* (GR) | | | |
| | | KHm to Gm | Benches[5,6] | series of resistant benches, with fine-grained pebbles, boulders etc | - | transition KHm to Gm | | - |
| | | Glasgow[5,6] | Gm_a, including buttes zone | finely laminated mudstones, abundant diagenetic features (veins, nodules) | *Glasgow* (GG) | Central, Western, Tower buttes & traverse to Mary Anning (MA) | | Intermediate fractured claybearing unit (fIU)[17,18] |
| | | | Gm_b | | - | post-MA, to base of Mont Mercou | | |
| | | | Gm_c | | *Nontron* (NT) | | | |
| | | | Gm_HT | "Hutton interval" - Zone of intense alteration, in contact with overlying Basal Siccar Point unconformity | *Hutton* (HT) | Top of Tower butte, in contact with overlying Basal Siccar Point unconformity[12,13] | | |
| Siccar Point Group[2] | Stimson (Sf)[7,8] | Stimson @ Greenheugh Pediment[12] | | Capping rock[11,13,14], above Basal Siccar Point unconformity | *Edinburgh* (EB) | Capping rock on Greenheugh Pediment | | |

**Table 1. Summary of units within Glen Torridon.**

[1]Grotzinger et al., 2015. [2]Fraeman at al., 2016. [3]Fedo et al., 2019. [4]Stack et al., 2019. [5]Bennet et al., this issue. [6]Fedo et al., this issue. [7]Banham et al., 2018. [8]Banham et al., 2021. [9]Edgar et al., 2020. [10]As defined herein. [11]Thompson et al., this issue. [12]Banham et al., this issue. [13]Bryk et al., 2019, 2020. [14]Malin & Edgett, 2000. [15]Anderson & Bell, 2010. [16]Milliken et al., 2010. [17]Stack et al., 2017. [18]Cofield et al., 2017. [19]Bennet et al., 2018. [20]Fox et al., 2018.

In this work, we present Alpha Particle X-ray Spectrometer (APXS) results for the Glen Torridon region. Section 2 places the Glen Torridon traverse in context with orbitally identified units and with in situ stratigraphically defined units. Section 3 gives details of the instrument, the data sets analyzed by APXS, and the statistical methodology used. Section 4 presents the analytical results across the traverse, which are discussed in section 5.

## 2. Context – orbital mapping and definition of units

The Glen Torridon region has been extensively mapped using orbital data, combining both morphology and spectral signature to define units [e.g., Fraeman et al., 2016; Hughes et al., 2021, this issue]. As part of the Glen Torridon campaign, unit definitions have been refined via in situ mapping and sedimentological analysis [e.g., Fedo et al., 2020, this issue; Bennet et al., 2018, this issue]. Table 1 relates the orbitally defined units to those defined by in situ (formations, members), and the geochemical sub-units as defined herein, based on APXS data.

The Glen Torridon campaign started with descent from the Vera Rubin ridge (VRR) (sol 2302) (Figure 1c) and ends (for the purposes herein) at the *Nontron* drill site, at the base of Mont Mercou (sol 3072) (Figure 1d). It encompasses three sedimentary members (Jura, Knockfarril and Glasgow) and marks the transition from the fluvio-lacustrine Murray formation (Mf) [e.g., Grotzinger et al., 2015; Fedo et al., 2019] to the more diverse Carolyn Shoemaker formation (CSf) [Bennet et al., this issue; Fedo et al., this issue].

The **Jura member** (**Jm**; Murray formation) within Glen Torridon (hereafter **Jm_GT**) (Section 4.1) is stratigraphically equivalent to the lacustrine Jura member on VRR (Jm_VRR) [Edgar et al., 2020; Fedo et al., 2020, this issue]. The Jm_GT is dominated by pebbly regolith, larger boulders, and rare flat lying patches of finely laminated mudstones (Figures S2a-d), interpreted to represent low energy lacustrine environments [Edgar et al., 2020; Caravaca et al., this issue]. Less commonly, there are coarser grained, continuous bedrock targets (Figure S10e), up to sandstone grain size [Rivera Hernandez et al., 2020a, 2020b; Minitti et al., 2020, 2021]. These are interpreted to have been deposited under higher energy conditions, such as a fluvial environment or a fluvially influenced lakeshore [Caravaca et al., this issue].

The base of the **Knockfarril Hill** mbr (**KHm**; Carolyn Shoemaker formation) marks the beginning of the Carolyn Shoemaker formation (CSf) [Bennet et al., this issue; Fedo et al., this issue] (Section 4.2). The KHm is dominated by hills, ridges and mesas (e.g., Knockfarril Hill, Teal ridge, Harlaw rise) (Figures S3a-b), extending (within the study area) to the lower elevations of Central and Western buttes (Figure 1c). Both finer-grained and coarser-grained facies are identified within KHm [Caravaca et al., this issue; Rivera Hernandez et al., 2020a, 2020b; Minitti et al., 2020, 2021]. Finer-grained targets are fine-grained mudstones to sandstone grain size, manifesting as rubble, pebbles and coherent layers within coarser beds (e.g., the Glen Etive drill locale) (Figures S3c-d). Cross stratification is identified in the coarser sandstones, indicating a change in depositional setting to a fluvial-dominated environment [Caravaca et al., this issue].

The **Glasgow** mbr (**Gm**; Carolyn Shoemaker formation) is characterized by thinly laminated sandstones, typically light-toned (Figures S4a-b, S6a-f) and with an abundance of diagenetic features, such as fracturing and nodules (rare to absent in the underlying KHm and Jm_GT) [Bryk et al., 2020; Fedo et al., 2019, this issue] (Section 4.3). The Gm stretches laterally from the buttes (Central, Western, Tower) to Mont Mercou (Figures 1c-d) lying stratigraphically above Knockfarril Hill (KHm) but below the layered sulfate unit [e.g., Milliken et al., 2020].

# 3. Instrumentation, data sets and statistical methodology

## 3.1. MSL Alpha Particle X-ray Spectrometer (APXS) instrumentation

The Canadian-built APXS instrument onboard MSL *Curiosity*, the third generation APXS on martian rovers, is used to determine elemental chemistry of both rock and unconsolidated materials (sand and soil), through a combination of X-ray fluorescence (XRF) and particle-induced X-ray emission (PIXE) [e.g., Gellert et al., 2006, 2015; Campbell et al., 2012; Grotzinger et al., 2012; VanBommel et al., 2016, 2017] [Supporting Information Text (S1)]. Six curium-244 ($^{244}Cm$) radionuclide sources located on the sensor head irradiate a given sample with alpha particles and X-ray radiation, resulting in characteristic X-rays from the target, which are used to derive a spectrum or histogram of detected energies [Gellert et al., 2006]. Peaks in the spectrum primarily correspond to element(s) present in the target, including major and minor elements with atomic number Z 11-26 (from sodium to iron), and select trace elements (including Ni, Zn, Br). Data are presented as elemental concentrations (in wt% oxide, wt% element, or μg/g), with 2σ statistical precision error [Gellert et al., 2006] [Supporting Information Text (S1)].

## 3.2 APXS Sample sets

This study presents compositional data from bedrock targets, diagenetic features, and Glen Torridon drill fines, as analyzed by APXS (Tables 2a-b; Supplementary data file Table S1). Bedrock samples include “as-is” unbrushed targets and targets largely cleared of dust, via brushing with the arm-mounted Dust Removal Tool (DRT). Features such as veins and nodules are analyzed routinely to monitor potential changes in diagenetic conditions. These features are listed in Tables 2a-b, S1, but not included in bedrock averages. Where individual targets are discussed in the text below, the name is given in italics followed by the sol of acquisition.

Ten targets were drilled in Murray and Carolyn Shoemaker formation bedrock during the Glen Torridon campaign (Section 4.6) (Figs. 1a, S1; Table 2a-b). Drill fines include “tailings” samples (generated by the drilling process) and “DBA” (dumped) samples, the latter of which are equivalent to material analyzed by the MSL CheMin X-ray diffraction (XRD) system used to determine phase crystallography and mineralogy [Blake et al., 2013]. Table 2b lists the highest quality drill fines for each target, based on standoff from (i.e., distance above) fines, length of integration, percentage of fines in APXS FOV (field of view), and the highest quality host bedrock measurement [see Berger et al., 2020 for more discussion on drill fine evaluation].

**Table 2.** APXS compositional data for Glen Torridon, sol 2304 to sol 3072. All data reported as wt. % except Ni, Zn, Br (ppm). Errors, elevation, location data are compiled in Table S1 (Supplementary Data). Stimson formation, Greenheugh pediment (sols 2694-2733) in Thompson et al., this issue.

(**2a**) All targets, grouped by formation, member and date. [1]Target names correspond to PDS names. [2]Sol = a martian solar day has a mean period of 24 h, 39 min, and 35.244 s and is referred to as a sol. [3]Target type: R=Rock; RT=regolithic pebble-sand mix; F=(drill) fines; V=vein; N=nodule; Ft=float; SL=soil; SD=Sand. [4]Mean Mf+CSf=mean Murray and Carolyn Shoemaker formation, average based on 488 targets (Supplementary Text S2 for discussion). [5]Average basaltic soil (ABS), average based on 90 APXS soil analyses from Gale crater (MSL), Gusev Crater (Spirit Rover, Mars Exploration Rover-A) (MER-A) and Meridiani Planum (Opportunity Rover, MER-B) [O’Connell-Cooper et al., 2017].

(**2b**) Recommended drill fines and associated host bedrock targets. Targets assessed on FWHM (i.e., Full Width Half Maximum, measure of data quality), lifetime length, distance from target and target coverage (for fines). [2]Target type: R=Rock; F-DT=tailings fines; F-DBA=fines.

**Table 2a.**

| Target[1] | Sol[2] | Type[3] | $SiO_2$ | $TiO_2$ | $Al_2O_3$ | $Cr_2O_3$ | MnO | FeO | MgO | CaO | $Na_2O$ | $K_2O$ | $P_2O_5$ | $SO_3$ | Cl | Ni | Zn | Br |
|---|---|---|---|---|---|---|---|---|---|---|---|---|---|---|---|---|---|---|
| **Mean Mf+CSf (n=488)[4]** | 720-3072 | | 47.88 | 1.06 | 9.07 | 0.32 | 0.22 | 18.88 | 5.74 | 4.39 | 2.49 | 0.90 | 0.94 | 6.48 | 1.26 | 873 | 1370 | 334 |
| **Average basaltic soil (ABS)[5]** | | SL | 45.44 | 0.95 | 9.68 | 0.38 | 0.35 | 17.39 | 8.23 | 6.62 | 2.71 | 0.46 | 0.88 | 6.09 | 0.69 | 476 | 293 | 62 |
| **Murray formation: Jura (Glen Torridon) member (Jm_Gt)** | | | | | | | | | | | | | | | | | | |
| St. Fergus | 2304 | R | 47.83 | 1.15 | 9.27 | 0.33 | 0.11 | 21.42 | 4.91 | 3.61 | 2.46 | 1.33 | 0.77 | 5.37 | 1.13 | 981 | 1031 | 27 |
| Brent_1 | 2308 | RT | 48.27 | 1.06 | 9.52 | 0.37 | 0.15 | 22.01 | 5.76 | 3.90 | 2.63 | 1.09 | 0.64 | 3.48 | 0.77 | 674 | 749 | 26 |
| Brent_raster2 | 2308 | RT | 47.37 | 1.10 | 9.36 | 0.42 | 0.23 | 21.50 | 6.68 | 4.55 | 2.61 | 0.87 | 0.72 | 3.62 | 0.75 | 678 | 690 | 35 |
| Brent_raster3 | 2308 | RT | 47.04 | 1.09 | 9.52 | 0.47 | 0.24 | 21.10 | 6.98 | 4.98 | 2.67 | 0.86 | 0.73 | 3.46 | 0.68 | 612 | 512 | 12 |
| Isbister | 2311 | RT | 45.75 | 0.94 | 8.77 | 0.44 | 0.22 | 21.87 | 7.02 | 4.51 | 2.71 | 0.87 | 0.64 | 4.75 | 1.10 | 723 | 756 | 513 |
| Emerald_centre | 2315 | RT | 48.27 | 1.13 | 9.32 | 0.35 | 0.12 | 20.03 | 5.66 | 3.96 | 2.57 | 1.19 | 0.72 | 4.98 | 1.39 | 767 | 948 | 342 |
| Emerald_raster1 | 2315 | RT | 48.04 | 1.12 | 9.30 | 0.36 | 0.12 | 20.03 | 5.83 | 4.02 | 2.60 | 1.16 | 0.72 | 5.04 | 1.37 | 780 | 926 | 371 |
| Emerald_raster2 | 2315 | RT | 50.30 | 1.13 | 9.50 | 0.33 | 0.11 | 20.38 | 5.14 | 3.16 | 2.68 | 1.29 | 0.65 | 3.87 | 1.17 | 798 | 981 | 295 |
| Curlew_DRT | 2318 | R | 45.01 | 1.13 | 9.03 | 0.34 | 0.22 | 17.94 | 6.83 | 5.38 | 2.73 | 0.81 | 0.76 | 7.29 | 2.12 | 660 | 2245 | 375 |
| Gannet | 2318 | R | 43.94 | 1.08 | 8.78 | 0.33 | 0.22 | 18.34 | 6.70 | 5.94 | 2.50 | 0.70 | 0.75 | 8.50 | 1.82 | 674 | 2333 | 231 |
| Ladder_Hills | 2320 | R | 46.18 | 1.21 | 9.21 | 0.32 | 0.24 | 17.57 | 6.53 | 5.39 | 2.68 | 0.75 | 0.72 | 6.77 | 1.95 | 682 | 2196 | 319 |
| Alloa | 2333 | R | 41.36 | 0.95 | 8.51 | 0.26 | 0.29 | 17.28 | 6.99 | 6.64 | 2.51 | 0.63 | 0.89 | 11.47 | 1.80 | 672 | 1514 | 287 |
| Auchterarder | 2333 | R | 40.43 | 0.92 | 8.09 | 0.25 | 0.30 | 15.93 | 6.37 | 8.33 | 2.49 | 0.58 | 0.82 | 13.21 | 1.80 | 568 | 1503 | 505 |
| Fife | 2347 | R | 48.66 | 1.16 | 9.07 | 0.39 | 0.20 | 19.86 | 6.92 | 3.81 | 2.46 | 0.82 | 0.71 | 3.99 | 1.47 | 878 | 2466 | 387 |
| Arbuthnott_DRT | 2349 | R | 44.33 | 1.08 | 8.21 | 0.32 | 0.21 | 16.59 | 6.39 | 6.88 | 2.27 | 0.73 | 0.74 | 10.26 | 1.52 | 723 | 2202 | 578 |
| Caledonia_centre | 2349 | RT | 46.82 | 1.12 | 8.94 | 0.45 | 0.22 | 21.56 | 6.86 | 4.38 | 2.56 | 0.91 | 0.75 | 3.93 | 1.18 | 725 | 875 | 901 |
| Caledonia_left | 2349 | RT | 44.94 | 1.23 | 8.62 | 0.53 | 0.30 | 21.59 | 7.64 | 5.41 | 2.44 | 0.70 | 0.79 | 4.61 | 0.95 | 696 | 633 | 649 |
| Caledonia_right | 2349 | RT | 44.30 | 1.02 | 8.82 | 0.58 | 0.41 | 20.73 | 9.21 | 6.78 | 2.54 | 0.49 | 0.59 | 3.72 | 0.63 | 658 | 476 | 118 |
| Crieff | 2352 | R | 49.89 | 0.91 | 9.16 | 0.33 | 0.12 | 19.93 | 6.02 | 3.16 | 2.61 | 1.09 | 0.66 | 3.57 | 1.82 | 869 | 1310 | 1209 |
| Snorre | 2356 | R | 48.49 | 1.12 | 8.70 | 0.33 | 0.11 | 20.30 | 5.39 | 3.90 | 2.52 | 1.08 | 0.77 | 5.41 | 1.45 | 829 | 859 | 1587 |
| Stonebriggs_centre | 2356 | RT | 46.74 | 1.14 | 8.76 | 0.37 | 0.26 | 21.54 | 6.99 | 4.41 | 2.70 | 0.91 | 0.78 | 4.03 | 1.08 | 880 | 894 | 441 |
| Stonebriggs_left | 2356 | RT | 46.86 | 0.90 | 9.14 | 0.45 | 0.20 | 21.68 | 6.99 | 4.04 | 2.45 | 0.86 | 0.81 | 4.11 | 1.05 | 751 | 1180 | 479 |
| Stonebriggs_right | 2356 | RT | 46.19 | 0.98 | 8.74 | 0.41 | 0.24 | 21.84 | 7.23 | 4.61 | 2.58 | 0.81 | 0.85 | 4.08 | 0.99 | 703 | 881 | 414 |
| Rutherglen | 2359 | R | 47.26 | 0.97 | 9.03 | 0.30 | 0.21 | 19.45 | 7.21 | 4.06 | 2.36 | 0.77 | 0.85 | 5.40 | 1.55 | 810 | 2139 | 774 |
| Ardmillan | 2361 | R | 49.07 | 1.14 | 8.87 | 0.33 | 0.19 | 22.04 | 5.39 | 2.80 | 2.50 | 1.12 | 0.75 | 4.48 | 0.97 | 893 | 1065 | 581 |
| Ardnamurchan | 2363 | R | 49.53 | 1.12 | 9.05 | 0.33 | 0.24 | 22.37 | 5.23 | 2.79 | 2.48 | 1.07 | 0.74 | 3.59 | 1.11 | 963 | 1179 | 416 |
| Maud | 2363 | R | 51.21 | 1.15 | 9.54 | 0.33 | 0.19 | 21.96 | 4.50 | 2.38 | 2.63 | 1.12 | 0.70 | 2.97 | 1.01 | 964 | 1123 | 211 |
| Longannet | 2365 | R | 49.07 | 1.14 | 8.95 | 0.28 | 0.25 | 19.56 | 6.67 | 3.17 | 2.30 | 0.84 | 0.78 | 4.71 | 1.66 | 777 | 3799 | 728 |
| Aberlady_DRT | 2367 | R | 48.44 | 1.12 | 9.44 | 0.30 | 0.33 | 19.49 | 7.03 | 3.21 | 2.46 | 0.75 | 0.82 | 4.16 | 1.88 | 640 | 3699 | 486 |
| Aberlady_offset | 2367 | R | 47.42 | 1.16 | 9.07 | 0.34 | 0.32 | 19.79 | 7.26 | 3.65 | 2.18 | 0.73 | 0.81 | 4.99 | 1.63 | 734 | 3678 | 521 |
| Aberlady_triage | 2367 | R | 47.54 | 1.03 | 9.27 | 0.30 | 0.34 | 19.51 | 7.18 | 3.57 | 2.51 | 0.70 | 0.92 | 4.58 | 1.80 | 747 | 3690 | 472 |
| Seil | 2377 | R | 47.25 | 1.07 | 8.70 | 0.36 | 0.44 | 18.95 | 7.53 | 3.88 | 2.30 | 0.66 | 1.03 | 5.38 | 1.70 | 775 | 3745 | 825 |
| Aberlady_drill_tailings_pale | 2380 | F | 42.46 | 1.20 | 8.34 | 0.35 | 0.42 | 21.38 | 6.89 | 6.07 | 2.24 | 0.63 | 0.77 | 8.00 | 0.55 | 756 | 4351 | 529 |
| Aberlady_drill_tailings_red | 2380 | F | 42.28 | 1.18 | 7.79 | 0.36 | 0.38 | 20.74 | 6.74 | 6.56 | 2.24 | 0.60 | 0.75 | 9.17 | 0.55 | 701 | 4229 | 644 |
| Aberlady_dump_corrected | 2380 | F | 41.55 | 1.08 | 8.24 | 0.38 | 0.36 | 20.59 | 5.84 | 7.03 | 2.21 | 0.60 | 0.81 | 9.89 | 0.95 | 818 | 2494 | 211 |
| Kilmarie | 2382 | R | 46.83 | 1.18 | 8.51 | 0.35 | 0.38 | 19.59 | 7.35 | 4.17 | 2.30 | 0.70 | 0.86 | 5.68 | 1.46 | 694 | 3511 | 1086 |
| Kilmarie_offset | 2382 | R | 47.09 | 1.16 | 8.63 | 0.36 | 0.40 | 19.69 | 7.49 | 3.84 | 2.32 | 0.70 | 0.85 | 5.43 | 1.40 | 730 | 3706 | 1060 |
| Kilmarie_dump_centre | 2402 | F | 38.56 | 1.10 | 7.34 | 0.36 | 0.61 | 19.86 | 5.66 | 9.23 | 1.78 | 0.62 | 0.97 | 12.96 | 0.32 | 662 | 4411 | 129 |
| Kilmarie_dump_offset | 2402 | F | 38.41 | 1.15 | 7.19 | 0.38 | 0.58 | 20.09 | 5.62 | 9.41 | 1.78 | 0.60 | 0.94 | 12.92 | 0.32 | 775 | 4164 | 107 |
| Kilmarie_drill_tailings_pale | 2404 | F | 37.04 | 1.12 | 6.26 | 0.28 | 0.43 | 19.41 | 5.60 | 9.98 | 1.35 | 0.59 | 0.64 | 16.19 | 0.46 | 592 | 3894 | 669 |
| Kilmarie_drill_tailings_red | 2404 | F | 39.59 | 1.16 | 6.91 | 0.34 | 0.48 | 20.32 | 5.97 | 8.12 | 1.50 | 0.64 | 0.81 | 12.81 | 0.63 | 714 | 3996 | 806 |
| Haddington | 2408 | R | 47.87 | 1.19 | 8.51 | 0.35 | 0.35 | 21.85 | 5.84 | 3.12 | 2.36 | 1.04 | 0.76 | 4.52 | 1.62 | 859 | 2490 | 1609 |
| Galashiels | 2413 | R | 51.46 | 1.17 | 8.97 | 0.36 | 0.13 | 18.13 | 5.76 | 3.42 | 2.36 | 1.14 | 0.66 | 4.37 | 1.61 | 876 | 1456 | 1124 |
| Grampian_Mountains | 2414 | R | 47.60 | 1.00 | 8.87 | 0.35 | 0.18 | 20.70 | 7.04 | 3.68 | 2.33 | 0.95 | 0.83 | 4.49 | 1.55 | 778 | 1729 | 1053 |
| Broad_Cairn_DRT | 2415 | R | 49.05 | 1.15 | 8.43 | 0.35 | 0.20 | 22.40 | 6.04 | 2.86 | 2.31 | 1.00 | 0.87 | 3.30 | 1.51 | 763 | 2389 | 1256 |
| Broad_Cairn_offset | 2415 | R | 47.34 | 1.13 | 8.49 | 0.35 | 0.24 | 22.15 | 6.56 | 3.30 | 2.37 | 0.91 | 0.99 | 4.27 | 1.30 | 680 | 2404 | 1170 |
| Broad_Cairn_triage | 2415 | R | 47.22 | 1.10 | 8.30 | 0.40 | 0.22 | 22.13 | 6.70 | 3.46 | 2.37 | 0.94 | 0.83 | 4.35 | 1.45 | 811 | 2160 | 1185 |
| Hillhead | 2419 | R | 49.50 | 1.13 | 9.65 | 0.28 | 0.18 | 22.38 | 5.05 | 2.67 | 2.49 | 1.03 | 0.57 | 3.77 | 0.87 | 963 | 992 | 76 |
| Kinghorn | 2419 | R | 49.66 | 1.15 | 8.99 | 0.33 | 0.29 | 22.76 | 4.82 | 2.59 | 2.46 | 1.10 | 0.83 | 3.67 | 1.04 | 995 | 1055 | 230 |
| Kintore | 2419 | R | 49.34 | 1.10 | 9.64 | 0.35 | 0.17 | 21.37 | 5.52 | 2.99 | 2.65 | 1.06 | 0.69 | 3.92 | 0.90 | 722 | 908 | 96 |
| Crakaig | 2422 | R | 49.98 | 1.09 | 8.66 | 0.32 | 0.07 | 21.59 | 5.91 | 2.81 | 2.24 | 1.07 | 0.66 | 4.08 | 1.13 | 896 | 1363 | 721 |
| Morningside_raster1 | 2424 | RT | 38.86 | 0.90 | 7.60 | 0.27 | 0.20 | 16.92 | 6.82 | 9.64 | 2.34 | 0.60 | 0.76 | 13.84 | 1.02 | 606 | 837 | 309 |
| Morningside_raster2 | 2424 | RT | 45.02 | 1.06 | 8.66 | 0.38 | 0.26 | 21.72 | 7.23 | 4.85 | 2.56 | 0.80 | 0.85 | 5.32 | 1.00 | 888 | 905 | 566 |
| Morningside_raster3 | 2424 | RT | 45.39 | 1.07 | 8.60 | 0.42 | 0.37 | 20.36 | 7.90 | 5.12 | 2.42 | 0.65 | 0.92 | 5.24 | 1.17 | 818 | 1621 | 469 |
| Mons_Graupius | 2427 | R | 46.05 | 1.17 | 8.72 | 0.36 | 0.47 | 20.29 | 7.31 | 4.43 | 2.37 | 0.71 | 0.92 | 5.40 | 1.35 | 785 | 2464 | 541 |
| Tobermory | 2427 | R | 46.99 | 1.06 | 8.70 | 0.37 | 0.23 | 20.50 | 7.26 | 4.43 | 2.46 | 0.77 | 0.74 | 4.75 | 1.38 | 811 | 1666 | 489 |
| Gullane | 2431 | R | 53.10 | 1.17 | 10.17 | 0.34 | 0.34 | 17.79 | 5.22 | 2.74 | 2.58 | 1.34 | 0.75 | 3.27 | 0.87 | 771 | 1338 | 321 |
| Hill_of_Skares | 2431 | R | 46.88 | 1.10 | 8.62 | 0.31 | 0.21 | 26.24 | 4.92 | 2.46 | 2.53 | 1.06 | 1.08 | 3.20 | 1.05 | 849 | 1384 | 382 |
| Smoogro | 2434 | R | 51.38 | 1.09 | 9.67 | 0.32 | 0.15 | 21.42 | 4.56 | 2.52 | 2.72 | 1.25 | 0.65 | 2.86 | 1.07 | 985 | 1311 | 448 |
| Almond_raster1 | 2437 | RT | 46.20 | 1.11 | 9.09 | 0.46 | 0.23 | 21.66 | 7.36 | 4.86 | 2.57 | 0.84 | 0.86 | 3.75 | 0.75 | 628 | 639 | 88 |
| Almond_raster2 | 2437 | RT | 42.80 | 1.15 | 9.14 | 0.69 | 0.40 | 21.80 | 8.97 | 6.56 | 2.57 | 0.54 | 0.80 | 3.83 | 0.61 | 542 | 432 | 45 |
| Iapetus | 2437 | R | 48.53 | 1.13 | 9.07 | 0.36 | 0.14 | 22.52 | 5.51 | 3.04 | 2.59 | 1.01 | 0.73 | 4.15 | 0.91 | 854 | 1172 | 462 |
| Urr | 2441 | R | 48.83 | 1.14 | 9.39 | 0.34 | 0.10 | 22.66 | 5.01 | 2.80 | 2.61 | 1.36 | 0.67 | 3.68 | 1.12 | 883 | 1217 | 38 |
| Tolsta | 2449 | R | 50.77 | 1.14 | 9.25 | 0.30 | 0.08 | 22.48 | 4.49 | 2.51 | 2.41 | 1.24 | 0.69 | 3.22 | 1.05 | 692 | 1063 | 719 |

| Target | Sol | Type[2] | $SiO_2$ | $TiO_2$ | $Al_2O_3$ | $Cr_2O_3$ | MnO | FeO | MgO | CaO | $Na_2O$ | $K_2O$ | $P_2O_5$ | $SO_3$ | Cl | Ni | Zn | Br |
|---|---|---|---|---|---|---|---|---|---|---|---|---|---|---|---|---|---|---|
| **Carolyn Shoemaker formation: Knockfarril Hill member (KHm)** | | | | | | | | | | | | | | | | | | |
| Calgary_Bay | 2442 | R | 42.99 | 1.13 | 8.50 | 0.31 | 0.38 | 20.11 | 7.82 | 5.83 | 2.32 | 0.54 | 1.01 | 7.38 | 1.16 | 707 | 3362 | 426 |
| Balnakettle | 2443 | R | 42.92 | 1.15 | 8.86 | 0.34 | 0.27 | 20.45 | 8.06 | 5.37 | 2.39 | 0.65 | 0.97 | 6.70 | 1.27 | 725 | 2922 | 450 |
| Beauly_DRT | 2443 | R | 42.73 | 1.05 | 8.30 | 0.28 | 0.28 | 18.55 | 7.14 | 6.51 | 2.26 | 0.58 | 0.97 | 9.77 | 1.09 | 684 | 3122 | 406 |
| Stack_of_Glencoul | 2446 | R | 43.65 | 1.10 | 8.57 | 0.32 | 0.27 | 19.17 | 6.98 | 5.96 | 2.34 | 0.71 | 0.75 | 8.19 | 1.41 | 712 | 3720 | 492 |
| Badcall | 2450 | R | 43.31 | 1.08 | 8.50 | 0.31 | 1.25 | 20.69 | 6.20 | 5.64 | 2.13 | 0.68 | 1.19 | 7.25 | 0.96 | 697 | 4465 | 159 |
| Buckie_DRT | 2450 | R | 38.44 | 1.11 | 7.97 | 0.34 | 0.70 | 19.96 | 6.22 | 7.81 | 2.30 | 0.64 | 1.31 | 11.27 | 1.43 | 655 | 2861 | 602 |
| Magnus_Bay | 2452 | R | 47.38 | 1.18 | 9.14 | 0.36 | 0.29 | 19.87 | 6.12 | 4.57 | 2.32 | 0.86 | 1.00 | 5.25 | 1.18 | 861 | 2743 | 272 |
| Perth | 2454 | R | 48.63 | 1.03 | 8.50 | 0.35 | 0.12 | 20.63 | 6.67 | 3.24 | 2.23 | 1.07 | 0.69 | 4.77 | 1.49 | 997 | 2778 | 1184 |
| Newtonhill | 2458 | R | 45.54 | 1.04 | 8.76 | 0.33 | 0.20 | 19.50 | 7.55 | 4.62 | 2.48 | 0.81 | 0.74 | 6.28 | 1.50 | 922 | 2506 | 544 |
| Oykel_DRT | 2458 | R | 46.53 | 1.18 | 8.41 | 0.35 | 0.22 | 19.97 | 6.62 | 4.57 | 2.26 | 0.94 | 0.81 | 6.26 | 1.34 | 837 | 2690 | 1056 |
| Sligachan | 2461 | R | 46.57 | 1.13 | 9.09 | 0.37 | 0.25 | 19.72 | 7.77 | 4.20 | 2.46 | 0.76 | 0.95 | 4.83 | 1.38 | 761 | 2861 | 779 |
| Feshie | 2462 | R | 45.43 | 1.02 | 8.80 | 0.31 | 0.30 | 19.87 | 6.97 | 4.70 | 2.35 | 0.78 | 0.97 | 6.55 | 1.43 | 815 | 2723 | 418 |
| Tay | 2463 | R | 47.38 | 1.06 | 9.29 | 0.37 | 0.16 | 19.59 | 7.22 | 4.07 | 2.43 | 0.85 | 0.70 | 4.63 | 1.68 | 891 | 3097 | 591 |
| Ecclefechan | 2465 | R | 46.39 | 1.12 | 8.78 | 0.34 | 0.22 | 19.61 | 7.56 | 4.36 | 2.48 | 0.82 | 0.84 | 5.44 | 1.60 | 848 | 2034 | 793 |
| Kirbuster | 2465 | R | 46.54 | 1.14 | 9.09 | 0.35 | 0.42 | 20.49 | 6.83 | 3.38 | 2.59 | 1.12 | 1.35 | 4.30 | 1.92 | 964 | 1953 | 754 |
| Paible | 2468 | R | 48.61 | 1.08 | 9.50 | 0.33 | 0.06 | 22.61 | 5.27 | 2.93 | 2.53 | 1.23 | 0.74 | 3.78 | 1.02 | 773 | 1196 | 141 |
| Nith | 2470 | R | 48.41 | 1.16 | 9.25 | 0.35 | 0.13 | 18.84 | 5.69 | 4.41 | 2.30 | 1.11 | 0.74 | 5.64 | 1.64 | 924 | 1297 | 322 |
| Solway_Firth_DRT | 2471 | R | 47.39 | 1.17 | 8.64 | 0.36 | 0.17 | 18.80 | 6.16 | 4.61 | 2.35 | 1.04 | 1.05 | 6.56 | 1.31 | 907 | 1348 | 831 |
| East_Shetland_DRT | 2472 | R | 48.72 | 1.18 | 9.14 | 0.37 | 0.15 | 18.75 | 5.86 | 3.92 | 2.51 | 1.10 | 0.93 | 5.13 | 1.82 | 939 | 1223 | 967 |
| Essendy | 2472 | R | 47.03 | 1.17 | 8.24 | 0.34 | 0.15 | 21.79 | 6.19 | 3.70 | 2.22 | 1.15 | 0.82 | 5.02 | 1.71 | 1023 | 1391 | 1064 |
| Mither_Tap | 2474 | R | 46.93 | 1.14 | 8.82 | 0.33 | 0.09 | 22.48 | 5.81 | 3.34 | 2.54 | 1.17 | 0.81 | 4.59 | 1.53 | 882 | 1086 | 1024 |
| Moine | 2474 | R | 44.14 | 1.08 | 8.55 | 0.33 | 0.11 | 19.91 | 5.13 | 5.83 | 2.53 | 1.09 | 0.88 | 8.67 | 1.47 | 851 | 886 | 144 |
| Cruden_Bay | 2477 | R | 44.61 | 0.96 | 8.60 | 0.42 | 0.33 | 20.42 | 7.76 | 5.15 | 2.49 | 0.75 | 0.90 | 5.82 | 1.22 | 1026 | 1650 | 343 |
| Fetterangus | 2478 | R | 45.36 | 1.12 | 8.56 | 0.34 | 0.17 | 21.91 | 6.85 | 3.99 | 2.44 | 1.06 | 0.81 | 5.55 | 1.43 | 974 | 1382 | 679 |
| Fetterangus_offset | 2478 | R | 45.14 | 1.14 | 8.49 | 0.33 | 0.17 | 21.88 | 7.00 | 4.21 | 2.35 | 1.01 | 0.72 | 5.80 | 1.37 | 949 | 1364 | 633 |
| Glen_Etive_1_DRT | 2482 | R | 49.19 | 1.16 | 9.07 | 0.35 | 0.17 | 20.37 | 5.69 | 3.49 | 2.31 | 1.29 | 0.79 | 4.25 | 1.45 | 961 | 1819 | 685 |
| Glen_Etive_1_offset | 2482 | R | 47.88 | 1.15 | 8.75 | 0.36 | 0.19 | 19.71 | 6.12 | 4.12 | 2.35 | 1.19 | 0.78 | 5.47 | 1.47 | 955 | 1837 | 832 |
| Glen_Etive_2_DRT | 2483 | R | 45.51 | 1.10 | 8.30 | 0.34 | 0.18 | 19.93 | 6.32 | 5.09 | 2.28 | 1.07 | 0.81 | 7.30 | 1.29 | 963 | 1759 | 922 |
| Glen_Etive_1_dump_centre | 2523 | F | 43.87 | 1.21 | 8.41 | 0.39 | 0.27 | 23.46 | 5.74 | 5.03 | 2.18 | 1.07 | 0.81 | 6.37 | 0.78 | 1042 | 1834 | 281 |
| Glen_Etive_1_tailings | 2524 | F | 47.38 | 1.30 | 8.59 | 0.40 | 0.22 | 23.57 | 5.41 | 3.85 | 2.14 | 1.28 | 0.77 | 4.13 | 0.49 | 1168 | 2327 | 153 |
| Glen_Etive_2_dump_corrected | 2552 | F | 38.64 | 1.14 | 7.30 | 0.36 | 0.25 | 20.16 | 4.63 | 9.66 | 1.81 | 1.04 | 0.69 | 13.17 | 0.71 | 1006 | 2372 | 82 |
| Glen_Etive_2_tailings | 2553 | F | 41.68 | 1.22 | 7.68 | 0.39 | 0.29 | 22.23 | 5.44 | 6.71 | 2.04 | 1.11 | 0.84 | 9.32 | 0.55 | 1056 | 2651 | 240 |
| High_Plains | 2557 | RT | 47.27 | 1.10 | 9.09 | 0.33 | 0.12 | 22.68 | 5.97 | 3.47 | 2.56 | 1.05 | 0.75 | 4.47 | 0.91 | 840 | 626 | 88 |
| Skipness | 2558 | RT | 43.26 | 1.02 | 9.34 | 0.47 | 0.31 | 20.56 | 8.39 | 6.34 | 2.70 | 0.58 | 0.85 | 5.19 | 0.80 | 645 | 392 | 121 |
| Orkney | 2563 | RT | 44.53 | 1.03 | 9.07 | 0.42 | 0.25 | 21.84 | 7.42 | 4.93 | 2.73 | 0.67 | 0.82 | 5.05 | 0.98 | 727 | 587 | 119 |
| Shetland | 2564 | R | 49.01 | 1.14 | 9.23 | 0.32 | 0.10 | 22.67 | 4.78 | 2.93 | 2.64 | 1.17 | 0.76 | 3.65 | 1.34 | 770 | 709 | 254 |
| South_Ronaldsay_DRT | 2567 | R | 47.71 | 1.08 | 8.71 | 0.31 | 0.11 | 20.09 | 5.11 | 4.30 | 2.43 | 1.03 | 1.13 | 6.30 | 1.39 | 949 | 622 | 617 |
| White_Craig | 2567 | R | 43.97 | 1.15 | 8.67 | 0.31 | 0.10 | 19.45 | 6.42 | 5.53 | 2.40 | 0.93 | 0.88 | 8.56 | 1.38 | 882 | 651 | 202 |
| Ben_Hope | 2570 | R | 48.00 | 1.06 | 8.86 | 0.34 | 0.13 | 20.64 | 5.99 | 3.59 | 2.50 | 1.06 | 0.93 | 4.98 | 1.60 | 826 | 887 | 597 |
| Glen_Mark | 2572 | R | 44.34 | 1.03 | 8.33 | 0.29 | 0.14 | 18.20 | 7.11 | 6.00 | 2.46 | 0.79 | 0.97 | 8.66 | 1.21 | 820 | 874 | 428 |
| Stonehive | 2574 | R | 41.51 | 0.98 | 8.09 | 0.28 | 0.16 | 17.22 | 5.91 | 8.14 | 2.47 | 0.75 | 0.90 | 12.15 | 1.24 | 560 | 632 | 183 |
| Upperhill_DRT | 2574 | R | 47.96 | 1.05 | 8.36 | 0.30 | 0.19 | 20.91 | 4.78 | 4.21 | 2.31 | 1.05 | 0.85 | 6.17 | 1.47 | 960 | 1037 | 1125 |
| Pobie_Bank | 2577 | R | 50.55 | 1.19 | 9.29 | 0.38 | 0.14 | 18.83 | 5.71 | 3.67 | 2.51 | 1.06 | 0.81 | 4.50 | 1.09 | 898 | 694 | 92 |
| Gleneagles | 2579 | R | 45.65 | 1.05 | 8.17 | 0.32 | 0.17 | 20.15 | 6.40 | 4.79 | 2.40 | 0.95 | 0.80 | 7.61 | 1.10 | 1115 | 1340 | 573 |
| Conachair_DRT | 2581 | R | 47.26 | 1.15 | 8.77 | 0.38 | 0.20 | 18.27 | 7.09 | 4.76 | 2.32 | 0.78 | 0.89 | 6.54 | 1.16 | 892 | 1452 | 209 |
| Conachair_offset | 2581 | R | 44.08 | 1.12 | 8.78 | 0.31 | 0.22 | 15.52 | 7.68 | 6.95 | 2.55 | 0.66 | 1.04 | 9.72 | 1.09 | 729 | 1210 | 84 |
| Blawhorn | 2587 | R | 45.24 | 1.02 | 8.60 | 0.29 | 0.14 | 19.89 | 6.15 | 5.12 | 2.52 | 0.83 | 1.07 | 7.53 | 1.23 | 841 | 566 | 534 |
| Gorgie | 2587 | R | 45.81 | 1.05 | 8.61 | 0.30 | 0.13 | 19.72 | 5.13 | 5.06 | 2.44 | 0.92 | 1.11 | 8.32 | 1.15 | 917 | 595 | 75 |
| Nedd | 2590 | R | 49.57 | 1.00 | 9.20 | 0.31 | 0.08 | 19.85 | 5.24 | 3.52 | 2.56 | 1.02 | 0.88 | 5.15 | 1.19 | 900 | 505 | 256 |
| Ard_Neakie | 2591 | R | 49.73 | 1.14 | 9.34 | 0.33 | 0.09 | 20.71 | 5.16 | 3.33 | 2.58 | 1.15 | 0.78 | 4.30 | 1.09 | 727 | 675 | 348 |
| Glen_Doll | 2591 | R | 45.52 | 1.14 | 8.63 | 0.32 | 0.12 | 19.81 | 5.48 | 5.17 | 2.48 | 0.98 | 1.11 | 7.85 | 1.16 | 723 | 609 | 157 |
| Muckle_Flugga_DRT | 2591 | R | 47.37 | 1.11 | 8.53 | 0.32 | 0.12 | 20.42 | 5.60 | 4.44 | 2.52 | 0.99 | 0.97 | 6.08 | 1.17 | 757 | 644 | 1184 |
| Everbay_DRT | 2598 | R | 53.17 | 1.16 | 9.64 | 0.34 | 0.09 | 18.21 | 4.34 | 2.76 | 2.46 | 1.12 | 1.25 | 3.58 | 1.56 | 915 | 877 | 604 |
| Inverurie_DRT | 2601 | R | 45.90 | 1.04 | 8.50 | 0.30 | 0.11 | 17.58 | 4.95 | 5.95 | 2.32 | 0.94 | 1.06 | 9.90 | 1.18 | 855 | 848 | 218 |
| Latherton | 2601 | R | 47.98 | 1.07 | 9.15 | 0.32 | 0.12 | 19.65 | 5.98 | 3.80 | 2.65 | 1.01 | 0.96 | 5.49 | 1.52 | 918 | 885 | 285 |
| Kintyre_Way_offset | 2819 | R | 48.45 | 1.10 | 9.07 | 0.29 | 0.14 | 21.90 | 5.50 | 2.65 | 2.64 | 1.09 | 0.88 | 4.80 | 1.19 | 905 | 917 | 451 |
| Kintyre_Way | 2820 | R | 48.73 | 1.11 | 9.13 | 0.31 | 0.12 | 21.99 | 5.35 | 2.51 | 2.66 | 1.09 | 0.88 | 4.73 | 1.09 | 899 | 961 | 349 |
| Breamish_DRT | 2826 | R | 46.98 | 1.11 | 9.11 | 0.33 | 0.85 | 18.48 | 7.30 | 3.43 | 2.38 | 0.89 | 1.11 | 5.70 | 1.77 | 878 | 3204 | 311 |
| Breamish_offset | 2826 | R | 48.45 | 1.15 | 9.16 | 0.35 | 0.79 | 17.80 | 7.04 | 3.28 | 2.30 | 0.98 | 0.95 | 5.28 | 1.96 | 916 | 3177 | 292 |
| Mary_Anning_DRT | 2833 | R | 48.07 | 1.17 | 8.91 | 0.36 | 0.51 | 18.96 | 7.21 | 3.06 | 2.38 | 0.94 | 0.83 | 5.39 | 1.75 | 760 | 2415 | 558 |
| Mary_Anning_offset | 2833 | R | 47.14 | 1.14 | 9.01 | 0.33 | 0.50 | 18.81 | 7.49 | 3.26 | 2.41 | 0.88 | 0.87 | 6.06 | 1.66 | 774 | 2444 | 567 |
| Mary_Anning_dump_1 | 2851 | F | 43.71 | 1.10 | 8.01 | 0.37 | 0.39 | 20.44 | 6.50 | 5.83 | 2.15 | 0.86 | 0.70 | 8.59 | 0.93 | 906 | 2192 | 239 |
| Mary_Anning_dump_2 | 2851 | F | 42.85 | 1.11 | 8.05 | 0.32 | 0.37 | 19.77 | 6.55 | 6.32 | 2.16 | 0.88 | 0.73 | 9.60 | 0.91 | 867 | 2124 | 56 |
| Mary_Anning_tailings | 2853 | F | 45.14 | 1.15 | 8.09 | 0.37 | 0.57 | 19.64 | 7.79 | 4.32 | 2.12 | 0.85 | 0.85 | 7.90 | 0.77 | 784 | 2430 | 478 |
| Ayton_raster1 | 2857 | R | 44.46 | 1.05 | 8.78 | 0.33 | 1.40 | 16.97 | 7.90 | 4.05 | 2.40 | 0.74 | 2.67 | 7.20 | 1.66 | 457 | 2296 | 369 |
| Ayton_raster2 | 2857 | R | 38.79 | 1.01 | 8.19 | 0.30 | 1.91 | 16.26 | 7.86 | 6.25 | 2.52 | 0.57 | 3.56 | 10.93 | 1.53 | 367 | 1967 | 263 |
| Ayton_raster3 | 2857 | R | 36.19 | 0.88 | 7.84 | 0.25 | 2.44 | 16.27 | 7.59 | 6.54 | 2.62 | 0.55 | 5.49 | 11.52 | 1.49 | 309 | 1505 | 232 |
| Mary_Anning_2_DRT | 2858 | R | 48.18 | 1.11 | 9.01 | 0.32 | 0.48 | 18.98 | 7.05 | 3.12 | 2.44 | 0.99 | 0.77 | 5.40 | 1.75 | 776 | 2089 | 475 |
| Mary_Anning_2_offset | 2858 | R | 48.28 | 1.11 | 8.89 | 0.34 | 0.49 | 19.08 | 6.96 | 3.19 | 2.40 | 1.03 | 0.80 | 5.31 | 1.71 | 793 | 2065 | 473 |
| Falkirk_Wheel | 2862 | R | 43.49 | 1.08 | 8.58 | 0.36 | 1.03 | 18.32 | 8.68 | 4.34 | 2.13 | 0.73 | 2.01 | 7.41 | 1.47 | 656 | 1950 | 450 |
| Falkirk_Wheel_offset | 2862 | R | 46.39 | 1.13 | 8.84 | 0.34 | 0.74 | 17.71 | 8.43 | 3.55 | 2.45 | 0.88 | 1.56 | 6.20 | 1.39 | 724 | 2104 | 430 |
| Mary_Anning_3_DRT | 2867 | R | 46.01 | 1.09 | 8.68 | 0.35 | 0.53 | 18.83 | 7.42 | 4.14 | 2.38 | 0.82 | 0.91 | 6.79 | 1.53 | 737 | 2321 | 472 |
| Mary_Anning_3_offset | 2867 | R | 46.18 | 1.14 | 8.85 | 0.34 | 0.50 | 18.33 | 7.32 | 4.04 | 2.39 | 0.84 | 0.90 | 7.08 | 1.63 | 799 | 2202 | 401 |
| Mary_Anning_3_dump_2 | 2890 | F | 38.96 | 1.06 | 7.83 | 0.36 | 0.66 | 18.22 | 7.59 | 7.77 | 2.21 | 0.69 | 1.37 | 12.06 | 0.89 | 674 | 1826 | 58 |
| Groken_DRT | 2906 | R | 43.56 | 1.03 | 8.49 | 0.30 | 1.40 | 16.43 | 8.00 | 4.09 | 2.43 | 0.77 | 2.64 | 8.76 | 1.73 | 500 | 2175 | 329 |
| Groken_offset | 2906 | R | 41.73 | 1.03 | 8.45 | 0.29 | 1.20 | 15.18 | 8.72 | 4.64 | 2.48 | 0.67 | 2.22 | 11.50 | 1.57 | 388 | 1924 | 249 |
| Trow_DRT | 2908 | R | 42.93 | 1.06 | 8.64 | 0.29 | 1.15 | 16.19 | 7.71 | 5.09 | 2.45 | 0.71 | 2.38 | 9.33 | 1.72 | 497 | 2072 | 357 |
| Trow_offset | 2908 | R | 42.87 | 1.12 | 8.50 | 0.33 | 1.24 | 16.14 | 8.24 | 4.54 | 2.38 | 0.69 | 2.49 | 9.45 | 1.61 | 502 | 2171 | 333 |
| Groken_tailings | 2921 | F | 37.32 | 1.10 | 7.59 | 0.42 | 1.07 | 19.66 | 9.35 | 6.15 | 2.33 | 0.60 | 2.13 | 11.33 | 0.50 | 630 | 2118 | 254 |

| Target | Sol | Type[2] | $SiO_2$ | $TiO_2$ | $Al_2O_3$ | $Cr_2O_3$ | MnO | FeO | MgO | CaO | $Na_2O$ | $K_2O$ | $P_2O_5$ | $SO_3$ | Cl | Ni | Zn | Br |
|---|---|---|---|---|---|---|---|---|---|---|---|---|---|---|---|---|---|---|
| **Carolyn Shoemaker formation: Glasgow member (Gm)** | | | | | | | | | | | | | | | | | | |
| Sourhope | 2583 | R | 46.37 | 1.11 | 8.84 | 0.33 | 0.21 | 18.26 | 6.30 | 4.95 | 2.40 | 0.85 | 0.93 | 7.98 | 1.20 | 857 | 1191 | 78 |
| Foggy_Moss | 2585 | Ft | 48.06 | 1.09 | 9.41 | 0.34 | 0.12 | 18.72 | 5.40 | 4.44 | 2.25 | 0.92 | 0.94 | 6.69 | 1.31 | 935 | 1175 | 128 |
| Kirkcudbrightshire | 2585 | R | 45.29 | 1.14 | 8.53 | 0.36 | 0.22 | 18.42 | 7.65 | 5.22 | 2.52 | 0.72 | 0.93 | 7.32 | 1.32 | 840 | 1187 | 747 |
| Well_Run | 2604 | R | 47.98 | 1.03 | 9.10 | 0.26 | 0.18 | 19.38 | 5.73 | 4.19 | 2.38 | 0.94 | 1.03 | 6.37 | 1.11 | 890 | 1147 | 165 |
| Staxigoe | 2606 | R | 48.25 | 1.19 | 8.99 | 0.38 | 0.15 | 17.87 | 6.45 | 4.19 | 2.64 | 0.87 | 0.81 | 6.37 | 1.46 | 895 | 1274 | 435 |
| Gretna_Green | 2608 | Ft | 36.84 | 0.44 | 5.08 | 0.68 | 0.35 | 22.42 | 15.63 | 4.74 | 1.68 | 0.37 | 0.83 | 9.40 | 1.22 | 2623 | 126 | 66 |
| Scotnish_DRT | 2608 | R | 46.69 | 1.06 | 8.47 | 0.30 | 0.11 | 17.64 | 4.23 | 5.55 | 2.16 | 1.02 | 0.76 | 10.78 | 0.94 | 732 | 894 | 213 |
| Renfrewshire | 2611 | R | 47.28 | 1.05 | 8.89 | 0.33 | 0.11 | 17.53 | 5.09 | 5.08 | 2.31 | 0.95 | 0.81 | 8.94 | 1.27 | 783 | 1287 | 19 |
| Glenmard_Wood | 2613 | R | 44.21 | 1.07 | 8.93 | 0.33 | 0.19 | 20.12 | 6.76 | 5.13 | 2.51 | 0.62 | 0.81 | 7.88 | 1.14 | 1073 | 1074 | 122 |
| North_Esk | 2616 | R | 45.74 | 0.99 | 8.64 | 0.28 | 0.12 | 17.75 | 6.17 | 5.85 | 2.51 | 0.66 | 0.80 | 8.99 | 1.05 | 848 | 781 | 189 |
| Ben_Arnaboll_DRT | 2631 | R | 45.48 | 0.86 | 8.67 | 0.27 | 0.25 | 16.69 | 5.95 | 6.37 | 2.42 | 0.73 | 0.86 | 10.22 | 0.72 | 772 | 1332 | 178 |
| Blackwaterfoot | 2631 | Ft | 44.42 | 0.77 | 9.16 | 0.63 | 0.48 | 19.13 | 8.74 | 7.25 | 3.22 | 1.21 | 0.90 | 3.23 | 0.74 | 293 | 373 | 57 |
| Buchan_Haven_DRT | 2640 | R | 51.62 | 0.94 | 9.83 | 0.28 | 0.32 | 16.76 | 6.30 | 5.80 | 3.05 | 0.91 | 1.15 | 2.26 | 0.50 | 587 | 1547 | 89 |
| Heinrich_Waenke | 2641 | Ft | 45.49 | 1.01 | 9.09 | 0.32 | 0.43 | 18.72 | 7.44 | 7.05 | 3.36 | 2.28 | 1.13 | 2.66 | 0.66 | 889 | 1876 | 38 |
| Abernethy | 2642 | V | 24.55 | 0.43 | 5.20 | 0.08 | 5.11 | 40.12 | 7.53 | 3.59 | 1.66 | 0.21 | 0.69 | 8.55 | 1.81 | 560 | 2630 | 519 |
| Lomond_Hills | 2642 | Ft | 46.64 | 0.92 | 10.20 | 0.28 | 0.35 | 17.06 | 7.89 | 6.00 | 4.17 | 2.37 | 1.31 | 1.90 | 0.58 | 716 | 1367 | 74 |
| Kennedys Pass | 2645 | R | 48.86 | 1.01 | 9.05 | 0.25 | 0.13 | 18.61 | 5.87 | 4.12 | 2.38 | 0.78 | 0.98 | 6.39 | 1.30 | 838 | 810 | 356 |
| Arbroath | 2647 | R | 49.86 | 1.00 | 9.42 | 0.34 | 0.10 | 16.93 | 5.75 | 3.94 | 2.61 | 0.84 | 0.88 | 6.63 | 1.25 | 910 | 984 | 54 |
| Moffat_Hills | 2653 | R | 47.36 | 0.98 | 9.19 | 0.30 | 0.18 | 19.03 | 5.63 | 3.37 | 2.18 | 0.82 | 1.26 | 8.34 | 0.95 | 878 | 960 | 65 |
| Trossachs_DRT | 2653 | R | 50.02 | 1.08 | 8.86 | 0.31 | 0.14 | 18.27 | 4.98 | 3.93 | 2.68 | 0.88 | 0.92 | 5.86 | 1.71 | 898 | 946 | 1040 |
| Rannoch_Moor | 2656 | R | 46.90 | 1.03 | 9.02 | 0.31 | 0.15 | 18.79 | 6.91 | 4.15 | 2.62 | 0.79 | 0.95 | 6.62 | 1.22 | 926 | 890 | 540 |
| Sauchiehall_DRT | 2656 | R | 49.18 | 1.06 | 8.88 | 0.29 | 0.11 | 16.84 | 4.02 | 5.59 | 2.19 | 0.94 | 0.91 | 8.95 | 0.77 | 845 | 907 | 75 |
| Marchmont | 2658 | R | 43.75 | 0.94 | 8.32 | 0.30 | 0.20 | 18.52 | 6.16 | 6.55 | 2.28 | 0.68 | 0.86 | 10.11 | 0.86 | 981 | 659 | 42 |
| Beefstand_Hill_DRT | 2744 | R | 50.95 | 1.04 | 9.51 | 0.29 | 0.15 | 19.14 | 4.31 | 3.71 | 2.37 | 0.88 | 0.99 | 5.82 | 0.58 | 828 | 935 | 74 |
| Beefstand_Hill_offset | 2744 | R | 49.41 | 1.03 | 9.11 | 0.29 | 0.15 | 19.20 | 4.86 | 3.85 | 2.26 | 0.84 | 0.94 | 7.16 | 0.65 | 830 | 956 | 82 |
| Glasgow_1_DRT | 2749 | R | 53.11 | 1.12 | 9.50 | 0.32 | 0.11 | 17.28 | 4.65 | 3.47 | 2.32 | 0.96 | 1.19 | 4.46 | 1.15 | 1080 | 1103 | 607 |
| Glasgow_1_offset | 2749 | R | 48.32 | 1.00 | 8.73 | 0.29 | 0.11 | 15.98 | 4.76 | 5.79 | 2.33 | 0.86 | 1.03 | 9.16 | 1.27 | 913 | 972 | 494 |
| Glasgow1_dump_corrected | 2775 | F | 46.87 | 1.08 | 8.74 | 0.38 | 0.17 | 18.82 | 4.74 | 6.11 | 2.23 | 0.91 | 1.03 | 7.48 | 1.12 | 964 | 1039 | 200 |
| Glasgow1_tailings | 2776 | F | 47.51 | 1.10 | 8.69 | 0.41 | 0.22 | 19.02 | 4.71 | 6.22 | 2.11 | 0.78 | 1.05 | 6.99 | 0.91 | 916 | 876 | 29 |
| Heather_Island_DRT | 2785 | R | 42.12 | 0.98 | 7.48 | 0.28 | 0.13 | 16.75 | 4.35 | 7.69 | 2.40 | 0.82 | 0.90 | 14.16 | 1.65 | 794 | 720 | 568 |
| Hedgeley_Moor_DRT | 2792 | R | 50.37 | 1.10 | 8.97 | 0.30 | 0.13 | 21.17 | 4.83 | 3.07 | 2.40 | 1.08 | 1.08 | 3.94 | 1.18 | 992 | 951 | 936 |
| Hedgeley_Moor_offset | 2792 | R | 48.00 | 1.08 | 8.66 | 0.32 | 0.16 | 21.39 | 5.50 | 3.72 | 2.45 | 0.99 | 0.93 | 5.21 | 1.24 | 1015 | 921 | 799 |
| Chambers_Street_DRT | 2801 | R | 51.04 | 1.15 | 9.08 | 0.32 | 0.17 | 14.34 | 4.49 | 5.19 | 2.25 | 0.79 | 0.76 | 8.89 | 1.13 | 1018 | 1159 | 1029 |
| Chambers_Street_offset | 2801 | R | 48.96 | 1.11 | 9.12 | 0.34 | 0.16 | 14.65 | 5.56 | 5.82 | 2.32 | 0.71 | 0.81 | 8.98 | 1.15 | 954 | 1155 | 310 |
| Capercaillie | 2803 | R | 45.08 | 1.03 | 8.55 | 0.30 | 0.13 | 16.14 | 5.39 | 6.73 | 2.38 | 0.85 | 0.81 | 11.30 | 1.01 | 821 | 983 | 95 |
| Capercaillie_offset | 2803 | R | 43.21 | 1.04 | 8.58 | 0.32 | 0.13 | 15.60 | 5.65 | 7.66 | 2.48 | 0.76 | 0.90 | 12.40 | 1.01 | 791 | 952 | 95 |
| Edinburrie | 2959 | R | 47.68 | 1.02 | 8.72 | 0.33 | 0.34 | 19.46 | 5.90 | 4.09 | 2.22 | 0.99 | 0.92 | 6.09 | 1.55 | 1318 | 3143 | 687 |
| Achnasheen | 2965 | R | 49.59 | 1.11 | 9.18 | 0.29 | 0.18 | 20.62 | 5.15 | 3.04 | 2.37 | 1.08 | 0.95 | 4.71 | 1.33 | 918 | 1713 | 438 |
| Dun_Eideann | 2967 | R | 47.61 | 1.10 | 8.85 | 0.30 | 0.32 | 19.95 | 5.85 | 3.60 | 2.35 | 1.08 | 1.02 | 5.90 | 1.52 | 991 | 2090 | 443 |
| Auchnafree_Hill | 2969 | R | 51.66 | 1.11 | 9.47 | 0.32 | 0.23 | 19.17 | 5.32 | 2.78 | 2.57 | 1.12 | 0.87 | 3.73 | 1.22 | 1073 | 1735 | 517 |
| Coupar_Angus | 2969 | R | 49.72 | 1.04 | 8.92 | 0.30 | 0.20 | 18.80 | 5.80 | 2.92 | 2.50 | 1.13 | 0.80 | 6.12 | 1.31 | 911 | 1329 | 689 |
| Torness | 2972 | R | 51.85 | 1.13 | 9.14 | 0.28 | 0.16 | 19.71 | 4.74 | 2.67 | 2.23 | 1.19 | 0.95 | 4.47 | 1.17 | 893 | 1252 | 71 |
| Carn_Mor | 2974 | R | 46.67 | 1.04 | 8.50 | 0.31 | 0.19 | 19.83 | 6.65 | 3.01 | 2.59 | 0.99 | 1.02 | 7.11 | 1.70 | 946 | 1204 | 725 |
| Cod_Baa_DRT | 2975 | R | 46.76 | 1.07 | 8.62 | 0.31 | 0.29 | 19.69 | 6.13 | 4.05 | 2.37 | 0.92 | 1.11 | 6.57 | 1.60 | 1177 | 2067 | 699 |
| An_Dun_raster1 | 2976 | N | 45.01 | 1.01 | 8.36 | 0.25 | 0.18 | 18.14 | 7.58 | 3.55 | 2.57 | 0.92 | 1.06 | 9.56 | 1.46 | 832 | 1266 | 560 |
| An_Dun_raster2 | 2976 | N | 43.59 | 1.02 | 8.33 | 0.31 | 0.19 | 18.02 | 8.26 | 3.47 | 2.18 | 0.87 | 1.00 | 11.02 | 1.38 | 910 | 1307 | 504 |
| An_Dun_raster3 | 2976 | N | 44.40 | 1.06 | 8.16 | 0.31 | 0.21 | 18.43 | 7.65 | 3.34 | 2.17 | 0.96 | 1.07 | 10.44 | 1.45 | 922 | 1347 | 524 |
| Ronas_Hill | 2989 | R | 50.13 | 1.09 | 9.22 | 0.31 | 0.24 | 20.36 | 6.03 | 2.79 | 2.41 | 0.95 | 0.98 | 3.89 | 1.21 | 1008 | 2066 | 126 |
| Tomb_of_the_Eagles | 3004 | R | 48.89 | 1.06 | 8.81 | 0.31 | 0.25 | 19.68 | 5.94 | 3.25 | 2.41 | 1.00 | 0.99 | 5.29 | 1.67 | 998 | 2059 | 623 |
| Easthouses | 3007 | R | 46.93 | 1.06 | 8.67 | 0.31 | 0.27 | 20.42 | 6.36 | 3.74 | 2.48 | 0.96 | 1.09 | 5.73 | 1.60 | 1046 | 1208 | 576 |
| Easthouses_offset | 3007 | R | 46.86 | 1.01 | 8.75 | 0.30 | 0.23 | 19.58 | 5.90 | 4.17 | 2.51 | 1.02 | 0.98 | 6.69 | 1.64 | 972 | 1203 | 536 |
| Gageac_et_Rouillac | 3010 | R | 47.84 | 1.08 | 8.59 | 0.31 | 0.22 | 20.63 | 6.06 | 3.45 | 2.55 | 1.00 | 0.99 | 5.21 | 1.60 | 1005 | 1157 | 1232 |
| La_Roque_Gageac_DRT | 3011 | R | 48.19 | 1.10 | 8.42 | 0.30 | 0.35 | 21.69 | 4.29 | 3.62 | 2.39 | 1.13 | 1.05 | 5.49 | 1.45 | 994 | 1286 | 1127 |
| Champagnac | 3013 | R | 42.34 | 1.01 | 7.59 | 0.22 | 0.27 | 21.38 | 7.12 | 4.79 | 2.28 | 0.82 | 1.12 | 8.98 | 1.62 | 959 | 1099 | 504 |
| Beaupouyet | 3015 | N | 46.21 | 1.11 | 8.42 | 0.31 | 0.32 | 20.92 | 6.07 | 3.84 | 2.25 | 0.89 | 1.95 | 6.20 | 1.15 | 844 | 1746 | 152 |
| Neuvic | 3018 | R | 48.29 | 1.09 | 8.59 | 0.30 | 0.60 | 19.83 | 4.64 | 4.06 | 2.38 | 1.12 | 0.91 | 6.34 | 1.46 | 1153 | 1271 | 675 |
| Lunas | 3020 | R | 48.36 | 1.14 | 8.95 | 0.32 | 0.21 | 20.63 | 5.58 | 3.36 | 2.37 | 1.01 | 1.03 | 5.00 | 1.67 | 966 | 1275 | 566 |
| Tamnies | 3022 | R | 49.66 | 1.11 | 9.41 | 0.27 | 0.22 | 21.73 | 4.75 | 2.76 | 2.48 | 1.13 | 1.01 | 3.73 | 1.19 | 1043 | 2505 | 176 |
| Biron | 3024 | R | 49.02 | 1.07 | 9.18 | 0.33 | 0.21 | 20.16 | 6.15 | 3.35 | 2.44 | 0.90 | 0.88 | 4.50 | 1.21 | 1096 | 2409 | 405 |
| Coutures_DRT | 3024 | R | 51.36 | 1.17 | 9.08 | 0.33 | 0.17 | 18.02 | 4.97 | 3.75 | 2.43 | 1.08 | 1.31 | 4.85 | 1.13 | 706 | 1488 | 667 |
| Labouquerie | 3026 | R | 48.61 | 1.18 | 9.06 | 0.33 | 0.09 | 19.29 | 6.88 | 3.39 | 2.46 | 0.82 | 1.28 | 4.81 | 1.37 | 875 | 1740 | 572 |
| Brantôme | 3027 | R | 46.37 | 1.08 | 8.58 | 0.33 | 0.25 | 19.94 | 6.45 | 4.32 | 2.38 | 0.88 | 0.84 | 6.46 | 1.53 | 985 | 1504 | 471 |
| Firbeix | 3028 | R | 48.07 | 1.05 | 8.95 | 0.32 | 0.14 | 21.17 | 5.07 | 3.81 | 2.41 | 0.95 | 0.88 | 5.67 | 1.17 | 861 | 1580 | 135 |
| Dordogne_DRT | 3031 | R | 46.17 | 1.02 | 8.73 | 0.27 | 0.19 | 18.20 | 5.10 | 5.53 | 2.34 | 0.93 | 1.21 | 8.57 | 1.31 | 1067 | 1915 | 241 |
| Dordogne_offset | 3031 | R | 46.89 | 0.97 | 8.83 | 0.29 | 0.19 | 18.02 | 5.17 | 5.26 | 2.33 | 0.93 | 1.03 | 8.39 | 1.29 | 1052 | 1910 | 210 |
| Limeyrat_DRT | 3034 | R | 48.26 | 1.01 | 8.92 | 0.30 | 0.23 | 19.38 | 4.83 | 4.32 | 2.43 | 0.97 | 0.92 | 6.43 | 1.38 | 1219 | 2454 | 532 |
| Limeyrat_offset | 3034 | R | 44.41 | 0.99 | 8.26 | 0.28 | 0.21 | 18.37 | 5.16 | 5.92 | 2.30 | 0.84 | 1.10 | 10.24 | 1.35 | 1136 | 2445 | 623 |
| Fleurac | 3035 | RT | 45.20 | 0.89 | 8.79 | 0.40 | 0.33 | 21.00 | 8.95 | 5.79 | 2.43 | 0.58 | 0.80 | 3.77 | 0.79 | 936 | 1103 | 231 |
| Fleurac_offset | 3035 | RT | 42.86 | 0.94 | 8.76 | 0.46 | 0.43 | 21.46 | 10.54 | 6.76 | 2.44 | 0.44 | 0.78 | 3.36 | 0.59 | 805 | 445 | 83 |
| Chalus_DRT | 3037 | R | 45.15 | 1.01 | 8.21 | 0.29 | 0.22 | 17.95 | 5.10 | 5.87 | 2.30 | 0.84 | 1.27 | 9.61 | 1.69 | 1027 | 2292 | 778 |
| Chalus_offset | 3037 | R | 47.35 | 0.98 | 8.59 | 0.27 | 0.23 | 16.92 | 5.37 | 5.23 | 2.35 | 0.91 | 1.24 | 8.39 | 1.67 | 1013 | 2382 | 755 |
| Plazac | 3040 | R | 48.72 | 1.02 | 9.26 | 0.28 | 0.18 | 20.65 | 5.39 | 3.50 | 2.24 | 0.98 | 0.90 | 5.06 | 1.31 | 1188 | 2026 | 372 |
| Manzac | 3042 | R | 47.86 | 0.97 | 9.00 | 0.29 | 0.22 | 21.75 | 5.81 | 3.28 | 2.54 | 0.92 | 0.94 | 4.64 | 1.33 | 1416 | 1766 | 378 |
| Pazayac | 3044 | R | 48.29 | 1.07 | 9.53 | 0.28 | 0.16 | 18.38 | 5.62 | 4.48 | 2.63 | 0.89 | 1.19 | 6.22 | 0.96 | 737 | 1351 | 145 |
| Sadillac | 3044 | R | 44.72 | 1.00 | 8.64 | 0.29 | 0.17 | 17.51 | 6.91 | 4.82 | 2.37 | 0.83 | 0.92 | 10.29 | 1.16 | 1004 | 1650 | 174 |
| Daglan | 3047 | R | 46.21 | 1.03 | 8.57 | 0.37 | 0.23 | 19.58 | 6.31 | 4.32 | 2.42 | 0.93 | 1.04 | 6.86 | 1.65 | 1127 | 2281 | 673 |
| Montrem_DRT | 3051 | R | 46.20 | 0.99 | 8.46 | 0.30 | 0.16 | 17.57 | 3.77 | 6.53 | 2.17 | 0.80 | 0.92 | 10.86 | 0.89 | 789 | 1497 | 313 |
| Peyrat | 3051 | N | 38.29 | 0.83 | 7.47 | 0.24 | 0.19 | 17.50 | 7.68 | 6.52 | 2.37 | 0.60 | 1.37 | 15.30 | 1.36 | 822 | 1145 | 171 |
| Nontron_offset | 3054 | R | 46.60 | 0.97 | 8.45 | 0.28 | 0.23 | 17.03 | 4.95 | 5.75 | 2.35 | 0.77 | 1.01 | 10.00 | 1.17 | 955 | 1800 | 362 |
| Nontron_triage | 3054 | R | 47.34 | 1.18 | 8.71 | 0.29 | 0.22 | 17.57 | 6.25 | 4.95 | 2.37 | 0.76 | 1.00 | 7.71 | 1.26 | 968 | 1905 | 411 |
| Nontron_DRT | 3055 | R | 50.16 | 0.98 | 9.06 | 0.29 | 0.22 | 17.39 | 4.68 | 4.39 | 2.51 | 0.87 | 1.03 | 6.78 | 1.09 | 950 | 1896 | 394 |
| Nontron_dump_2 | 3068 | F | 45.93 | 1.07 | 8.56 | 0.33 | 0.29 | 20.85 | 4.80 | 5.37 | 2.43 | 0.79 | 0.99 | 7.20 | 0.95 | 1141 | 2016 | 200 |
| Chassenon_raster1 | 3069 | V | 28.47 | 0.61 | 5.84 | 0.21 | 0.35 | 23.78 | 6.18 | 12.43 | 2.01 | 0.31 | 0.71 | 18.07 | 0.78 | 878 | 908 | 259 |
| Chassenon_raster2 | 3069 | V | 46.59 | 1.08 | 9.22 | 0.33 | 0.31 | 18.56 | 6.65 | 4.85 | 2.50 | 0.77 | 1.03 | 6.65 | 1.00 | 1139 | 2037 | 301 |
| Chassenon_raster3 | 3069 | V | 46.70 | 1.04 | 8.74 | 0.31 | 0.36 | 19.45 | 7.00 | 4.39 | 2.41 | 0.73 | 0.98 | 6.25 | 1.07 | 1187 | 2119 | 405 |
| Chassenon_raster4 | 3071 | V | 43.23 | 0.98 | 8.34 | 0.30 | 0.42 | 19.87 | 6.58 | 6.09 | 2.37 | 0.64 | 0.93 | 8.85 | 0.98 | 1077 | 1853 | 266 |
| Nontron_tailings | 3072 | F | 49.30 | 1.16 | 9.15 | 0.33 | 0.27 | 19.82 | 4.14 | 4.52 | 2.55 | 0.86 | 0.99 | 5.58 | 0.90 | 1205 | 2182 | 29 |

| Target | Sol | Type[2] | $SiO_2$ | $TiO_2$ | $Al_2O_3$ | $Cr_2O_3$ | MnO | FeO | MgO | CaO | $Na_2O$ | $K_2O$ | $P_2O_5$ | $SO_3$ | Cl | Ni | Zn | Br |
|---|---|---|---|---|---|---|---|---|---|---|---|---|---|---|---|---|---|---|
| **Carolyn Shoemaker formation: Glasgow member, Hutton interval** | | | | | | | | | | | | | | | | | | |
| Bogmill_Pow | 2660 | R | 36.15 | 0.94 | 8.12 | 0.28 | 0.27 | 19.49 | 8.01 | 7.70 | 2.58 | 0.37 | 0.87 | 13.49 | 1.34 | 1153 | 1403 | 397 |
| Cullivoe_DRT | 2660 | R | 50.33 | 0.99 | 9.55 | 0.29 | 0.28 | 17.26 | 7.60 | 3.97 | 2.79 | 0.89 | 0.91 | 4.26 | 0.62 | 683 | 963 | 68 |
| Cairnbulg | 2662 | R | 47.27 | 0.93 | 9.05 | 0.28 | 0.24 | 19.19 | 7.69 | 4.75 | 2.96 | 0.89 | 1.14 | 4.18 | 1.11 | 716 | 907 | 107 |
| Berwickshire_DRT | 2663 | R | 47.50 | 0.94 | 8.73 | 0.29 | 0.24 | 20.10 | 7.36 | 4.62 | 2.94 | 0.93 | 1.16 | 3.71 | 1.19 | 712 | 946 | 506 |
| Hutton_DRT_offset | 2665 | R | 50.21 | 1.00 | 9.34 | 0.29 | 0.25 | 17.41 | 6.75 | 5.29 | 3.26 | 0.89 | 1.07 | 3.02 | 0.98 | 661 | 947 | 248 |
| Hutton_triage | 2665 | R | 46.66 | 0.94 | 8.74 | 0.36 | 0.25 | 19.02 | 7.36 | 5.40 | 2.70 | 0.80 | 0.93 | 5.30 | 1.01 | 727 | 935 | 236 |
| Hutton_DRT_centre | 2666 | R | 50.50 | 1.00 | 9.53 | 0.28 | 0.25 | 18.03 | 6.16 | 5.05 | 3.38 | 0.94 | 1.12 | 2.63 | 0.88 | 658 | 938 | 219 |
| Liberton_Brae | 2666 | V | 40.60 | 0.85 | 7.62 | 0.25 | 0.25 | 16.25 | 17.11 | 3.31 | 1.86 | 2.14 | 0.97 | 6.67 | 1.42 | 1052 | 3433 | 486 |
| Moorfoot_Hills | 2666 | R | 42.04 | 0.92 | 8.54 | 0.30 | 0.33 | 20.69 | 7.78 | 7.27 | 2.89 | 0.74 | 1.00 | 5.46 | 1.68 | 749 | 1097 | 765 |
| Traprain_Law | 2667 | R | 48.42 | 1.00 | 9.03 | 0.30 | 0.25 | 18.74 | 6.72 | 5.18 | 2.93 | 0.93 | 1.25 | 4.12 | 0.71 | 597 | 1746 | 883 |
| Hutton_dump_centre | 2684 | F | 49.29 | 1.07 | 9.27 | 0.28 | 0.26 | 18.68 | 5.39 | 6.10 | 3.51 | 0.93 | 1.04 | 2.99 | 0.91 | 716 | 1191 | 70 |
| Hutton_dump_corrected | 2684 | F | 46.64 | 1.07 | 9.29 | 0.31 | 0.27 | 19.94 | 6.29 | 5.88 | 3.39 | 0.89 | 1.09 | 3.71 | 0.91 | 739 | 1598 | 131 |
| Hutton_tailings | 2686 | F | 50.55 | 1.06 | 9.46 | 0.31 | 0.25 | 19.23 | 5.58 | 5.28 | 3.68 | 0.96 | 1.12 | 1.43 | 0.84 | 698 | 988 | 21 |
| Dounreay | 2690 | V | 40.01 | 1.00 | 7.95 | 0.27 | 0.49 | 19.88 | 11.36 | 5.07 | 2.04 | 1.43 | 1.09 | 6.73 | 2.18 | 1283 | 1613 | 822 |
| Dunbartonshire_refined | 2691 | V | 26.38 | 0.58 | 5.09 | 0.14 | 6.33 | 39.65 | 8.57 | 3.60 | 1.57 | 0.24 | 0.62 | 4.89 | 1.97 | 893 | 1593 | 750 |
| **Carolyn Shoemaker formation: Benches unit - KHm-Gm transition** | | | | | | | | | | | | | | | | | | |
| Bablin | 2925 | R | 48.20 | 1.09 | 9.29 | 0.35 | 0.41 | 18.34 | 6.80 | 3.88 | 2.56 | 1.07 | 0.96 | 5.30 | 1.36 | 709 | 1397 | 558 |
| Bablin_offset | 2925 | R | 46.70 | 1.04 | 8.88 | 0.39 | 0.36 | 18.88 | 7.69 | 4.57 | 2.64 | 0.88 | 0.88 | 5.46 | 1.33 | 701 | 1129 | 429 |
| Garth_Ness | 2928 | R | 44.96 | 1.05 | 8.41 | 0.33 | 0.22 | 21.28 | 6.97 | 4.18 | 2.46 | 0.84 | 0.91 | 6.79 | 1.27 | 744 | 965 | 740 |
| Garth_Ness_offset | 2928 | R | 44.44 | 0.99 | 8.22 | 0.31 | 0.23 | 21.31 | 7.06 | 4.24 | 2.38 | 0.83 | 1.00 | 7.23 | 1.32 | 739 | 1000 | 910 |
| Rachan | 2931 | R | 49.63 | 1.07 | 9.37 | 0.27 | 0.24 | 21.03 | 5.35 | 2.66 | 2.55 | 1.15 | 0.60 | 4.82 | 1.02 | 723 | 1118 | 80 |
| Mail_Beach | 2933 | R | 49.45 | 1.13 | 9.40 | 0.29 | 0.22 | 20.40 | 5.63 | 2.59 | 2.72 | 1.21 | 0.80 | 4.66 | 1.07 | 806 | 1150 | 370 |
| Hunt_Hill_DRT | 2935 | R | 46.13 | 1.17 | 8.98 | 0.36 | 0.26 | 17.05 | 7.79 | 4.09 | 2.46 | 0.88 | 1.03 | 7.53 | 1.91 | 602 | 1654 | 366 |
| Muckle_Minn | 2935 | R | 46.32 | 1.05 | 9.39 | 0.31 | 0.30 | 18.31 | 8.19 | 3.96 | 2.58 | 0.83 | 1.00 | 5.73 | 1.63 | 790 | 1329 | 316 |
| Hart_Fell | 2938 | R | 44.60 | 1.08 | 8.39 | 0.31 | 0.26 | 19.39 | 8.44 | 3.18 | 2.30 | 1.00 | 0.93 | 7.77 | 1.81 | 955 | 2808 | 901 |
| West_Loch | 2940 | R | 47.45 | 0.98 | 8.83 | 0.35 | 0.35 | 21.43 | 6.37 | 2.61 | 2.55 | 1.29 | 0.83 | 5.28 | 1.17 | 867 | 1273 | 216 |
| Geesa_Water | 2942 | R | 45.86 | 1.06 | 8.57 | 0.36 | 0.38 | 19.22 | 7.48 | 3.63 | 2.42 | 1.08 | 0.91 | 6.88 | 1.72 | 857 | 1576 | 618 |
| St_Ninian | 2943 | R | 44.11 | 1.05 | 8.53 | 0.31 | 0.25 | 19.23 | 7.71 | 3.68 | 2.54 | 1.06 | 0.97 | 8.53 | 1.67 | 813 | 1135 | 575 |
| Ingliston | 2945 | R | 47.21 | 1.14 | 8.94 | 0.38 | 0.31 | 18.16 | 6.89 | 3.79 | 2.57 | 1.11 | 0.88 | 6.52 | 1.66 | 910 | 1619 | 815 |
| Lasswade_DRT | 2945 | R | 38.83 | 0.99 | 7.75 | 0.28 | 0.29 | 15.79 | 6.22 | 8.55 | 2.38 | 0.99 | 1.01 | 14.93 | 1.66 | 776 | 1121 | 850 |
| Giova_DRT | 2949 | R | 43.98 | 1.02 | 8.21 | 0.29 | 0.21 | 18.39 | 7.00 | 4.59 | 2.28 | 1.01 | 0.89 | 9.95 | 1.74 | 931 | 1878 | 611 |
| Giova_offset | 2949 | R | 43.86 | 1.03 | 8.22 | 0.32 | 0.21 | 17.81 | 6.76 | 5.38 | 2.32 | 0.94 | 0.93 | 10.09 | 1.75 | 871 | 1725 | 557 |
| Saughieside_Hill | 2951 | R | 45.28 | 0.99 | 8.16 | 0.41 | 0.26 | 19.25 | 5.36 | 5.28 | 2.33 | 1.07 | 0.95 | 8.75 | 1.42 | 859 | 1367 | 832 |
| Rest_and_Be_Thankful_DRT | 2955 | R | 43.86 | 0.99 | 8.43 | 0.29 | 0.21 | 17.65 | 7.34 | 4.39 | 2.45 | 0.85 | 1.00 | 10.30 | 1.88 | 925 | 1280 | 375 |
| Rest_and_Be_Thankful_offset | 2955 | R | 45.89 | 1.02 | 8.69 | 0.29 | 0.19 | 17.71 | 7.28 | 3.80 | 2.39 | 0.88 | 0.96 | 8.90 | 1.67 | 918 | 1220 | 408 |
| **Unconsolidated sediments** | | | | | | | | | | | | | | | | | | |
| Auld_Reekie | 2731 | SL | 44.23 | 0.96 | 9.23 | 0.53 | 0.42 | 19.62 | 9.00 | 7.07 | 2.64 | 0.44 | 0.81 | 4.31 | 0.61 | 478 | 238 | 29 |
| Balliekine | 2706 | SL | 43.44 | 1.02 | 9.30 | 0.48 | 0.40 | 18.83 | 9.08 | 7.24 | 2.55 | 0.52 | 0.80 | 5.47 | 0.72 | 480 | 324 | 40 |
| Airor | 2993 | SD | 43.03 | 0.92 | 8.12 | 0.38 | 0.43 | 22.03 | 11.43 | 6.95 | 2.25 | 0.33 | 0.82 | 2.69 | 0.43 | 1231 | 144 | 39 |
| Alba | 2313 | SD | 43.53 | 1.20 | 8.92 | 0.73 | 0.45 | 20.88 | 9.56 | 7.05 | 2.42 | 0.39 | 0.72 | 3.52 | 0.52 | 443 | 236 | 29 |
| Braewick_Beach | 2989 | SD | 42.49 | 0.93 | 8.63 | 0.54 | 0.42 | 21.77 | 10.90 | 7.05 | 2.49 | 0.37 | 0.76 | 2.97 | 0.53 | 823 | 219 | 44 |
| Burrowgate | 2558 | SD | 40.62 | 1.14 | 8.67 | 0.56 | 0.40 | 22.10 | 8.78 | 6.71 | 2.58 | 0.48 | 0.86 | 6.20 | 0.72 | 727 | 467 | 168 |
| Clackmannanshire | 2564 | SD | 42.72 | 0.99 | 9.10 | 0.53 | 0.44 | 20.63 | 9.73 | 7.22 | 2.62 | 0.45 | 0.77 | 4.08 | 0.58 | 570 | 213 | 22 |
| Dunoon | 2409 | SD | 42.58 | 0.86 | 8.72 | 0.40 | 0.41 | 21.35 | 11.39 | 7.02 | 2.52 | 0.42 | 0.74 | 2.93 | 0.48 | 1036 | 156 | 59 |
| Ellon | 2410 | SD | 44.25 | 0.88 | 10.03 | 0.31 | 0.35 | 18.16 | 8.23 | 7.37 | 2.79 | 0.56 | 0.94 | 5.27 | 0.68 | 862 | 269 | 96 |
| Gairsay | 2409 | SD | 44.59 | 0.90 | 9.06 | 0.48 | 0.42 | 20.13 | 9.76 | 7.25 | 2.53 | 0.40 | 0.75 | 3.12 | 0.48 | 529 | 210 | 38 |
| Nairn | 2410 | SD | 43.67 | 0.85 | 8.57 | 0.50 | 0.45 | 21.13 | 10.90 | 6.92 | 2.45 | 0.35 | 0.70 | 2.87 | 0.44 | 744 | 194 | 57 |
| Ratharsair | 2992 | SD | 42.19 | 1.11 | 8.74 | 0.72 | 0.47 | 21.94 | 10.36 | 7.15 | 2.44 | 0.38 | 0.75 | 3.12 | 0.48 | 562 | 228 | 32 |
| Traquair | 2995 | SD | 43.81 | 0.94 | 8.54 | 0.52 | 0.44 | 21.18 | 10.62 | 7.11 | 2.36 | 0.38 | 0.73 | 2.76 | 0.45 | 740 | 182 | 41 |
| **Table 2b.** | | | | | | | | | | | | | | | | | | |
| **Carolyn Shoemaker formation: Knockfarril Hill member (KHm)** | | | | | | | | | | | | | | | | | | |
| Glen_Etive_1_DRT | 2482 | R | 49.19 | 1.16 | 9.07 | 0.35 | 0.17 | 20.37 | 5.69 | 3.49 | 2.31 | 1.29 | 0.79 | 4.25 | 1.45 | 961 | 1819 | 685 |
| Glen_Etive_2_DRT | 2483 | R | 45.51 | 1.1 | 8.3 | 0.34 | 0.18 | 19.93 | 6.32 | 5.09 | 2.28 | 1.07 | 0.81 | 7.3 | 1.29 | 963 | 1759 | 922 |
| Glen_Etive_1_tailings | 2524 | F-DT | 47.38 | 1.3 | 8.59 | 0.4 | 0.22 | 23.57 | 5.41 | 3.85 | 2.14 | 1.28 | 0.77 | 4.13 | 0.49 | 1168 | 2327 | 153 |
| Glen_Etive_2_dump_corrected | 2552 | F-DBA | 38.64 | 1.14 | 7.3 | 0.36 | 0.25 | 20.16 | 4.63 | 9.66 | 1.81 | 1.04 | 0.69 | 13.17 | 0.71 | 1006 | 2372 | 82 |
| Mary_Anning_DRT | 2833 | R | 48.07 | 1.17 | 8.91 | 0.36 | 0.51 | 18.96 | 7.21 | 3.06 | 2.38 | 0.94 | 0.83 | 5.39 | 1.75 | 760 | 2415 | 558 |
| Mary_Anning_dump_2 | 2851 | F-DBA | 42.85 | 1.11 | 8.05 | 0.32 | 0.37 | 19.77 | 6.55 | 6.32 | 2.16 | 0.88 | 0.73 | 9.6 | 0.91 | 867 | 2124 | 56 |
| Mary_Anning_3_DRT | 2867 | R | 46.01 | 1.09 | 8.68 | 0.35 | 0.53 | 18.83 | 7.42 | 4.14 | 2.38 | 0.82 | 0.91 | 6.79 | 1.53 | 737 | 2321 | 472 |
| Mary_Anning_3_dump_2 | 2890 | F-DBA | 38.96 | 1.06 | 7.83 | 0.36 | 0.66 | 18.22 | 7.59 | 7.77 | 2.21 | 0.69 | 1.37 | 12.06 | 0.89 | 674 | 1826 | 58 |
| Groken_DRT | 2906 | R | 43.56 | 1.03 | 8.49 | 0.3 | 1.4 | 16.43 | 8 | 4.09 | 2.43 | 0.77 | 2.64 | 8.76 | 1.73 | 500 | 2175 | 329 |
| Groken_offset | 2906 | R | 41.73 | 1.03 | 8.45 | 0.29 | 1.2 | 15.18 | 8.72 | 4.64 | 2.48 | 0.67 | 2.22 | 11.5 | 1.57 | 388 | 1924 | 249 |
| Groken_tailings | 2921 | F-DT | 37.32 | 1.1 | 7.59 | 0.42 | 1.07 | 19.66 | 9.35 | 6.15 | 2.33 | 0.6 | 2.13 | 11.33 | 0.5 | 630 | 2118 | 254 |
| **Carolyn Shoemaker formation: Glasgow member (Gm)** | | | | | | | | | | | | | | | | | | |
| Hutton_DRT_centre | 2666 | R | 50.5 | 1 | 9.53 | 0.28 | 0.25 | 18.03 | 6.16 | 5.05 | 3.38 | 0.94 | 1.12 | 2.63 | 0.88 | 658 | 938 | 219 |
| Hutton_dump_corrected | 2684 | F-DBA | 46.64 | 1.07 | 9.29 | 0.31 | 0.27 | 19.94 | 6.29 | 5.88 | 3.39 | 0.89 | 1.09 | 3.71 | 0.91 | 739 | 1598 | 131 |
| Glasgow_1_DRT | 2749 | R | 53.11 | 1.12 | 9.5 | 0.32 | 0.11 | 17.28 | 4.65 | 3.47 | 2.32 | 0.96 | 1.19 | 4.46 | 1.15 | 1080 | 1103 | 607 |
| Glasgow1_dump_corrected | 2775 | F-DBA | 46.87 | 1.08 | 8.74 | 0.38 | 0.17 | 18.82 | 4.74 | 6.11 | 2.23 | 0.91 | 1.03 | 7.48 | 1.12 | 964 | 1039 | 200 |
| Nontron_offset | 3054 | R | 46.6 | 0.97 | 8.45 | 0.28 | 0.23 | 17.03 | 4.95 | 5.75 | 2.35 | 0.77 | 1.01 | 10 | 1.17 | 955 | 1800 | 362 |
| Nontron_DRT | 3055 | R | 50.16 | 0.98 | 9.06 | 0.29 | 0.22 | 17.39 | 4.68 | 4.39 | 2.51 | 0.87 | 1.03 | 6.78 | 1.09 | 950 | 1896 | 394 |
| Nontron_dump_2 | 3068 | F-DBA | 45.93 | 1.07 | 8.56 | 0.33 | 0.29 | 20.85 | 4.8 | 5.37 | 2.43 | 0.79 | 0.99 | 7.2 | 0.95 | 1141 | 2016 | 200 |
| **Stimson formation** | | | | | | | | | | | | | | | | | | |
| Edinburgh_DRT | 2703 | R | 42.59 | 0.77 | 8.24 | 0.5 | 0.48 | 20.84 | 9.76 | 5.9 | 3 | 0.86 | 0.68 | 4.6 | 1.67 | 406 | 274 | 54 |
| Edinburgh_dump_corrected | 2728 | F-DBA | 41.54 | 0.87 | 9.25 | 0.46 | 0.53 | 22.71 | 9.09 | 6.14 | 3.55 | 0.99 | 0.69 | 3.18 | 0.84 | 455 | 476 | 68 |

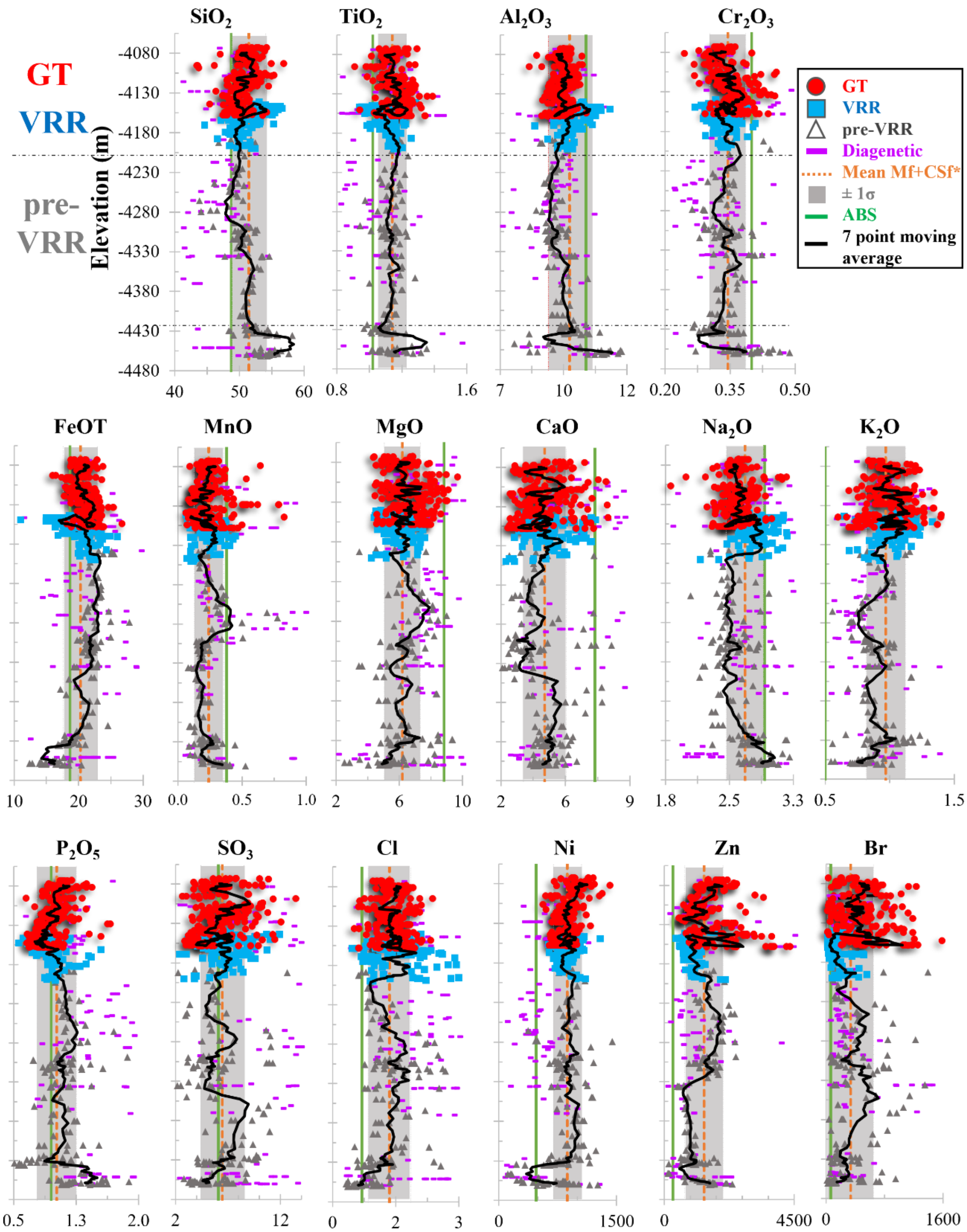


**Figure 2.** Major and trace element data versus elevation; all data weight percent, except Ni, Zn, Br (ppm). Data includes all data from Murray (Mf) and Carolyn Shoemaker (CSf) formation targets, divided into pre-Vera Rubin ridge targets (VRR) (grey symbols) (Table S1d), VRR targets (blue symbols) (Table 1c) and Glen Torridon targets (red symbols) (Table S1a). Diagenetic features are denoted by pink rectangles. Mean Mf+CSf is denoted by the dashed orange line, with ± 1 standard deviation shaded in grey. A seven point moving average (black solid line) was calculated to show the broad compositional trend with respect to increasing elevation (and increasing sol). Average basaltic soil [ABS; O' Connell-Cooper et al., 2017] is denoted by green solid line

### 3.3. Statistical treatment of APXS data

Standard univariate analysis results (mean, standard error, z-scores and % change from mean Murray and Carolyn Shoemaker formations concentrations [“Mf+CSf”] (number of targets = 488 bedrock and fines targets; Supplemental Text S2a) are given in Table S1. Unless otherwise stated, all data discusses in this paper are in the form of element/Si molar ratios. Si was assessed to be a suitable denominator, as >95% of bedrock targets fall within the normal range (<±1.96) when assessing via z-scores (Table S1). However, values for drill fines and diagenetic features typically fall outside the normal range. Differences in concentrations between members/subunits for a given element identified were analyzed for statistical significance. Distribution was determined to be non-normal for most populations (Shapiro-Wilk test), with unequal variances (Levene’s test). Kruskal-Wallis tests were used to determine if any statistically significant differences existed within the dataset for a given element. Games-Howell post-hoc tests determined which pairings showed differences (Tables S5-7). Pearson correlation coefficient analysis (r) results were calculated to identify compositional trends (Table S3). Principal Component analysis (PCA) was conducted, using transformed molar/Si ratio data to identify major elemental trends.

Agglomerative Hierarchical Clustering analysis (AHCA) was run to investigate similarities within members and to identify, if possible, alteration trends (Supplemental Text S2c for discussion; Tables S5-7; Figures S8, S10-11). All data was in the form of $Log_{10}$[element/Si] mole ratios. For each data set, three model parameters were run. Model A includes all elements routinely reported on by APXS. Following Mittlefehldt et al. [2018, 2021], Model B excludes the volatile elements S, Cl, Br, to minimize the effect of such variable elements on the bedock clustering. Model C excludes S, Cl, Br and the mobile elements Mn, P, Zn, Ni to examine the extent of alteration [e.g., Mittlefehldt et al. 2018, 2021].

# 4. APXS compositional results and statistical analysis

## 4.1 Murray formation – Jura member

### 4.1.1. Jura member within Glen Torridon (herein Jm_GT)

The Jm_GT was previously subdivided, based on morphological expression, into the "rubbly_Jura" and "coherent_Jura" respectively [e.g., O'Connell-Cooper et al., 2021]. A strong inverse relationship between potassium and grain size is identified throughout Jm_GT. The dominant "rubbly" morphology primarily comprises finely laminated K-rich mudstones and angular to rounded pebbles (Figures S2a-d). The compositional similarity between the loose pebble regolith and the flat lying patches suggests that the pebbles are locally derived (Figures 3a-b). The less abundant "coherent Jura" comprises coarser grained, magnesium-rich targets. Although high-K targets are the dominant morphology, both Jm_GT drill targets, Aberlady (*AL*; sol 2370) and Kilmarie (*KM*; sol 2384), are co-located on adjacent high-Mg blocks (Figures 1, S1, S2e), due to the difficulty in finding a suitable, drillable target within the rubbly high-K material.

The K-Mg relationship within Jm_GT targets is of particular interest, with 93% of samples falling into compositional endmembers, defined by "K/Si>mean Mf+CSf>Mg/Si" (high-K-facies) *or* "K/Si<mean Mf+CSf <Mg/Si" (high-Mg-facies) (Tables S1, S5a). A small subset of targets (n=6) show intermediate K and Mg, falling outside of the compositional endmembers defined above – these are grouped herein with the high-Mg facies. There is no overlap in either K or Mg concentrations between high-K and high-Mg facies (Figure 3a), and limited overlap for Zn and Mn (depleted in high-K-facies, enriched in high-Mg-facies) (relative to mean Mf+CSf)

(Figure 3b). Univariate correlation analysis identifies strong negative Pearson correlation coefficients (r) between K-Mg (r: -0.90), K-Mn (r: -0.68) and K-Zn (r: -0.63), and positive correlations between Mg, Mn and Zn (r: +0.58 to +0.65) (Figures 3a-b; Table S3a). These relationships (K, Mg, Mn, Zn) are not identified for the Mf+CSf in general, except in the Blunts Point (BPm): K-Mg r=-0.80; Mg-Zn-Mn r=+0.47 to +0.59) and Sutton Island (SIm) members (Mg-Zn-Mn r=0.56 to 0.62) (Table S3f). Statistically significant variance is identified between the two facies for all elements, except Ti, Al, Cr, Fe, Na, Br, which have broad in compositional ranges for both types (Table S5d; Figure 7a).

**4.1.2. Jm_GT Agglomerative Hierarchical Clustering Analysis (AHCA)**

AHCA was performed on Jm_GT bedrock (n=40), using model parameters described previously (Section 3.3; Supplementary Text S2b). For all three models, at cluster size K=6 ($K_6$), two groups are formed, falling along previously defined facies lines: high-K facies targets dominate Group A, whilst Group B consists of high-Mg facies and intermediate-facies targets (Table S5a; Figures S8a-d). Models are very similar, with 90% (n=36) of targets falling into the same group, and the majority falling into the same cluster. For all models, the target "*Haddington*" (sol_2408; AL+KM drill locale) which is high-K but also has very high Mn and Zn, falls into Group B. For Models A+B, Group A contains only high-K targets, but gains four intermediate-Mg targets (with moderate Mn, P, Zn) for Model C. The high-K target *Hill of Skares* clusters within Group A for Models A+C, but Group B for Model B only.

**4.1.3. Jm_**GT Multivariate Principal Component Analysis (PCA)

PCA analysis was applied to the AHCA Model A results to identify major trends (Figure S9a). Group A ($C_1$-$C_3$, primarily high-K-facies, n=18) is characterized by a trend to higher K, Si, Ni, Fe and Group B ($C_4$-$C_5$, primarily high-Mg targets, n=22) to higher values for all other elements. Calculating percentage change in means, relative to mean Mf+CSf (Figure S9b), Group A trends to depleted Mn, Mg, Ca, P, S, Cl, Zn. Group A is relatively homogenous, but with enrichment Ni in $C_1$, Al, Cr, Na in $C_2$ (r=+0.87 for Al+Cr), Cl in $C_3$ and a marked Br depletion in $C_2$ but enrichment in $C_3$. Group B shows strong differences between clusters, with some evidence for geographical clustering. $C_5$ (targets from Woodland Bay area) are enriched in Mn, Mg, Na, S, Cl, Zn, Br. $C_6$ (predominantly intermediate targets, plus *Haddington*) is depleted in Ca, S, P but very enriched in Br. $C_4$ (primarily located in the Aberlady and Kilmarie drill locale) is enriched in both Mn and Zn, with highest Zn values for Jm_GT in this cluster.

**4.2 Carolyn Shoemaker formation – Knockfarril Hill member**

**4.2.1. Knockfarril Hill member (KHm)**

APXS analyses of KHm targets show that fine-grained targets are enriched in K (defined as: K/Si>mean Mf+CSf>Mg/Si); whilst coarser targets are enriched in Mg (defined as: K/Si<mean Mf+CSf <Mg/Si) (Tables S1, S6a). The paired *Glen Etive* drill holes (GE1 and GE2; sols 2486 and 2527, respectively) are co-located at the southern end of the Visionarium (an area of scarps and ridges, Bennett et al., this issue) in a layer of slightly finer-grained [Rivera-Hernandez et al., 2020a; Minitti et al., 2021] high K, moderate Mg material (Figures 1, 3c-d, S1). The paired *Mary Anning* drill holes (MA1 and MA3; sols 2838 and 2870, respectively), located in coarser grained Mg-rich sandstones, mark a brief detour from the MSAR (once the main KHm campaign had finished) to facilitate a TMAH SAM experiment [Williams et al., 2021] (Figures 1, S1). The nodular MnO-$P_2O_5$ rich target *Groken* (GR; sol 2910), co-located with MA, was the focus of an opportunistic drill campaign (Figures 1, S1, S3e).

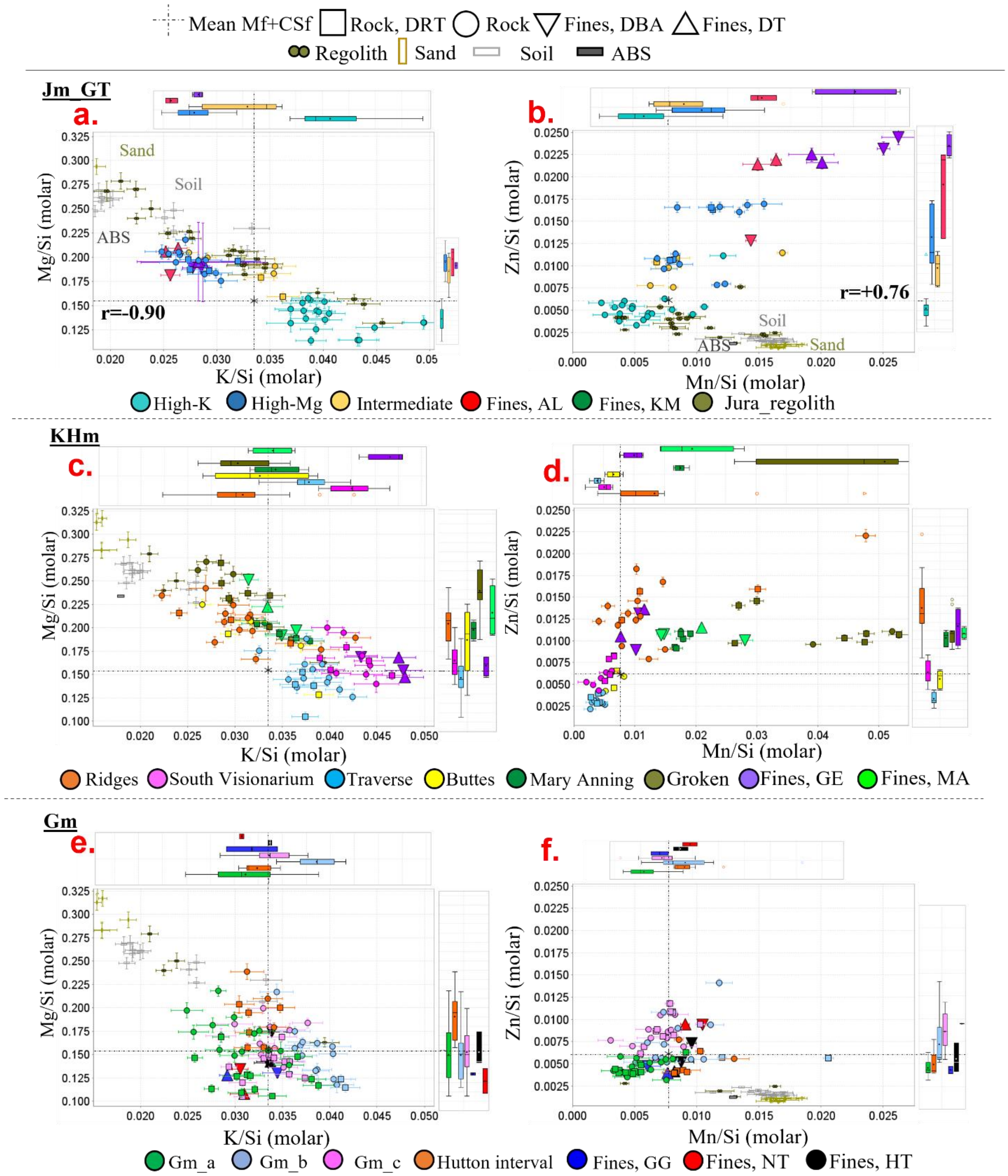


**Figure. 3.** K-Mg and Mn-Zn compositional data (x-y graphs with Tukey outlier plots), for bedrock and fines targets (no diagenetic features). All data is in X/Si molar form. Members are subdivided into facies or subunits (see text for details). Tukeys: central box is mid 50% of data (Q1-Q3). Outliers (circles) are > 1.5* (Q3-Q1) from the central box; far outliers (triangles) are > 3.0 * (Q3-Q1). Mean Mf+CSf = mean Murray and Carolyn Shoemaker formations (Tables S1, S2; Supplementary Text S2a). ABS = Average Basaltic Soil [O'Connell-Cooper et al., 2017]. **3a-b.** Jura member, Glen Torridon (Jm_GT). **3c-d.** Knockfarril Hill member (KHm). **3e-f.** Glasgow member (Gm).

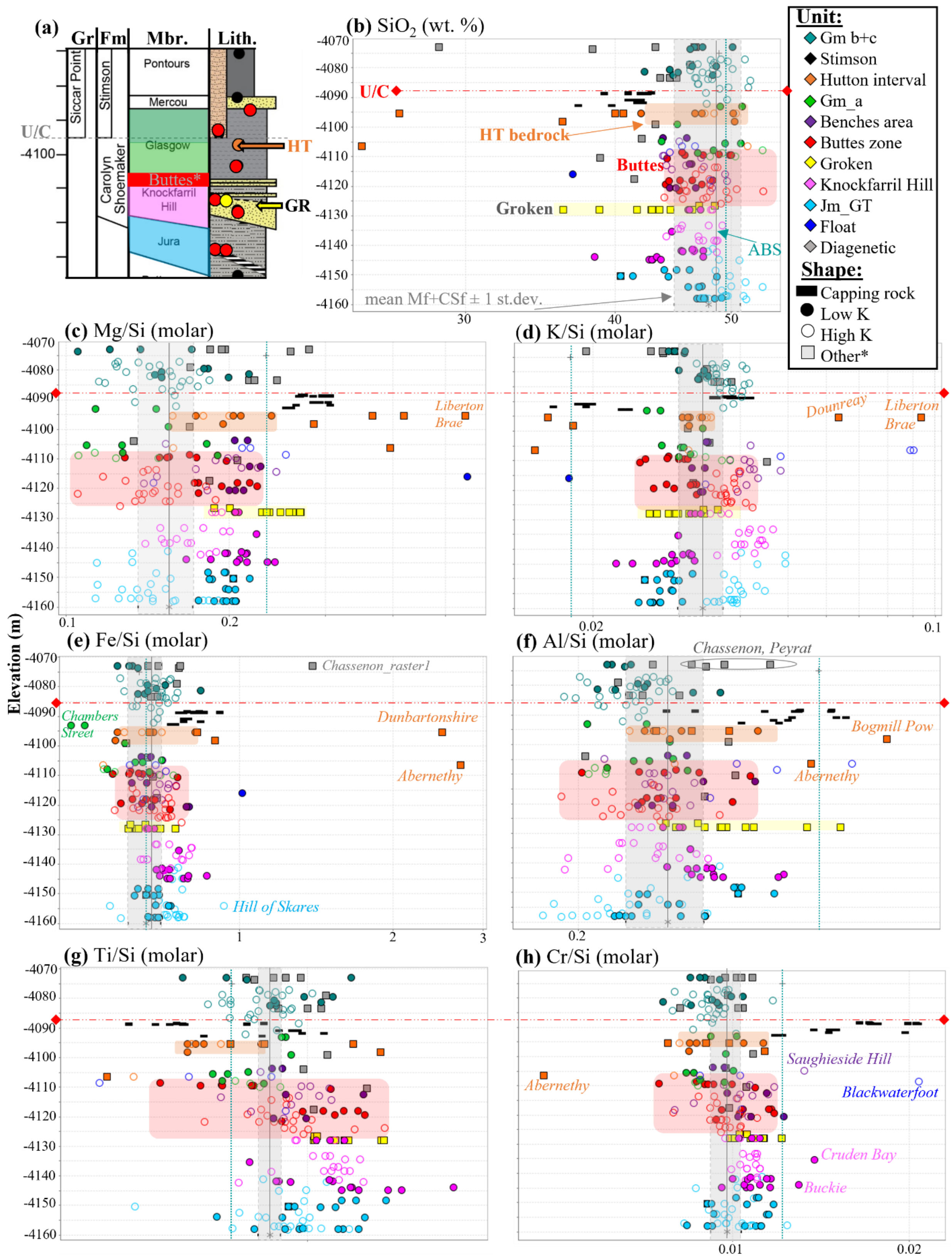
(a)
Gr
Fm
Mbr.
Lith.
Siccar Point
Stimson
Pontours
Mercou
U/C
-4100
Glasgow
HT
Carolyn Shoemaker
Buttes*
Knockfarril Hill
GR
Jura
(b) SiO$_2$ (wt. %)
U/C
HT bedrock
Buttes
Groken
ABS
mean Mf+CSf ± 1 st.dev.
(c) Mg/Si (molar)
Liberton Brae
(d) K/Si (molar)
Dounreay
Liberton Brae
(e) Fe/Si (molar)
Chassenon_raster1
Chambers Street
Dunbartonshire
Abernethy
Hill of Skares
(f) Al/Si (molar)
Chassenon, Peyrat
Bogmill Pow
Abernethy
(g) Ti/Si (molar)
(h) Cr/Si (molar)
Saughieside Hill
Abernethy
Blackwaterfoot
Cruden Bay
Buckie
Elevation (m)
Unit:
Gm b+c
Stimson
Hutton interval
Gm_a
Benches area
Buttes zone
Groken
Knockfarril Hill
Jm_GT
Float
Diagenetic
Shape:
Capping rock
Low K
High K
Other*

**Figure 4.** Major oxide concentrations within Glen Torridon. **4a.** Stratigraphic column after Fedo et al., this issue, with study area in colour. **4b-h.** All data (X/Si) molar (except **4b**, in weight percent) versus elevation (metres); logarithmic x-axis for all plots (**b-h**). The red dashed line represents the Siccar Point Basal unconformity, the dark grey line mean Mf+CSf, the grey shaded areas ± 1 standard deviation, and the green dashed line Average Basaltic soil (ABS) [O'Connell-Cooper et al., 2017]. The buttes transition zone is shaded in red for each plot.

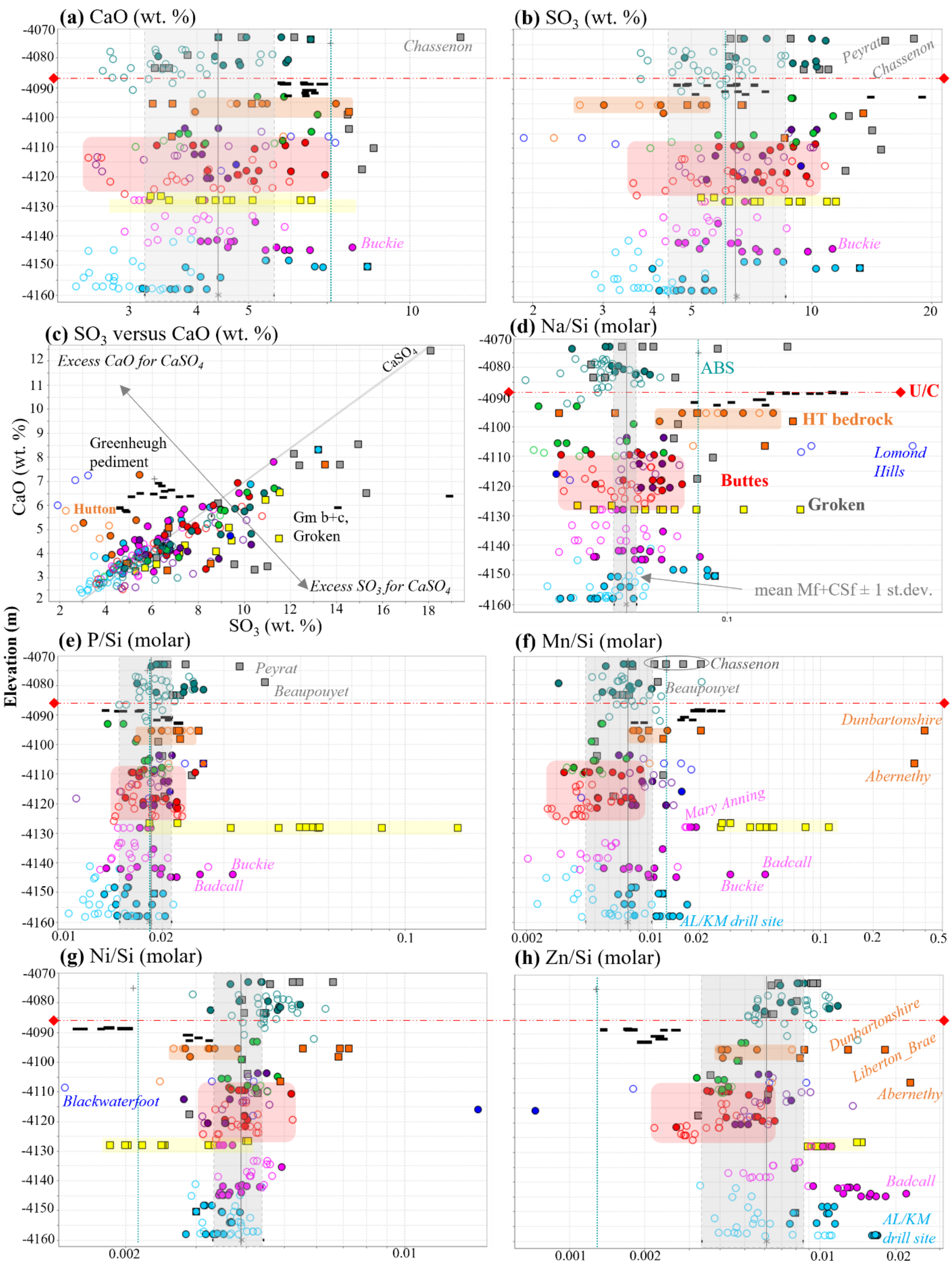
(a) CaO (wt. %)
Chasseron
Buckie
(b) SO3 (wt. %)
Peyrat
Chasseron
Buckie
(c) SO3 versus CaO (wt. %)
Excess CaO for CaSO4
CaSO4
Greenheugh pediment
Hutton
Gm b+c, Groken
Excess SO3 for CaSO4
CaO (wt. %)
SO3 (wt. %)
(d) Na/Si (molar)
ABS
U/C
HT bedrock
Lomond Hills
Buttes
Groken
mean Mf+CSf ± 1 st.dev.
Elevation (m)
(e) P/Si (molar)
Peyrat
Beaupouyet
Buckie
Badcall
(f) Mn/Si (molar)
Chasseron
Beaupouyet
Dunbartonshire
Abernethy
Mary Anning
Badcall
Buckie
AL/KM drill site
(g) Ni/Si (molar)
Blackwaterfoot
(h) Zn/Si (molar)
Dunbartonshire
Liberton_Brae
Abernethy
Badcall
AL/KM drill site

**Figure 5.** Mobile element concentrations within Glen Torridon (Legend as per Figure 4). **5a-b**. CaO and $SO_3$ weight percent versus elevation (metres); logarithmic x-axis. **5c**. $SO_3$ versus CaO (weight percent). **5d-h**. Concentrations (X/Si molar) versus elevation (metres); logarithmic x-axis.

Compositional endmembers are less well developed within KHm than Jm_GT, with 35% of samples exhibiting both Mg and K higher than mean Mf+CSf. However, targets with highest K concentrations continue to trend to lower Mg, Mn, Zn, whilst highest Mg targets exhibit lower K, and higher Mg, Mn, Zn (Figures 3c-d; Tables S3, S6a). The KHm shows compositional variation with location and can be subdivided into five broad units, with statistically significant differences identified between units (Table S6d; Figures 3c-d, 7A).

(1) ***Ridge*** targets (dominated by high-Mg/low K targets, number of targets (n) =16), encompassing Teal ridge and Harlaw rise, are characterized by depletion in K, but trend high for other elements, with highest mean Ti, Al, Cr, Fe, Mg, Na, P, Zn concentrations. (2) Post-ridge targets at the southern end of the Visionarium (***South_Vis***) (dominated by high K/moderate Mg targets, n=12), including the Glen Etive (GE) drill sites. (3) ***Traverse*** targets (dominated by high-K/low Mg targets, n=16) are a broad group of post-GE targets, incorporating five targets from the traverse to the buttes, and eleven along the base of the buttes, to the edge of Western butte. South_Vis targets are enriched in Cr, Cl, Ni, Br but depleted in P, whilst traverse targets exhibit the opposite pattern. (4) ***Butte*** targets (a mix of high-K + high-Mg targets, n=5), along the contact with the overlying Glasgow member (Gm), have the highest mean Ca, S, but lowest Al, Cl, with Fe concentrations amongst the lowest identified in KHm. (5) Mary Anning (***MA***) drill site (high-Mg/low to moderate K targets, n=6) targets exhibit the highest mean Mn (excluding the Groken locale and other outliers) and differ from the ridge targets (also high-Mg-facies) in that they have low mean Fe, Ca, P. Although the Groken (GR) drill target is co-located with MA, they exhibit an anomalous composition, with very high z-scores (Table S1) – targets have very

high mean Al, Mn, Mg, Na, P, S, Cl but very low Ni. In particular, MnO is very high, with concentrations up to 2.44 wt. % observed, compared to the 0.35 ± 0.04 wt% found in average basaltic (MER and MSL) soils (ABS) [O'Connell-Cooper et al., 2017]. Accordingly, they are treated separately from other KHm targets, and are not included in the AHC analysis below.

#### 4.2.2. KHm Agglomerative Hierarchical Clustering Analysis (AHCA)

AHCA confirms the validity of the KHm geographical and facies divisions. Three AHC models (Section 3.3) were run using $Log_{10}$[X/Si] (molar) data for bedrock targets only (n=55) (no fines). Ideal cluster size was identified using the "elbow method" as $K=6$ ($K_6$).

All models result in two major groupings (Table S6a; Figures S10a-d). Models B (no S, Cl, Br) and C (also excludes Mn, P, Zn, Ni) resulted in very similar cluster organizations with two broad groupings, each dominated by either high-K or high-Mg targets. 84% of targets remain in the same group regardless of model, with Group A dominated by high-K (variable Mg, typically low to moderate) South Vis and traverse targets (18% ridges, buttes; *no* MA targets) and Group B comprising high-Mg targets (ridges, buttes, MA) only. Model A shows the strong effect of S enrichment in the ridge targets, with these targets in a separate group to all other targets (Figure S10b). For model B, distance between class centroids (Table S6b) confirms the similarity between Group A clusters (distances ≤0.427) and between Group B clusters (0.356). For model C, distances are slightly higher: Group A ≤0.234; Group B s ≤0.279.

### 4.3 Carolyn Shoemaker formation – Glasgow member

#### 4.3.1. Glasgow member (Gm)

The traverse across the Glasgow member (Gm) was bisected by a detour into Knockfarril Hill (KHm) (sols 2826-2921) to facilitate drilling at MA (Figure 1) in support of the SAM TMAH experiment [Williams et al., 2021]. Gm is split herein into pre_MA (***Gm_a***) and post_MA (***Gm_b***) (Tables S1, S7a; Figures 1b-d, S4). The post_MA unit is further subdivided, with the identification of a sub-unit (***Gm_c***) which skirts along the Sands of Forvie, and up to the base of Mont Mercou (Figure 1c-d, S4). The boundaries of this subunit are based on recent CRISM mapping by Hughes et al. [2021, this issue], who identified a rougher "rubbly" or fractured texture in this area. Three targets were drilled in Gm. Drill target *Glasgow* (GG; sol 2754) was drilled in the buttes area (Gm_a), whilst *Nontron* (NT; sol 3056) was drilled in Gm_c bedrock at the base of Mont Mercou. An additional target *Hutton* (HT; sol 2668) was drilled within the "**Hutton interval**", a zone of Gm rocks just below the Basal Siccar Point unconformity and in contact with the overlying Greenheugh pediment, which are treated herein as a separate but related unit.

The abrupt change at Central butte from cross-stratification structures to thin laminations, coupled with a sharp increase in diagenetic features (Figure S6), delineates a sharp sedimentological contact between KHm and Gm [Bennet et al., this issue; Fedo et al., this issue]. However, APXS analyses indicate a subtle geochemical transition between KHm and Gm in the area of the buttes (Section 5.4), marked by a trend to lower means, especially for Mg, Ca, Mn, Ni, Zn, Br (Figures 4c, 5a, 5f-h). Statistically significant variance was not identified for any element (except K/Si), indicating a degree of similarity.

APXS analyses also reveal geochemical differences between the pre- and post-MA Gm units (Gm_a, Gm_b) and subtle trends of change across the lateral extent of Gm (from the buttes to Mont Mercou) (Figures 3-5, 6b). Post_MA Gm targets trend to higher Fe, K, plus mobile (Mn, P, Zn, Ni) and volatile elements (Cl, Br), than pre_MA targets, with lower concentrations for all other elements (Tables S1-2). Statistically significant variances are identified between Gm_a and both post_MA units (Mn, K, Cl, Zn, Ni), between Gm_a & Gm_b only (Al, Fe, Ca, S) and Gm_a

& Gm_c only (P) (Table S7d). Minor compositional differences are also identified in the post_MA eastward traverse, from Gm_b to Gm_c, with decreases in Ti, Fe, Mn, K, Cl, and increases for all other elements; K, S, Ca show statistically significant variance (Table S7d).

The strong correlation relationships (K, Mn, Mg, Zn), key to defining the lower GT units, are weakly developed or absent in Gm as a whole (Table S3c). A negative K-Mg correlation is identified in Gm_b (r=-0.83), and a positive Mg-Mn correlation in Gm_a (r=+0.67); positive correlations between Zn and Mg+Mn are absent. However, a moderate positive correlation between Ni and Zn is identified in both Gm_b (r=+0.54) and Gm_c (r=+0.63) – this correlation is not identified in any GT unit.

**4.3.2. Gm Agglomerative Hierarchical Clustering Analysis (AHCA)**

Three AHCA models (Section 3.3; Supplementary Text S1) were run on the Glasgow member data, using $Log_{10}$[X/Si] (molar) data for bedrock targets only (n=63), for an ideal cluster size of $K=7$ ($K_7$) (Tables S7a-c; Supp. Figs. S11a-d). All models resulted in two major groupings, with 51% of targets remaining in the same group regardless of model. For Models A (all elements included) and B (excluding volatiles S, Cl, Br), 68-84% of all Gm_a targets fall in Group A, whilst 93-100% of Gm_b targets and 70-78% of all Gm_c targets fall into Group B (Table S7c), suggesting a compositional divide between the pre_MA (Gm_a) and the post_MA (Gm_b+Gm_c) units. This divide is not as striking for Model C (no volatiles, *plus* no Mn, Zn, Ni, P), where Gm_a and Gm_b targets are divided equally between Groups A and B, but Gm_c is found predominantly in Group B.

Comparing Models A and B, overlap targets (i.e., in the same group for both models) are roughly split evenly between the three Gm units, suggesting the contribution of volatile elements is relatively uniform across the Glasgow member. However, comparing Model B to Model C, overlap targets are 67% Gm_a, 7% Gm_b and 27% Gm_c, indicating that mobile elements (Mn, P, Zn, Ni) have a larger effect on composition (Table 7c). This can be attributed to the much lower levels of all four mobile elements in Gm_a. Zn and Mn are depleted in the transition zone from KHm to Gm at the buttes (Section 5.4), whilst both P and Ni are enriched in the post-MA units, with concentrations increasing with distance from the buttes and proximity to Mont Mercou.

**4.3.3. Hutton interval**

The Hutton interval (***Gm_HT***) (sols-2660-2691) (Tables 2. S1) is a layer of Gm bedrock and complex vein networks that occurs at the top of Tower Butte (Figures 1c, S5) below the Siccar point unconformity and in contact with the overlying Greenheugh pediment (GP) [see also Thompson et al., this issue for further discussion]. Although this interval contains the characteristic thin laminations that mark it as part of the Gm, a unique geochemical and mineralogical signature was documented here by APXS [this paper; Thompson et al., this issue], ChemCam [Dehouck, et al., this issue; Gasda et al., this issue] and CheMin [Thorpe et al., this issue]. Relative to mean underlying Gm_a bedrock, Hutton bedrock trends to enriched Mg, Na, Mn, and depleted S, Ni (Tables 2, S1; Figures 4c, 5b, 5d, 5f-g, 6b). Although S is depleted, Ca is not, indicating that a decoupling of Ca and S (Figure 5c). Additionally, some samples trend to low Ti, and high Al, P, Zn, (Figures 4g, 4f, 5e, 5h, 6b). A similar geochemical composition is identified at the highest point achieved by *Curiosity* on Western Butte in the bedrock target *Buchan Haven* (sol_2640) and vein target *Abernethy* (sol_2642) (Tables 2, S1). The correlations between K, Mn, Mg and Zn identified in other GT units are completely absent from the Hutton interval. Evidence for more alteration with increased proximity to GP is manifest in the form of more abundant nodules and veins. Complex FeO-MnO-rich (*Dunbartonshire (sol_2691)*, *Abernethy*: FeO 40 wt.%, MnO 5-6%) and MgO-$K_2O$-rich (*Liberton Brae (sol_2666)*: MgO 17 wt. %, $K_2O$ 2 w%) vein networks are identified at both at Hutton and Western Butte (Figure S5).

**4.4. Benches**

The “benches” unit represents a second transition between KHm and Gm (Figure 1d), through a series of resistant topographic “benches” with rubbly bedrock in between benches [Bennet et al., this issue]. However, unlike the clear facies transition identified at Central Butte, the “Benches” transition zone is not well defined stratigraphically, resulting in some ambiguity about whether this unit is more correctly placed with KHm or Gm. Targets are in family with other Glen Torridon bedrock (Tables 2, S1), but there are some distinctions (Figures 4-5). Coherent targets (e.g., *Muckle Minn*, sol_2935) which comprise the bulk of APXS targets here, have higher Mg/Si than mean Mf+CSf, whilst rubbly targets (e.g., *Mail Beach*, sol_2933) have high K/Si (i.e., > mean Mf+CSf). However, moderate targets (high K *plus* high Mg) are more common in the Bench unit than previously described units, comprising >50% of bench targets. The target *Hart Fell* (sol_2938) has both high Mg and K, but also very high Zn (2808 ppm). There are also examples of a “chaotic” texture, in the high-Mg *Garth Ness* target (sol_2928), which is not reflected in the composition; the benches exhibit the highest mean Mg/Si, K/Si, Na/Si, S/Si and Cl/Si for any GT bedrock facies or subunit (excluding the Hutton interval, Groken and other diagenetic targets). Similar to the KHm-Gm transition zone at the buttes, mean Zn/Si trends low, however Mn/Si trends high.

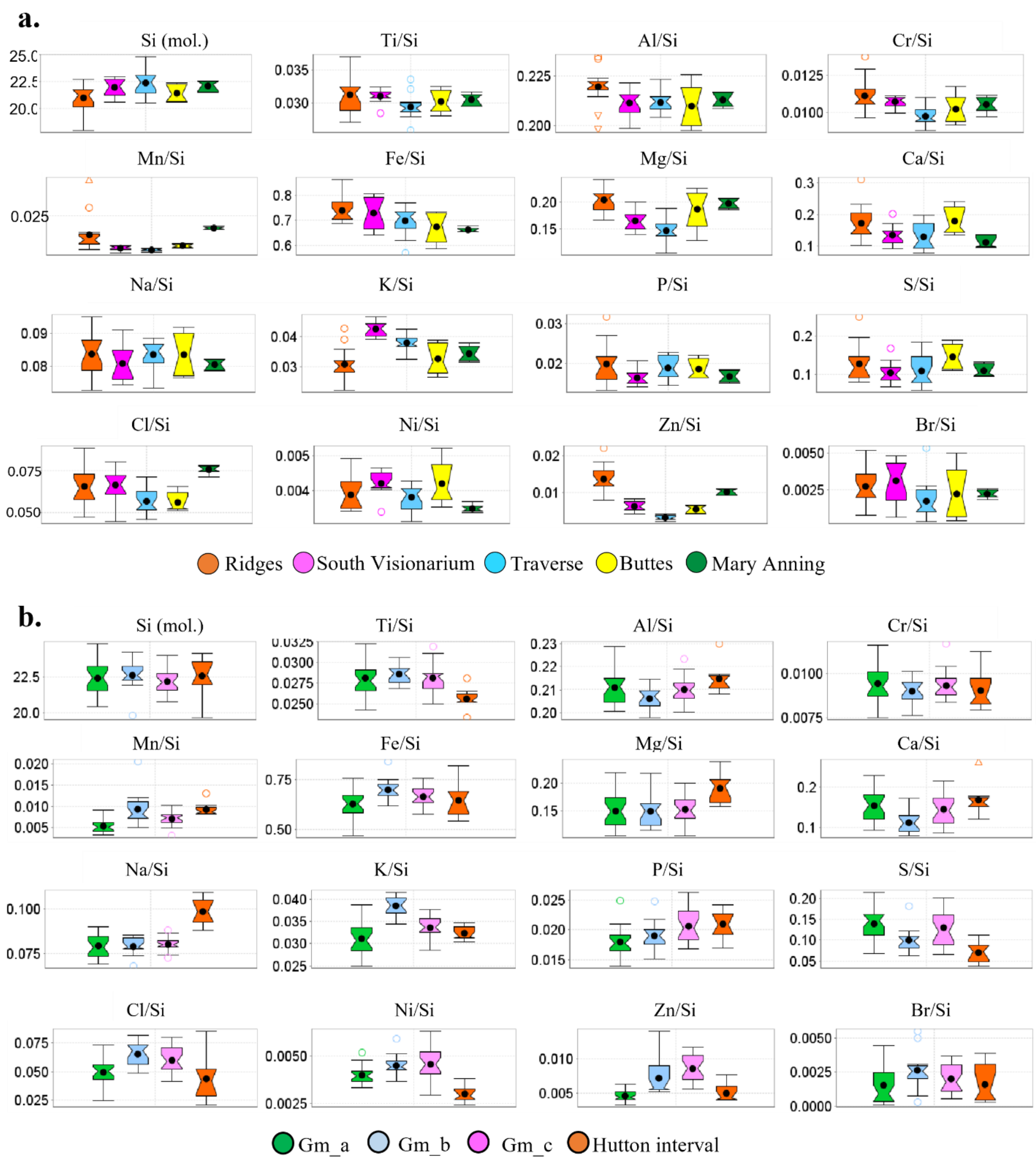


**Figure 6. Tukey plots, showing compositional trends for Knockfarril Hill and Glasgow member subunits. 6a.** Knockfarril Hill (KHm) subunits, defined by geographical location (Table S1-S2, S6). **6b.** Glasgow (Gm) subunits and Hutton interval (Table S1-S2, S7). Tukey plot interpretation: Black circle is mean value for a given unit. The central box represents the mid 50% of data (Q1-Q3). Outliers (circles) are > 1.5* (Q3-Q1) from the central box; far outliers (triangles) are > 3.0 * (Q3-Q1). All data is in element/Si (molar) form except first plot (Si molar) for both 6a and 6b.

**4.5. Unconsolidated sediments in Glen Torridon**

Twelve unconsolidated sediment targets were analyzed during the traverse to Mont Mercou (Table 2, S1). All but two samples were active sands, using S, Cl, Zn abundances as a proxy for dust cover and, by implication, activity levels. All sand targets are in family with active sands analyzed prior to the ridge. Offcrest samples show enrichment in T-Cr, a trend previously identified in the second phase of the Bagnold Dunes campaign and onwards [O'Connell-Cooper et al., 2018]. Crest samples typically show enrichment in Mg-Ni. Grain size and depositional settings of samples are discussed in Weitz et al. [this issue]. In contrast, *Balliekine* (sol_2706) and *Auld Reekie* (sol_2731), both overlying Stimson formation substrate on the Greenheugh pediment, plot with soil measurements, such as *Portage* and other soil targets analyzed prior to the Bagnold Dunes campaign, which are in family with average basaltic soil (ABS) from the MSL and MER missions [O'Connell-Cooper et al., 2017].

**4.6. APXS Drill fines analysis – comparison to host bedrock**

Ten holes were drilled in Murray and Carolyn Shoemaker bedrock targets during the Glen Torridon campaign [Jm_GT, n=2; KHm, n=5; Gm, n=3] (Figs. 1, 3a-f, S1; Tables 2a-b, S1), with an additional target in the Stimson formation (Sf) (*Edinburgh* (EB), on the Greenheugh pediment (discussed in detail in Thompson et al., this issue). Targets represent a variety of bedrock, as defined by K and Mg: (1) low K, high Mg: *Aberlady* (AL), *Kilmarie* (KM); (2) high K, moderate Mg: *Glen Etive* 1+2 (GE1, GE2); (3) moderate K, high Mg: *Mary Anning* 1+3 (MA1, MA3), *Groken* (GR); (4) moderate K, low Mg: *Glasgow* (GG), *Nontron* (NT), *Hutton* (HT) (Table 2b; Figure S1). Drill fines typically follow the trend of host bedrock, but there are some variations, both relative to host bedrock, and between DBA and tailings samples.

Cl trends to lower for drill fines than bedrock, with lower concentrations for all tailings than DBA samples, except KM DBA. Br concentrations in fines are typically ≤ host bedrock for all samples, but AL, KM, and MA1 tailings are enriched, relative to bedrock. Ti and Cr are enriched in Jura and Knockfarril Hill member drill fines relative to host bedrock. Fe is enriched in fines for all samples, relative to a given host bedrock, with the enrichment less pronounced in the Glasgow samples (GG, NT, HT). Both GR fines and the nodular rich host bedrock are enriched in both P and Mn, with a near perfect correlation between these elements (r=+0.99). Ca and S are typically enriched in fines relative to bedrock for all samples.

The KM samples show the most differences to the GT bedrock. The DBA samples are enriched in Mn and P (also seen in MA and GR), up to 20-26% wt. Ca+S, and an enrichment in Zn in both DBA and tailings (also seen in AL tailings). Na and Al concentrations are similar to host bedrock for the majority of fines samples; however, the KM tailings are significantly depleted in both.

## 5. Discussion and implications

The Glen Torridon clay unit was proposed as an important MSL traverse waypoint prior to landing; it was interpreted as a lithological unit that could help inform planetary processes that influence habitability [Grotzinger et al., 2012]. The local enrichment in phyllosilicates in Glen Torridon (Fe/Mg smectites), inferred from orbital spectroscopy [e.g., Fraeman et al., 2016; Milliken et al., 2010; Fox et al., 2018; Stack et al., 2017] was of high interest, as smectites are considered to be favorable indicators of ancient habitable environments and to aid in the preservation of organic molecules [e.g., Summons et al., 2011].

Additionally, orbital mapping revealed spatial variations in the smectite signature, with highest signatures closest to VRR, decreasing to a smectite-sulfate mix with distance from VRR and into the transition to the overlying sulfate unit. The transition to a more sulfate-enriched lithology was considered to be indicative of changing environmental and depositional conditions, with broad implications for our understanding of both Gale crater [e.g., Milliken et al., 2010] and, at a more global scale, across Mars [e.g., Bibring et al., 2006].

APXS results from the exploration of Gale crater will therefore be assessed from two perspectives (1) the significance of the clay-rich material within the trough and (2) variations as *Curiosity* moved from the trough towards the clay-sulfate transition.

### 5.1. Relationship to Jura member on VRR (herein Jm_VRR)

Although orbital mapping placed the trough above VRR in terms of stratigraphy [Fraeman et al., 2016], in situ analysis shows that the Jura within Glen Torridon (Jm_GT) is stratigraphically equivalent to that on the ridge (Jm_VRR) (Section 2; Table 1) [Fedo et al., 2020, this issue]. Similarities in facies, and the absence of a clear tectonic or depositional break between the two suggest comparable depositional environments (low energy, lacustrine) [Fox et al., 2019b; Edgar et al., 2020; Caravaca et al., this issue], despite the difference in morphological expression. However, APXS identifies geochemical differences between the Jm_GT and Jm_VRR. Jm_GT exhibits lower mean Si, Al Ca, Na, P, S, Ni than mean Jm_VRR. Statistically significant variance is identified for 10 of the 16 reported elements (Table S4), a higher proportion than with any other Mf or CSf member (except Pahrump Hills, PHm). Notably, the strong correlation relationships (K, Mg, Mn, Zn) observed in Jm_GT are not identified in Jm_VRR.

Thompson et al. [2020] subdivide the Jm_VRR (on the basis of spectral signature, via orbital mapping) into *Jm_VRR_tan* (targets from areas mapped orbitally as tan coloured; the dominant lithology) and *Jm_VRR_blue* (targets from more discrete areas, mapped orbitally as blue or grey). Comparing these subunits with the Jm_GT high-K and high-Mg facies allows a more detailed analysis, identifying statistically significant variance for all elements reported on: Al, Ca, Na, S, (high-K targets: VRR_tan ± VRR_blue); Si, Mn, Ni (high-Mg targets: VRR_blue + VRR_tan); all other elements (both high-K & high-Mg facies:VRR_blue *and/or* VRR_tan) (Table 5e; Figure 7a).

AHCA and PCA were undertaken for all Jura targets to investigate compositional differences or similarities, regardless of location (Tables S5a; Figure 7b). Ideal cluster size ($K_4$) places all Jm_VRR targets in a single unit or cluster, whilst splitting Jm_GT into three clusters along (high K or high Mg) facies lines, thus confirming the homogeneity of Jm_VRR when compared to Jm_GT. Forcing $K_7$ to facilitate more detailed analysis splits targets into two groups A and B. Group A consists of Jm_GT intermediate to high Mg facies targets, plus two Jm_VRR_tan targets (from the *Rockhall* drill locale). All other targets are found in Group B, which is split into three subgroups: $B_1$ Jm_GT high-K targets only; $B_2$ dominated by Jm_VRR_blue/grey, *no* Jm_GT; $B_3$ dominated by Jm_VRR_tan, *no* Jm_GT. The key observation from this AHCA and PCA analysis is the confirmation of the unusual nature of the Jm_GT high-Mg targets (Figure 7b).

CheMin also identified mineralogical differences between Jm_GT [Thorpe et al., this issue] and JM_VRR drill targets [Rampe et al., 2020]. Jm_GT is enriched in phyllosilicates (28 wt. %) relative to Jm_VRR (5-13%). Plagioclase is half that identified in Jm_VRR (Jm_GT: 9-10%; Jm_VRR: 20-22%). Hematite in Jm_GT ranges from 1.06% to 1.71%, and magnetite was not identified. In contrast, iron oxides are enriched in Jm_VRR: hematite ranges from 2.90% to 9.30%, and magnetite is present (0.60%). Minor akageneite and jarosite are also identified on the ridge [Rampe et al., 2020].

The compositional and morphological ridge expression led previous work [e.g., Bristow et al., 2019; Fraeman et al., 2020; Frydenvang et al., 2020; Rampe et al., 2020; Turner et al., 2021] to infer the presence of a diagenetic front, along the ridge, overlain by a relatively impermeable caprock. Bristow et al. [2021] suggest silica-poor brines as a means to convert clays along the ridge into iron oxides and oxyhydroxides, with recrystallization of ferric iron oxides enhancing cementation and thus preventing erosion. APXS compositional data from Jm_VRR broadly supports this model [Thompson et al., 2020]. An assessment of the relative bedrock strength, inferred by the level of drill intensity required [Peters et al., 2018], confirm the inherent strength of Jm_VRR compared to Jm_GT [Stack et al., this issue]. Targets within Glen Torridon range from <8 MPa (targets: AL, GE1, GR) to 8.5 MPa (KM, GE2, MA1, MA3, GG, HT), in contrast to the Jm_VRR drill target (*Rockhall*, RH), which had an assessed strength of 8-12.5 MPa.

APXS data supports the theory that the Jura sediments within Glen Torridon represent the original composition of the Jura member, in contrast to the altered Jura along the ridge. In contrast to the Jm_VRR, the Jm_GT shows little evidence of alteration, with very low levels of of Ca+S, few veins or diagenetic features, which otherwise increase slowly upwards in the KHm, indicating low levels of post-depositional alteration. The compositional continuity observed by APXS from Jm_GT to the overlying Knockfarril Hill (KHm) (Section 5.2), which then grades upwards into Glasgow (Section 5.3) supports the idea that the Jm_GT is a primary composition. This interpretation is consistent with the suggestion by Rudolph et al. [this issue] that the clays in Glen Torridon were authigenic, forming in the Jura's lacustrine depositional environment. Without recrystallization of ferric iron oxides (as suggested for the VRR by Bristow et al., 2021) the softer, less resistant GT deposits were also susceptible to erosion than their altered counterparts on VRR, resulting in the current day trough expression.

597

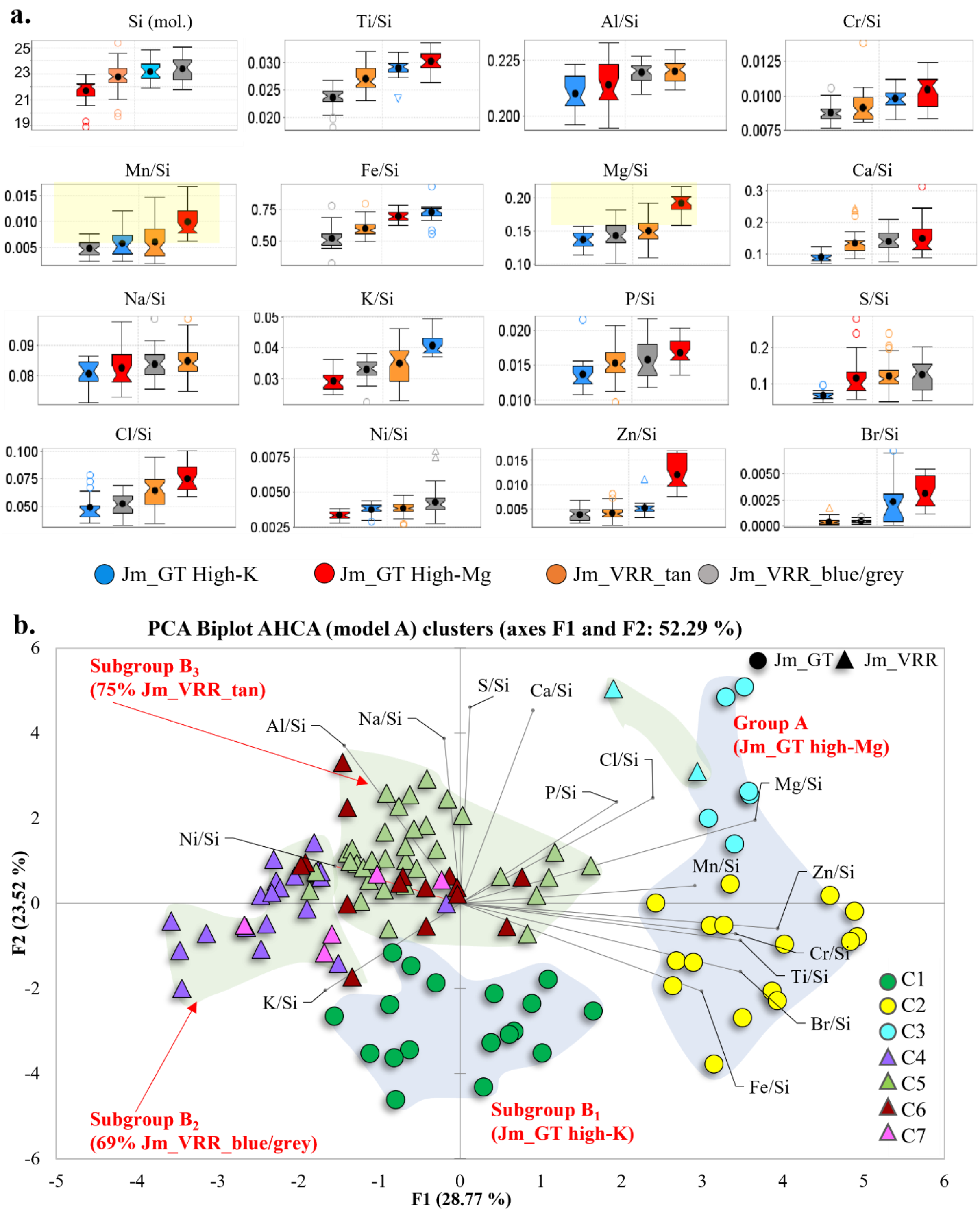


598

599
600
601

**Figure 7.** Comparison of Jura member targets, from VRR and Glen Torridon. **A.** Tukey plot comparisons of the Jm_GT (high-K and high-Mg) and Jm_VRR (tan and blue/grey) subunits (see text for details). All data in element/Si (molar) form except first plot (Si molar) (Table S1). Yellow shaded area highlights high values for Mn, Mg, K, Zn values in Jm_GT. Black circle is mean value for a given unit. Units within a given plot shown in order of increasing mean value, left to right. Tukey plot interpretation: the central box represents the mid 50% of data (Q1-Q3). Outliers (circles) are > 1.5* (Q3-Q1) from the central box; far outliers (triangles) are > 3.0 * (Q3-Q1). **B.** Multivariate PCA biplot showing compositional distinctions, both between Jm_VRR and Jm_GT, and between Jm_VRR and Jm_GT subunits (Table S5a, S5e).

### 5.2 Relationship between Jm_GT and the Knockfarril Hill member (KHm)

The main phyllosilicate trough was mapped orbitally as two distinct units based on morphology (smooth and polygonally fractured) with a smectite signal identified in both, but stronger in Jm_GT (Section 2), leading to an expectation of compositional variations between the two units. However, on the basis of APXS data, we see no evidence for substantial compositional differences between Jm_GT and KHm. In situ analysis reveals that both K-rich mudstones (dominant in Jm_GT; Section 4.1) and Mg-rich sandstones (dominant in KHm; Section 4.2) are present in both members. The interfingering of these lithologies suggests a gradual change in overall energy regimes, rather than an abrupt transition, moving from predominantly low energy lacustrine, to higher energy fluvial environment or lakeshore with fluvial input environment in KHm, but with episodic changes [Edgar et al., 2020; Caravaca et al., this issue].

APXS analysis reveals a high degree of similarity between the two members, with broad overlap for the majority of elements (Figures 4, 5) and limited statistically significant differences (Ni, P – Table S4). In contrast, both members show statistically significant variance from Jm_VRR, and with the overlying Gm (Table S4).

This result is in agreement with CheMin results from across Glen Torridon, which indicate that all three GT members (Jm_GT, KHm, Gm) are enriched in phyllosilicates (23-34 wt. %) [Thorpe et al., this issue] relative to VRR drill sites (5-13%) [Rampe et al., 2020] or GT drill sites on/in contact with the overlying pediment (6-8%) [Thorpe et al., this issue]. However, pre_VRR drill sites (*Marimba*, *Quela*, *Sebina*) also contain high levels of phyllosilicates (15-28%) [Bristow et al., 2018]. Within GT, phyllosilicate abundances are highest in GE1 (34%) and lowest in GG (23%) but concentrations are comparable (26-30%) for other targets, whether drilled in high-K facies bedrock (GE2) or high-Mg (AL, KM, MA1, MA3) facies bedrock targets. Although the CRISM signature predicted higher smectite abundances in Jm_GT, CheMin report highest phyllosilicate abundances in KHm (GE1: 34 wt.%). However, morphology constraints precluded drilling in Jm_GT high-K targets (present as rubble and pebbles), and both Jm_GT drill targets are in Mg-rich coherent bedrock, whilst the GE drill samples (KHm) were drilled in a K-rich finer grained layer, within a more coherent Mg-rich sandstone.

This suggests that the difference in spectral intensity noted by orbital mappers was driven by factors other than geochemical composition. Cofield et al. [2017] suggested that weathering out of clay minerals from one (clay-rich) unit could provide a mantle or cover on a second (clay-poor) unit, giving the illusion of smectites in both. However, given the compositional similarity between Jm_GT and KHm, as reported by both APXS and CheMin, this scenario seems unlikely.

Alternatively, Fox et al. [2019a, 2021] suggest dust cover, related to morphology, as a potential source of the differences in CRISM spectra intensity, with dust plausibly masking an equivalent absorption from KHm. The relatively larger surface area of coherent bedrock slabs (such as the sandstones that make up the KHm ridges) (Section 4.2.1) (Figures S3a-b) gather more dust than the (typically smaller) pebbles and rubble that constitute much of the Jm_GT (Section 4.1.1) (Figures S2a-d). Because the Mg content of dust [Berger et al., 2016] is higher than that of Mf bedrock, unbrushed dusty targets tend to have higher Mg concentrations than brushed rocks and drilled fines [Berger et al., 2020]. Comparing Mg concentrations in brushed and unbrushed targets can be helpful in assessing the degree to which dust is present, although caution should be taken with interpreting results, as the brushing of smaller, fragmented samples was precluded (due to risk to the brush), leading to an inherent target selection bias. For both KHm and Gm, unbrushed targets (60-65% of targets) have slightly higher mean Mg (Gm: 0.131135; KHm: 0.179379) than brushed targets (Gm: 0.16335; KHm: 0.171687). In contrast, mean Mg is higher for Jm_GT brushed targets (15% of targets) (0.184017) than unbrushed (0.163336), providing evidence that dust build up is limited on the rubbly targets. As the Jm_GT landscape is dominated by rubbly material, it follows that less dust will be present across the unit, compared to the KHm, where the phyllosilicate signal is hindered by dust buildup. This seems the most plausible explanation for the intensity differential.

**5.3 The K-Mg relationship**

Two key compositional characteristics of the lower Glen Torridon units (Jm_GT and KHm) are (1) the very well-developed anti-correlation relationship between K and Mg (Sections 4.1, 4.2; Table S3a-b; Figures 3a, 3c), and (2) the inverse relationship between K and grain size. The anti-correlation between K and Mg is not identified on VRR, in the bulk of the underlying Murray formation (Mf) or overlying Carolyn Shoemaker formation (CSf). However, it is identified in the Blunts Point member (BPm), below the ridge (BPm: K-Mg r=-0.80) (Table S3f), and within the Glasgow member subunit Gm_b (K-Mg r=-0.83) (Section 4.3.1; Table S3c).

The bimodal grain distribution within the Jm_GT and KHm has a significant correlation with the composition of each facies. Fine-grained targets are typically K-rich [defined as K/Si>mean Mf+CSf], with high Si, Fe, Ni, but low concentrations of mobile elements such as Ca, S, P, Mn, Zn. Coarse grained targets are typically Mg-rich [defined K/Si<mean Mf+CSf], with moderate to very high concentrations of Ca, S, P, Mn, Zn, Ni. The higher permeability of

the coarser grained targets, allowing more extensive post-depositional percolation of fluids, may explain the higher concentrations of mobile elements in the GT coarse grained targets. This suggests that the inverse relationship between K and grain size reflects a primary sorting process, such as the segregation of less dense, felsic [K-rich, Al-rich etc.] minerals (alkali feldspars, illites etc) from denser, mafic [Mg-rich, Fe-rich, Ni-rich etc.] minerals (e.g., pyroxene, olivine) [e.g., Fedo et al., 2015], with finer-grained less dense minerals concentrating in lower energy

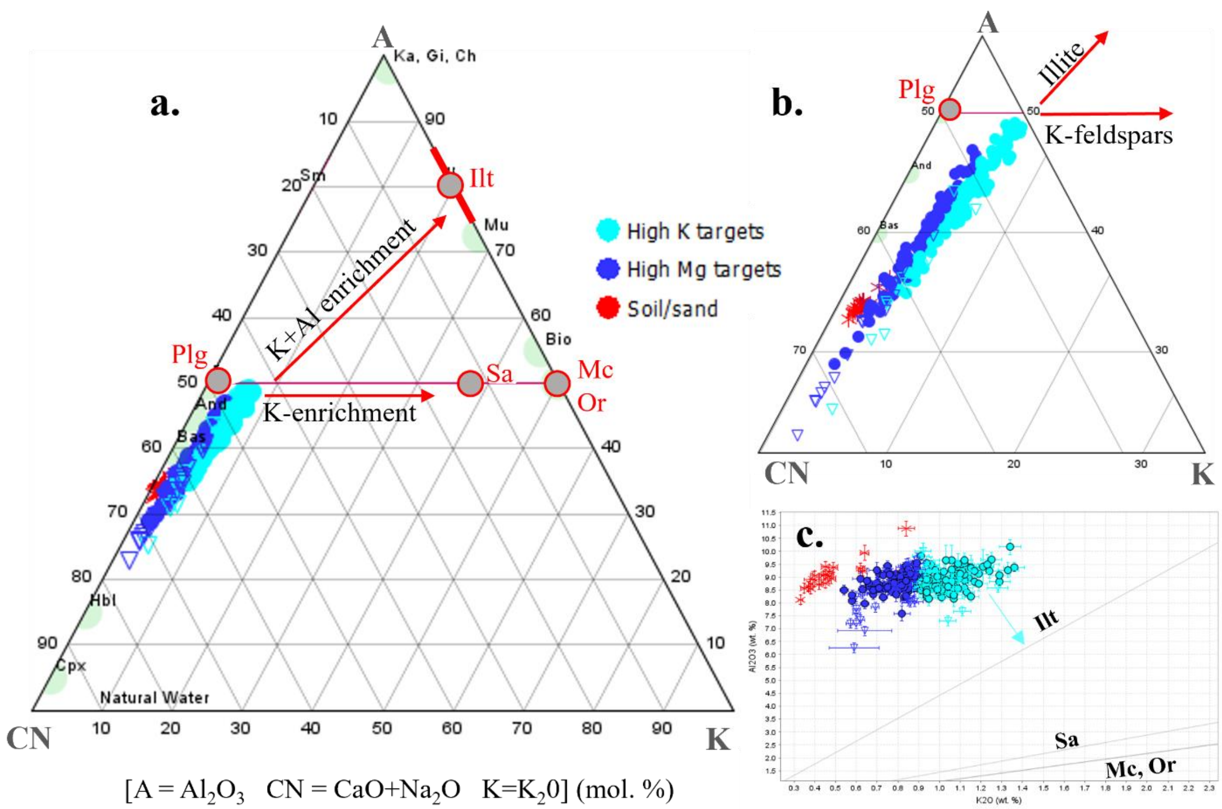


**Figure 8. 8a-b.** $Al_2O_3$-$CaO+Na_2O$-$K_2O$ (mol %) (A-CN-K) ternary diagram [Nesbitt and Young, 1984] showing Glen Torridon bedrock, drill fines, sand, plus soil samples from across Gale crater. Jm_GT, KHm and Gm bedrock targets are classified as high K [i.e., K/Si >mean Murray +Carolyn Shoemaker formations (all data molar)] or high Mg [i.e., K/Si<mean Mf+CSf (all data molar)]. Mineral abbreviations after Whitney and Evans [2010]: Plg=plagioclase; Ilt=illite; Sa=sanidine; Mc=microcline; Or=orthoclase. 8**c**. $K_2O/Al_2O_3$ ratio (wt. %) showing Glen Torridon bedrock (Jm_Gt, KHm, Gm), drill fines, sand, plus soil samples from across Gale crater. Mineral abbreviations as **A-B**.

lacustrine sediments, and coarser, denser minerals in the higher energy fluvial sediments. Compositional endmembers are less well developed within KHm than Jm_GT (30% of samples falling outside endmembers), indicating more overlap between high-K and high-Mg facies depositional settings, or a greater degree of mixing.

However, the evidence for mineral segregation is limited and not definitive. Plotting all bedrock data on a $Al_2O_3$-$CaO$+$Na_2O$-$K_2O$ (A-CN-K) ternary diagram (Figures 8a-b) [after Nesbitt and Young, 2010] to identify trends of enrichment in K-bearing mineral phases, enrichment in alkali feldspars is not identified. A tentative trend of increasing illitization is identified on the A-CN-K plot (Figures 8a-b), and on $K_2O/Al_2O_3$ ratio plots (Figure 8c). Whilst CheMin results indicate highest phyllosilicate content in the high-K facies drill targets (GE1), drill targets from all three GT members (Jm_GT, KHm, Gm) are enriched in phyllosilicates (23-34 wt. %) (Section 5.2) [Thorpe et al., this issue]. The alkali feldspar sanidine is detected in all samples but highest in the high-Mg target MA1. Pyroxene is also highest in MA1, but almost equivalent in GE2 (high-K target), whilst olivine is not detected in any sample.

### 5.4. Relationship between KHm and Glasgow member (Gm)

Although the sedimentological boundary between KHm and Gm was well defined by a change from cross stratified sandstones to finely laminated sandstones [Fedo et al., 2020, this issue], with an abrupt increase in diagenetic features at the transition, APXS did not detect a significant change in composition at the buttes (Section 4.3.1). Variance analysis for *bulk* KHm and Gm reveals some elements with statistically significant variance (Ti, Cr, Fe, Mg, Si, K) (Table S4) between the members; however, variance analysis using KHm and Gm geographically defined units finds no statistically significant variance between KHm and Gm targets at the buttes.

The majority of elements have a relatively similar profile for both KHm and Gm targets along the buttes (Figure S7). In particular, both units (plus other Gm_a targets) show a marked depletion (relative to mean Mf+CSf) in Mn and Zn. The lack of a strong geochemical change from KHm to overlying Gm in the area of the buttes could suggest a transitionary period, with a common source of material for the end of the KHm and beginning of Gm. However, compositional variations are identified within Gm, from pre-MA to post MA and additionally, moving eastward towards Mont Mercou with an increasing abundance of diagenetic features identified (Section 4.3.1; Figure S6). This suggests a change in (a) provenance with increasing elevation through Gm and/or (b) alteration processes from KHm to Gm.

## 5.5. Element mobilization and alteration

Evidence for the mobilization of Mn, Zn, P, Ca, S and Ni has been previously identified in Gale crater (pre Glen Torridon) [e.g., Thompson et al., 2020; Berger et al., 2017; Kronyak et al., 2019; Sun et al., Nachon et al., ]. APXS identifies evidence for fluid mobilization and multiple episodes of alteration across Glen Torridon. Patterns change with grain size of host rock, elevation, proximity to the capping rock, and the clay-sulfate transition zone, lying above Mont Mercou and just beyond the study area.

**5.5.1. Ca+S:** In general, $CaO+SO_3$ show a strong correlation ($r \geq +0.90$), indicating addition of $CaSO_4$ rich fluids (Table S3, Figure 5c). A trend of lower mean $CaO+SO_3$ (relative to mean Mf+CSf) in high-K targets is identified in GT bedrock (Jm_GT, KHm, Gm) (Figures 5a-c), with higher values in high-Mg targets. As high K is typically found in finer grained targets (e.g., Jm_GT mudstones), we can infer that higher $CaO+SO_3$ are found in coarser targets (e.g., KHm sandstones from Harlaw rise). This suggests that Ca+S rich fluids were utilizing the greater permeability of the coarser sandstones, resulting in higher concentrations in these targets.

Coarser Jm_GT targets are enriched in Ca+S but to a lesser extent than KHm sandstones, pointing to a trend of increasing Ca+S with elevation. Values increase with increasing elevation in the CSf to the Hutton interval, with mean values decreasing slightly in post-buttes Gm targets (Tables 2, S1; Figures 5a-b) – however, S is depleted in the Hutton interval itself.

This suggests a concentration of $CaSO_4$-rich fluids in the Glen Torridon area, potentially capped by the overlying Stimson formation, moving outwards, weakening with distance from this zone. This fits with the model proposed for the VRR [e.g., Thompson et al., 2020; Bristow et al., 2019; Frydenvang et al., 2020; Rampe et al., 2020; Turner et al., 2021] (Section 5.1), whereby an overlying relatively impermeable caprock acts as a control on diagenetic activity.

CaSO4 veins are present both parallel to bedding and cross-cutting bedding, the latter indicating later diagenetic activity (e.g., Figures S2c-d, S3a, S6a, S6d). Whilst many vein targets are primarily CaSO4, some targets also show evidence for other fluid activity e.g., the *Chassenon* vein target (sol_3069-3071), at the base of Mont Mercou, exhibits a $CaSO_4$-rich rim, but a Fe-rich core, which also showed some Na+Mn enrichment, but low Zn and Ni (Figure S6f).

Although Ca concentrations are high in the Hutton interval on Tower butte just below the unconformity, S is depleted, indicating a decoupling and an increase in Ca not related to $CaSO_4$. This is also noted at the highest elevation attained on Western butte in the bedrock target *Buchan_Haven* (sol_2640). Conversely, there is evidence for increasing S, relative to Ca, across the CSf - in KHm targets (most notably at the Groken locale, but also the ridges and in the benches area), and in Gm_b+c bedrock. A number of Gm_c nodular targets (*An_Dun*, sol_2967; *Peyrat*, sol_3051) show evidence for enriched S+Mg relative to bedrock.

**5.5.2. Na:** Na shows little change in Jm_GT or KHm, or the buttes area, with respect to elevation (or grain size), with mean values very close to mean Mf+CSf, whilst the post-buttes Gm units are depleted, relative to mean Mf+CSf (Figure 5d). Statistically significant variance is not identified for Na between Jm_GT, KHm or "typical" Gm bedrock units (Table S3a-c). However, both the Hutton interval (plus *Buchan_Haven* on Western butte) and capping rock show a significant enrichment in Na, as do a number of float rock targets (*Lomond Hills*, *Heinrich Waenke*, *Blackwaterfoot*), speculated to be related to the capping unit [e.g., Thompson et al., this issue]. Statistically significant variance for Na is identified between HT, capping rock and all other units within GT. The Groken targets also show a significant enrichment in Na. A number of Hutton samples with high Na also trend to high Cl. Slight enrichment in Na (+S±Ca) is identified in some vein (*Chassenon_raster1*, sol_3071) and nodular (*Peyrat*) Gm_c targets.

**5.5.3. Mn, P, Zn, Ni:**

Strong positive correlation relationships are present between Mg, Mn, Zn within Jm_GT and KHm (r=+0.53 to +0.86) (Sections 4.1, 4.2; 5.3**;** Table S3a-b; Figures 3a-d, 4c, 5f, 5h), with all three elements enriched (i.e., >1 standard deviation from mean Mf+CSf) in coarser grained targets, but not observed in Gm (Section 4.3; Table S3c; Figures 3e-g, 4c, 5f, 5h). Strong local enrichments in all three are identified in the Groken, Mary Anning, Aberlady and Kilmarie drill locales, and at Teal ridge and Harlaw rise (e.g., *Badcall* + *Buckie*). Within the buttes zone, higher Mg is identified in "coherent" outcrops (relatively resistant to erosion) but both Mn and Zn concentrations are typically less than mean Mf+CSf, with neither element showing signs of enrichment and lowest values in the fine-grained KHm targets on the traverse to the buttes. Zn does not increase with increasing elevation up into the pre_MA Glasgow member (Gm_a) or into the Hutton interval, with values remaining similar to those in the buttes. However, Hutton vein targets such as *Dunbartonshire* (sol_2691) and *Abernethy* (sol_2642) (Figure S5) show both highly enriched Zn and Mn. Post_MA Glasgow member (Gm_b+Gm_c) shows a trend of increasing Zn with proximity to Mont Mercou, identified in both low-K and high-K targets, suggesting a change in alteration processes. Mn is slightly enriched in Hutton interval bedrock (typically >mean but < 1 stdeva). The Mn enrichment in K-poor and depletion in K-rich targets is not identified in the Glasgow member. Post_MA Gm_b targets closest to the benches area have the highest Mn, which decreases slightly with elevation and increasing proximity to Mont Mercou.

The majority of GT bedrock targets (other than Gm_b+c) have Ni concentrations within 1 standard deviation of mean Mf+CSf, with slightly higher values in K-rich targets (e.g., Glen Etive drill locale) and lower values in the Aberlady/Kilmarie drill locale and the Hutton interval (Figure 5g). The Groken targets are depleted, as are the capping rock targets. In contrast, Gm_b+c trend to high Ni, with highest values again in K-rich targets, and a positive correlation identified between Zn-Ni (r=+0.54 to +0.63; Table S3c) not identified in any other unit.

P is depleted at lower elevations (Figure 5e) but steadily increases with elevation, with highest mean (other than GR) in the Hutton interval. As with Ca+S, P concentrations are lower in K-rich targets than Mg-rich targets for Jm_GT, KHm and Gm. sandstones. Highest P concentrations are associated with nodular Gm_c targets (*Beaupouyet*, sol_3015 (Figure S6d); *Peyrat*). Nodules in the Groken samples are significantly enriched in both Mn and P, with a near perfect correlation (r=+0.99) (Table S3c; Figs. 5e-f, S3e). This is not identified in the co-located Mn-rich MA samples, where P is below mean Mf+CSf, but is seen in Jm_GT high-Mg targets (+0.61), suggesting localized enrichment via Mn-P rich fluids. Below the VRR, strong P-Mn correlations were identified in BPm nodular targets (e.g., *Jones Marsh*, sol_1727) [Thompson et al., 2020].

## 6. Conclusion

- The Glen Torridon campaign marks the transition from the low energy lacustrine-dominated environment of the Murray formation (Jura) to the more diverse Carolyn Shoemaker formation (Knockfarril Hill and Glasgow), indicating a change in overall depositional settings. However, APXS results and statistical analysis reveals that the bulk primary geochemistry within Glen Torridon does not show a significant shift in overall composition. Targets within the Carolyn Shoemaker formation are broadly in family with those in the underlying Murray formation but do show some subtle geochemical trends with increasing elevation.
- APXS data identifies compositional differences between the Jura member within Glen Torridon (Jm_GT) and the stratigraphically equivalent Jura member on Vera Rubin ridge (Jm_VRR). The characteristic alteration on the ridge is absent from the Jm_GT, which shows instead a strong similarity to the overlying Knockfarril Hill member (KHm). Interpretation of the distinctive VRR morphology and composition, absent from the Jm_GT or overlying Knockfarril Hill member, as resulting from highly localized alteration processes is confirmed.
- Within Jm_GT and KHm, APXS data defines two geochemical endmembers (high-K or high-Mg) that correlate with a strong bimodal grain distribution (inverse relationship between grain size and K concentrations. APXS data highlights the very strong intra-facies similarity for the two members, indicating a common source and a continuation of processes (e.g., K enrichment in fine grained sediments) over time.
- The bimodal nature of the grain distribution had a strong effect on alteration patterns, with greater permeability in coarser grained targets facilitating movement of fluids,

leading to higher levels of Ca, S, P, Mn, Zn in coarser targets within Jm_GT and KHm. Ca, S, P concentrations in Jm_GT and KHm also decrease with distance from the Basal Siccar Point unconformity on the Greenheugh pediment, suggesting that the capping rock may have acted as a conduit for fluids and/or a system cap.

  - APXS identifies a transition zone from KHm to the overlying Glasgow member (Gm) in the buttes zone, with similar composition in both members in the transition zone. However, clustering and variance analysis shows that, outside of the buttes, the KHm and Gm plot discretely. APXS results suggest a zone of common alteration at the buttes and/or a gradual transition in provenance with increasing elevation in the Gm.
  - APXS results point to a complex history of alteration, with multiple episodes, including multiple generations of Ca-S rich fluids, multi-generation veins and localized enrichments or depletions of Mn, P, Zn, Ni, Na, and in Ca (relative to S) and S (relative to Ca). The anomalous Hutton interval on Tower butte provides evidence for increasing alteration with proximity to the unconformity, with abundant nodules and complex vein networks.

**Acknowledgements**: MSL APXS is managed & financed by the Canadian Space Agency (CSA). We appreciate & acknowledge the support of engineers at JPL and the MSL science team during operations. We thank F. Calef for the drill location map and drill hole images (Figure S1). Mastcam mosaics were processed by the Mastcam team at Malin Space Science Systems (NASA/JPL-Caltech/MSSS). Mars Hand Lens Imager (MAHLI) images were acquired by the MAHLI team at Malin Space Science Systems (NASA/JPL-Caltech/MSSS).
All data used in this article are listed in the references, tables, and supplements. [Data tables S1 through S7 will be hosted in a data repository. We are currently seeking a host for the data.]. All raw and reduced APXS data are available at the Planetary Data System, http://pds-geosciences.wustl.edu/missions/msl/apxs.htm.

Science team member funding for O'Connell-Cooper, Thompson, Spray, Boyd, Gellert, and McCraig is provided by the CSA. Berger was funded by a NASA Postdoctoral Program fellowship administered by USRA. VanBommel was supported by NASA/Caltech/JPL Contract 1549716 to Washington University in St. Louis for participation in the Mars Science Laboratory Science Team.

**References: Special issue references – these have been submitted or are in the process of being submitted.**

Banham, S. G., Gupta, S., Rubin, D. M., Bedford, C. C., Edgar, L., Bryk, A., Dietrich, W. E., Fedo, C. M., et al. (this issue). Evidence for seasonal- to millennial-scale wind fluctuations in an ancient aeolian dune field: Reconstruction of the Hesperian Stimson formation at the Greenheugh pediment, Gale crater, Mars. *Journal of Geophysical Research: Planets*, submitted, 2021.

Bennett, K., Fox, V., Bryk, A. B., Dietrich, W. E., Fedo, C. M., Edgar, L. A., Thorpe, M., Williams, A., et al. (this issue). An Overview of the Curiosity rover's Campaign in Glen Torridon, Gale Crater, Mars. *Journal of Geophysical Research: Planets*, submitted, 2021.

Caravaca, G., Mangold, N., Dehouck, E., Schieber, J., Zaugg, L., Bryk, A. B., Fedo, C. M., Le Mouélic, S., Le Deit, L., et al. (this issue). From lake to river: Documenting an environmental transition across the Jura/Knockfarril Hill members boundary in the Glen Torridon region of Gale crater (Mars). *Journal of Geophysical Research: Planets*, submitted, 2021

Dehouck, E., Cousin, A., Mangold, N., Frydenvang, J., Gasnault, O., Forni, O., Rapin, W., P.J. Gasda, P. J., et al. (this issue). Bedrock geochemistry and alteration history of the clay-bearing Glen Torridon region of Gale crater, Mars. *Journal of Geophysical Research: Planets*, submitted, 2021.

Fedo, C. M., Bryk, A. B., Edgar, L. A., Bennett, K. A., Fox, V. K., Banham, S. G., (this issue). Geology and Stratigraphic Correlation of the Murray and Carolyn Shoemaker formations Across the Glen Torridon Region, Gale Crater, Mars. *Journal of Geophysical Research: Planets*, submitted, 2021.

Gasda, P. J., Comellas, J., Essunfeld, A., Das, D., Bryk, A. B., Dehouck, A. B., Schwenzer, S. P., L. Crossey, Herkenhoff, K., Johnson, J.R., et al. (this issue) Overview of the morphology and chemistry of diagenetic features in the clay-rich Glen Torridon unit of Gale crater, Mars, *Journal of Geophysical Research: Planets*, submitted, 2021.

Hughes, M. N., Arvidson, R. E., Christian, J. R., Dietrich, W. E., Fedo, C. M., Lamb, M. P., & Fraeman, A. A. (this issue). Geomorphic Evolution of the Geologic Units in Glen Torridon, Gale Crater, Mars. *Journal of Geophysical Research: Planets*, submitted, 2021.

Rudolph, A., Horgan, B., Johnson, J.R., Bennett, K., Haber, J., Bell (III), J. F., Fox, V., Jacob, S., et al. (this issue). The distribution of clay minerals and their impact on diagenesis in Glen Torridon, Gale crater, Mars. *Journal of Geophysical Research: Planets*, submitted, 2021.

Stack, K. M., Dietrich, W. E., Lamb, M. P., Sullivan, R. J., Christian, J. R., O'Connell-Cooper, C. D., Sneed, J. W., Baker, M., et al. (this issue). Orbital and In-Situ Investigation of Periodic Bedrock Ridges in Glen Torridon, Gale Crater, Mars. *Journal of Geophysical Research: Planets*, submitted, 2021.

Thompson, L. M., Yen A., O'Connell-Cooper, C., Spray. J. G., Berger, J. A., Gellert, R., McCraig, M. A., VanBommel, S. J. (this issue). Widespread alteration at the base of the Siccar Point unconformity and further evidence for regional, alkaline source rock(s) at Gale crater: Exploration of the Mount Sharp group - Greenheugh pediment cap rock contact with APXS. *Journal of Geophysical Research: Planets*, submitted, 2021.

Thorpe, M. T., Bristow, T. F., Rampe, E. B., Tosca, N. J., Grotzinger, J. P., Bennett, K. A., Achilles, C. N., Blake, D. F., et al. (this issue). Mars Science Laboratory CheMin data from the Glen Torridon region and the significance of lake-groundwater interactions in interpreting mineralogy and sedimentary history. *Journal of Geophysical Research: Planets,* submitted, 2021.

Weitz, C. M., O'Connell-Cooper, C. D., Thompson, L. Sullivan, R. J., Baker, M., & Grant, J. A. (this issue). The Physical properties and geochemistry of grains on aeolian bedforms at Gale crater, Mars. *Journal of Geophysical Research: Planets,* submitted, 2021.

**References:**

Aitchison, J. (1994). Principles of compositional data analysis. *Lecture Notes-Monograph Series*, (pp. 73-81). https://doi.org/10.1214/lnms/1215463786

Anderson, R. B., & Bell, J. F., III, (2010). Geologic mapping and characterization of Gale Crater and implications for its potential as a Mars Science Laboratory landing site. *Mars* 5, 76-128, doi:10.1555/mars.2010.0004

Banham, S.G., Gupta, S., Rubin, D. M., Watkins, J. A., Sumner, D. Y., Edgett, K. S., Grotzinger, J. P., Lewis, K. W., et al. (2018). Ancient Martian aeolian processes and palaeomorphology reconstructed from the Stimson formation on the lower slope of Aeolis Mons, Gale crater, Mars. *Sedimentology*, 65(4):993-1042, doi:10.1111/sed.12469, 2018.

Banham, S. G., Gupta, S., Rubin, D. M., Bedford, C. C., Edgar, L., Bryk, A., Dietrich, W. E., Fedo, C. M., et al. (this issue). Evidence for seasonal- to millennial-scale wind fluctuations in an ancient aeolian dune field: Reconstruction of the Hesperian Stimson formation at the Greenheugh pediment, Gale crater, Mars. *Journal of Geophysical Research: Planets*, submitted, 2021.

Bennet, K. A., Bennett, K. A., Fox, V. K., Vasavada, A. R., Grotzinger, J. P., Edwards, C. S., and the MSL Science Team (2018). *The clay-bearing unit in Gale crater II: plans for the investigation of the clay-bearing unit by the Curiosity rover*. Paper presented at 49th Lunar and Planetary Science Conference, Houston, TX. LPI contribution 2083, Abstract #1277.

Bennett, K., Fox, V., Bryk, A. B., Dietrich, W. E., Fedo, C. M., Edgar, L. A., Thorpe, M., Williams, A., et al. (this issue). An Overview of the Curiosity rover's Campaign in Glen Torridon, Gale Crater, Mars. *Journal of Geophysical Research: Planets*, submitted, 2021.

Berger, J. A., Schmidt, M. E., Gellert, R., Campbell, J. L., King, P. L., Flemming, R. L., Ming, D. W., Clark, B. C., et al. (2016). A global Mars dust composition refined by the alpha-particle X-ray spectrometer in Gale crater. *Geophysical Research Letters*, 43(1), 67–75. https://doi.org/10.1002/2015GL066675

Berger, J. A., Schmidt, M. E., Gellert, R., Boyd, N. I., Desouza, E. D., Flemming, R. L., Izawa, M. R., Ming, D. W., et al. (2017). Zinc and germanium in the sedimentary rocks of Gale Crater on Mars indicate hydrothermal enrichment followed by diagenetic fractionation. *Journal of Geophysical Research:Planets*, 122(8), 1747–1772. https://doi.org/10.1002/2017JE005290

Berger, J. A., Gellert, R., Boyd, N. I., King, P. L., McCraig, M. A., O'Connell-Cooper, C. D., Schmidt, M. E., Spray, J. G., et al. (2020). Elemental composition and chemical evolution of geologic materials in Gale crater, Mars: APXS results from Bradbury Landing to the Vera Rubin ridge. *Journal of Geophysical Research: Planets*, 125, e2020JE006536. https://doi.org/10.1029/2020JE006536

Bibring, J.-P., Langevin, Y., Mustard, J. F., Poulet, F., Arvidson, R., Gendrin, A., Gondet, B., Mangold, N., et al. (2006). Global mineralogical and aqueous Mars history derived from OMEGA/Mars Express data. *Science*, 312, 400–404, doi:10.1126/science.1122659

Blake, D.F., Morris, R. V., Kocurek, G., Morrison, S. M., Downs, R. T., Bish, D., Ming, D. W., Edgett, K. S., et al. (2013). *Curiosity* at Gale Crater, Mars: Characterization and Analysis of the Rocknest Sand Shadow. *Science*, 341, doi:10.1126/science.1239505

Bristow, T. F. Rampe, E. B., Achilles, C. N., Blake, D. F., Chipera, S. J., Craig, P., Crisp, J. A., Des Marais, D. J., et al. (2018). Clay mineral diversity and abundance in sedimentary rocks of Gale crater, Mars. *Science Advances*, *4*(6), doi:10.1126/sciadv.aar3330

Bristow, T.F., Rampe, E. B., Grotzinger, J. P., Fox, V. K., Bennett, K. A., Yen, A. S., Vasavada, A. R., Vaniman, D. T., et al. (2019). *Clay Minerals of Glen Torridon, Mount Sharp, Gale crater, Mars*. Paper presented at 9th International Conference on Mars, Pasadena, CA. LPI contribution 2089, Abstract #6390.

Bristow, T. F., Grotzinger, J. P., Rampe, E. B. Cuadros, J., Chipera, S. J., Downs, G. W., Fedo, C. M., Frydenvang, J. et al. (2021). Brine-driven destruction of clay minerals in Gale crater, Mars. *Science*, 373(6551), doi: 10.1126/science.abg5449, 2021.

Bryk, A. B., Dietrich, W. E., Lamb, M. P., Grotzinger, J. P., Vasavada, A. R., Stack, K. M., Arvidson, R., Fedo, C., et al. (2019). *In Curiosity's path: The geomorphology and stratigraphy of the Greenheugh pediment and Gediz vallis ridge in Gale crater*. Paper presented at 50th Lunar and Planetary Science Conference, Houston, TX. LPI Contribution 2132, Abstract #2263.

Bryk, A.B., Dietrich, W.E., Fox, V.K., Bennett, K.A., Banham, S.G., Lamb, M.P., Grotzinger, J.P., Vasavada, A.R., et al. (2020). *The stratigraphy of Central and Western butte and the Greenheugh pediment contact.* Paper presented at 51st Lunar and Planetary Science Conference, Houston, TX. LPI Contribution 2326, Abstract #2612.

Campbell, J. L., Perrett, G. M., Gellert, R., Andrushenko, S. M., Boyd, N. L., Maxwell, J. A., King, P. L., & Schofield, C. D. M., (2012). Calibration of the Mars Science Laboratory Alpha Particle X-ray Spectrometer. *Space Science Reviews*, 170, 319-340, doi:10.1007/s11214-0129873-5

Caravaca, G., Mangold, N., Dehouck, E., Schieber, J., Zaugg, L., Bryk, A. B., Fedo, C. M., Le Mouélic, S., Le Deit, L., et al. (this issue). From lake to river: Documenting an environmental transition across the Jura/Knockfarril Hill members boundary in the Glen Torridon region of Gale crater (Mars). *Journal of Geophysical Research: Planets*, submitted, 2021

Chayes, F. (1971). *Ratio correlation: a manual for students of petrology and geochemistry*. University of Chicago Press.

Cofield, S., K. M. Stack and A. A. Fraeman (2017). *Geologic mapping and stratigraphic analysis of the "Clay trough" of Mount Sharp, Gale crater, Mars*. Paper presented at 48th Lunar and Planetary Science Conference, Houston, TX. LPI Contribution 1964, Abstract #2531.

Dehouck, E., Cousin, A., Mangold, N., Frydenvang, J., Gasnault, O., Forni, O., Rapin, W., P.J. Gasda, P. J., et al. (this issue). Bedrock geochemistry and alteration history of the clay-bearing Glen Torridon region of Gale crater, Mars. *Journal of Geophysical Research: Planets*, submitted, 2021.

Edgar, L. A. Fedo, C. M., Gupta, S., Banham, S. G., Fraeman, A. A., Grotzinger, J. P., Stack, K. M., Stein, N. T., et al. (2020). A lacustrine paleoenvironment recorded at Vera Rubin ridge, Gale crater: Overview of the sedimentology and stratigraphy observed by the Mars Science Laboratory *Curiosity* rover. *Journal of Geophysical Research: Planets*, 125(3), doi:10.1029/2019JE006307

Fedo, C. M., McGlynn, I. O., & McSween, Jr., H. Y., (2015). Grain size and hydrodynamic sorting controls on the composition of basaltic sediments: Implications for interpreting martian soils. *Earth Planetary Science Letters*, 423, 67-77, doi:10.1016/j.epsl.2015.03.052

Fedo, C. M., Grotzinger, J. P., Gupta, S., Banham, S., Bennett, K., Edgar, L., Fox, V., Fraeman, A., et al. (2019). *Evidence for persistent, water-rich, lacustrine deposition preserved in the Murray formation, Gale crater: A depositional system suitable for sustained habitability.* Paper presented at 50th Lunar and Planetary Science Conference, Houston, TX. LPI Contribution 2132, Abstract # 6308.

Fedo, C. M., Grotzinger, J. P., Bryk, A., Edgar, L. A., Bennett, K., Fox, V., Stein, N., Fraeman, A., Banham, S., Gupta, S., Edgett, K., et al., (2020). *Ground-based stratigraphic correlation of the Jura and Knockfarril Hill members of the Murray formation, Gale crater: Bridging the Vera Rubin ridge–Glen Torridon divide.* Paper presented at 51st Lunar and Planetary Science Conference, Houston, TX. LPI Contribution 2326, Abstract # 2345.

Fedo, C. M., Bryk, A. B., Edgar, L. A., Bennett, K. A., Fox, V. K., Banham, S. G., (this issue). Geology and Stratigraphic Correlation of the Murray and Carolyn Shoemaker formations Across the Glen Torridon Region, Gale Crater, Mars. *Journal of Geophysical Research: Planets*, submitted, 2021.

Fraeman, A. A., Ehlmann. B. L., Arvidson, R. E., Edwards, C. S., Grotzinger, J. P., Milliken, R. E., Quinn, D. P., & Rice M. S., (2016). The stratigraphy and evolution of lower Mount Sharp from spectral, morphological, and thermophysical orbital data sets. *Journal of Geophysical Research: Planets* 121 (9), doi:10.1002/2016JE0005095.

Fraeman, A. A., Edgar, L. A., Rampe, E. B., Thompson, L. M., Frydenvang, J., Fedo, C. M., Catalano, J. G., Dietrich, W. E., et al. (2020). Evidence for a diagenetic origin of Vera Rubin ridge, Gale crater, Mars: Summary and synthesis of *Curiosity*'s exploration campaign. *Journal of Geophysical Research: Planets*, *125*(12), doi:10.1029/2019JE006527

Frydenvang, J., Gasda, P. J., Hurowitz, J. A., Grotzinger, J. P., Wiens, R. C., Newsom, H. E., Edgett, K.S., Watkins, J., et al., (2017). Diagenetic silica enrichment and late-stage groundwater activity in Gale crater, Mars. *Geophysical Research Letters*, *44*(10), pp.4716-4724, doi:10.1002/2017GL073323

Frydenvang, J., Mangold, N., Wiens, R. C., Fraeman, A. A., Edgar, L. A., Fedo, C. M., L'Haridon, J., Bedford, C. C., et al. (2020). The chemostratigraphy of the Murray formation and role of diagenesis at Vera Rubin ridge in Gale crater, Mars, as observed by the ChemCam instrument. *Journal of Geophysical Research: Planets*, *125*, e2019JE006320. https://doi.org/10.1029/2019JE006320

Fox, V. K., Bennett, K. A., Vasavada, A. R., Stack, K. M., & Ehlmann, B. L., (2018). *The clay-bearing unit of Mount Sharp, Gale crater, I: Orbital perspective and initial results.* Paper presented at 49th Lunar and Planetary Science Conference, Houston, TX. LPI Contribution 2083, Abstract #1728.

Fox, V. K., Bennett, K. A., Bristow, T., Ehlmann, B. L., House, C., Fairén, A. G., Horgan, B., Johnson, S., et al. (2019.a). *Exploring the clay-bearing unit with the Curiosity rover.* Paper presented at 50th Lunar and Planetary Science Conference, Houston, TX. LPI contribution 2132, Abstract #2826.

Fox, V. K., Bennett, K. A., Arvidson, R. E., Ehlmann, B. L., Stack, K., Dehouck, E., Grotzinger, J. P., Bristow, T., et al. (2019.b). *Martian clay minerals from orbit to the surface: MSL and MER rover investigations of CRISM smectite detections.* Paper presented at 9th International Conference on Mars, Pasadena, CA. LPI contribution 2089, Abstract #6372.

Fox, V. K., Bennett, K. A., Bryk, A. B., Arvidson, R. E., Fedo, C. & Dehouck, E., (2021). *Contextualizing CRISM observations of the clay-bearing Glen Torridon region with the Mars Science Laboratory Curiosity rover.* Paper presented at 52nd Lunar and Planetary Science Conference, Houston, TX. LPI Contribution 2548, Abstract #2765.

Gasda, P. J., Comellas, J., Essunfeld, A., Das, D., Bryk, A. B., Dehouck, A. B., Schwenzer, S. P., L. Crossey, Herkenhoff, K., Johnson, J.R., et al. (this issue) Overview of the morphology and chemistry of diagenetic features in the clay-rich Glen Torridon unit of Gale crater, Mars, *Journal of Geophysical Research: Planets,* submitted, 2021.

Gellert, R., Rieder, R., Brückner, J., Clark, B. C., Dreibus, G., Klingelhöfer, G., Lugmair, G., Ming, D. W., et al. (2006). Alpha Particle X-ray Spectrometer (APXS): Results from Gusev crater and calibration report. *Journal of Geophysical Research: Planets*, 111, E02S05, doi:10.1029/2005JE002555

Gellert, R, B. C. Clark and the MSL and MER Science Teams, (2015). In Situ compositional measurements of rocks and soils with the Alpha Particle X-ray Spectrometer on NASA's Mars Rover. *Elements*, 11, 39-44, doi: 10.2113/gselements.11.1.39

Golombek, M., Grant, J., Kipp, D., Vasavada, A., Kirk, R., Fergason, R., Bellutta, P., F. Calef, F., et al. (2012). Selection of the Mars Science Laboratory landing site. *Space Science Reviews*, 170:41-737, doi:10.1007/s11214-012-9916-y, 2012

Grotzinger, J. P., Crisp, J., Vasavada, A. R., Anderson, R. C., Baker, C. J., Barry, R., Blake, D. F., Conrad. P., et al. (2012). Mars Science Laboratory mission and science investigation. *Space Science Reviews*, 170, 5-56, doi:10.1007/s11214-012-9892-2

Grotzinger, J. P., Sumner, D. Y., Kah, L. C., Stack, K., Gupta, S., Edgar, L., Rubin, D., Lewis, K., et al. (2014). A habitable fluvio-lacustrine environment at Yellowknife Bay, Gale Crater, Mars. *Science*, 343(6169), 1242777, doi:10.1126/science.1242777, 2014

Grotzinger, J. P., Gupta, S., Malin, M. C., Rubin, D. M., Schieber, J., Siebach, K., Sumner, D. Y., Stack, K. M., et al. (2015). Deposition, exhumation, and paleoclimate of an ancient lake deposit, Gale crater, Mars. *Science*, 350 (6257), doi:10.1126/science.aac7575

Hughes, M. N., Arvidson, R. E., Fraeman, A. A., & VanBommel, S. J. (2021). Characteristics of the Fractured Intermediate Unit from Orbital and Curiosity-Based Data. Paper presented at 52nd Lunar and Planetary Science Conference, Houston, TX. LPI Contribution 2548, Abstract #1586.

Hughes, M. N., Arvidson, R. E., Christian, J. R., Dietrich, W. E., Fedo, C. M., Lamb, M. P., & Fraeman, A. A. (this issue). Geomorphic Evolution of the Geologic Units in Glen Torridon, Gale Crater, Mars. *Journal of Geophysical Research: Planets*, submitted, 2021.

Kronyak, R. E., Kah, L. C., Edgett, K. S., VanBommel, S. J., Thompson, L. M., Wiens, R. C., Sun, V. Z., & Nachon, M., (2019). Mineral-filled fractures as indicators of multigenerational fluid flow in the Pahrump Hills member of the Murray formation, Gale crater, Mars. *Earth and Space Science*, 6(2):238-265, doi:10.1029/2018EA000482

Le Deit, L., Mangold, N., Forni, O., Cousin, A., Lasue, J., Schröder, S., Wiens, R.C., Sumner, D., et al. (2016). The potassic sedimentary rocks in Gale Crater, Mars, as seen by ChemCam on board Curiosity. *Journal of Geophysical Research: Planets*, *121*(5), 784-804. https://doi.org/10.1002/2015JE004987

Milliken, R. E., Grotzinger, J. P., & Thomson, B. J. (2010). Paleoclimate of Mars as captured by the stratigraphic record in Gale Crater. *Geophysical Research Letters*, *37*(4). doi.org/10.1029/2009GL041870

Minitti, M. E., Fey, D. M., Bennett, K. A., & Edgett, K. S., (2020). *Rock textures observed by the Mars hand Lens Imager (MAHLI) in the Glen Torridon region (Gale Crater, Mars)*. Paper presented at 51st Lunar and Planetary Science Conference, Houston, TX. LPI Contribution 2326, Abstract #2306.

Minitti, M. E., Rivera-Hernández, F., Bennett, K. A., Gupta, S., & Wiens, R.C. (2021). *Rock textures and grain sizes in the Glen Torridon region (Gale crater, Mars) observed by the Mars Hand Lens Imager (MAHLI) and ChemCam*. Paper presented at 52nd Lunar and Planetary Science Conference, Houston, TX. LPI Contribution 2548, Abstract #2435.

Mittlefehldt, D. W., Gellert, R., Ming, D. W., Yen, A. S., Clark, B. C., Morris, R. V., Schröder, C., Crumpler, L. S., et al. (2018). Diverse lithologies and alteration events on the rim of Noachian-aged Endeavour crater, Meridiani Planum, Mars: In situ compositional evidence. *Journal of Geophysical Research: Planets*, 123(5), 1255-1306. doi:10.1002/2017JE005474

Mittlefehldt, D. W., Gellert, R., VanBommel, S., Arvidson, R. E., Ashley, J. W., Clark, B. C., Crumpler, L.S., Farrand, W.H., et al. (2021). Geology and geochemistry of Noachian bedrock and alteration events, Meridiani Planum, Mars: MER Opportunity observations. *Journal of Geophysical Research: Planets*, *126*(9), e2021JE006915

Nachon, M., Mangold, N., Forni, O., Kah, L. C., Cousin, A., Wiens, R. C., et al. (2016). Chemistry of diagenetic features analyzed by ChemCam at Pahrump Hills, Gale crater, Mars. *Icarus*, *281*. doi.org/10.1016/j.icarus.2016.08.026

Nesbitt, H. W., & Young, G. M. (1989). Formation and diagenesis of weathering profiles. *The Journal of Geology*, *97*(2), 129-147. https://www.jstor.org/stable/30065535

O'Connell-Cooper, C. D., Spray, J. G., Thompson, L. M., Gellert, R., Berger, J. A., Boyd, N. I., Desouza, E. D., Perrett, G.M., et al. (2017). APXS-derived chemistry of the Bagnold dune sands: Comparisons with Gale crater soils and the global Martian average. *Journal of Geophysical Research: Planets*, *122*, 2623–2643. https://doi.org/10.1002/2017JE005268

O'Connell-Cooper, C. D. Thompson, L. M., Spray, J. G., Berger, J. A., VanBommel, S. J., Gellert, R., Boyd, N. I. & DeSouza, E. (2018). Chemical diversity of sands within the linear and barchan dunes of the Bagnold Dunes, Gale Crater, as revealed by APXS onboard Curiosity. *Geophysical Research Letters*, 45(18):9460-9470, doi:10.1029/2018GL079026, 2018

O'Connell-Cooper, C. D., Thompson, L. M., Gellert, R., Spray, J. G., Boyd, N. I., Berger, J., McCraig, M., VanBommel, S. J., & Yen, A. (2021). *APXS geochemistry of the fractured Intermediate unit (fIU) – its relationship to underlying Glen Torridon units and overlying pediment rocks at the Greenheugh unconformity.* Paper presented at 52nd Lunar and Planetary Science Conference, Houston, TX. LPI Contribution 2548, Abstract #2405.

Peters, G. H., Carey, E. M., Anderson, R. C., Abbey, W. J., Kinnett, R., Watkins, J. A., Schemel, M., Lashore, M. O., et al. (2017). Uniaxial Compressive Strengths of Rocks Drilled at Gale Crater, Mars. *Geophysical Research Letters*, 45(1), 108-116. doi: 10.1002/2017GL075965

Rampe, E. B., Bristow, T. F., Morris, R. V., Morrison, S. M., Achilles, C. N., Ming, D. W., Vaniman, D. T., Blake, D. F., et al. (2020). Mineralogy of Vera Rubin Ridge from the Mars Science Laboratory CheMin instrument. *Journal of Geophysical Research: Planets*, *125*, e2019JE006306. https://doi.org/10.1029/2019JE006306

Rice, M. S., Gupta, S., Treiman, A. H., Stack, K. M., Calef, F., Edgar, L. A., Grotzinger, J., Lanza, N., et al. (2017). Geologic overview of the Mars Science Laboratory rover mission at The Kimberley, Gale crater, Mars. *Journal of Geophysical Research: Planets*, 122(1):2-20, doi:10.1002/2016JE005200

Rivera-Hernandez, F., Sumner, D. Y., Minitti, M. E., Bennett, K. A., Bryk, A., Edgett, K. S., Yingst, R. A., Fedo, C., et al. (2020a). *Grain Size and Facies Variations in Glen Torridon (Gale Crater, Mars): Perspective from MAHLI, Mastcam, and ChemCam LIBS Data.* Paper presented at 51st Lunar and Planetary Science Conference, Houston, TX. LPI Contribution 2326, abstract #2814.

Rivera-Hernández, F., Sumner, D. Y., Mangold, N., Banham, S. G., Edgett, K. S., Fedo, C. M., Gupta, S., Gwizd, S., et al. (2020b). Grain Size Variations in the Murray Formation: Stratigraphic Evidence for Changing Depositional Environments in Gale Crater, Mars. *Journal of Geophysical Research: Planets*, 125, e2019JE006230. https://doi.org/10.1029/2019JE006230

Rudolph, A., Horgan, B., Johnson, J.R., Bennett, K., Haber, J., Bell (III), J. F., Fox, V., Jacob, S., et al. (this issue). The distribution of clay minerals and their impact on diagenesis in Glen Torridon, Gale crater, Mars. *Journal of Geophysical Research: Planets*, submitted, 2021.

Stack, K. M., Cofield, S. M., & Fraeman, A. A. (2017). *Geological map of the MSL Curiosity rover extended mission traverse of Aeolis Mons, Gale Crater, Mars.* Paper presented at 48th Lunar and Planetary Science Conference, Houston, TX. LPI Contribution 1964, Abstract #1889.

Stack, K. M., Grotzinger, J. P., Lamb, M. P., Gupta, S., Rubin, D. M., Kah, L. C., et al. (2019). Evidence for plunging river plume deposits in the Pahrump Hills member of the Murray formation, Gale crater, Mars. *Sedimentology*, *66*(5), 1768–1802. https://doi.org/10.1111/sed.12558

Stack, K. M., Dietrich, W. E., Lamb, M. P., Sullivan, R. J., Christian, J. R., O'Connell-Cooper, C. D., Sneed, J. W., Baker, M., et al. (this issue). Orbital and In-Situ Investigation of Periodic Bedrock Ridges in Glen Torridon, Gale Crater, Mars. *Journal of Geophysical Research: Planets*, submitted, 2021.

Summons, R.E., Amend, J. P., Bish, D., Buick, R., Cody, G. D., Des Marais, D. J., Dromart, G., Eigenbrode, J. L., et al. (2011). Preservation of martian organic and environmental records: Final report of the Mars biosignature working group. *Astrobiology*, 11(2): doi:10.1089/ast.2010.0506, 2011

Sun, V. Z., Stack, K. M., Kah, L. C., Thompson, L., Fischer, W., Williams, A. J., Johnson, S.S., Wiens, R.C., et al. (2019). Late-stage diagenetic concretions in the Murray formation, Gale crater, Mars. *Icarus*, *321*, doi.org/10.1016/j.icarus.2018.12.030

Thompson, L. M., Berger, J. A., Spray, J. G., Fraeman, A. A., McCraig, M. A., O'Connell-Cooper, C. D., Schmidt, M. E., VanBommel, S., et al. (2020). APXS-derived compositional characteristics of Vera Rubin Ridge and Murray formation, Gale crater, Mars: Geochemical implications for the origin of the ridge. *Journal of Geophysical Research: Planets*, 125(10), doi: 10.1029/2019JE006319

Thompson, L. M., Yen A., O'Connell-Cooper, C., Spray. J. G., Berger, J. A., Gellert, R., McCraig, M. A., VanBommel, S. J. (this issue). Widespread alteration at the base of the Siccar Point unconformity and further evidence for regional, alkaline source rock(s) at Gale crater: Exploration of the Mount Sharp group - Greenheugh pediment cap rock contact with APXS. *Journal of Geophysical Research: Planets*, submitted, 2021.

Thomson, B. J., Bridges, N. T., Milliken, R., Baldridge, A., Hook, S. J., Crowley, J. K., Marion, G. M., de Souza Filho, C. R., et al. (2011). Constraints on the origin and evolution of the layered mound in Gale Crater, Mars using Mars Reconnaissance Orbiter data. *Icarus*, *214*(2), 413-432.

Thorpe, M. T., Bristow, T. F., Rampe, E. B., Tosca, N. J., Grotzinger, J. P., Bennett, K. A., Achilles, C. N., Blake, D. F., et al. (this issue). Mars Science Laboratory CheMin data from the Glen Torridon region and the significance of lake-groundwater interactions in interpreting mineralogy and sedimentary history. *Journal of Geophysical Research: Planets*, submitted, 2021.

Turner, S. M. R., Schwenzer, S. P., Bridges, J. C., Rampe, E. B., Bedford, C. C., Achilles, C.N., McAdam, A. C., Mangold, N., et al. (2021). Early diagenesis at and below Vera Rubin ridge, Gale crater. Mars. *Meteoritics & Planetary Science*, 56(10), doi: 10.1111/maps.13748

VanBommel, S. J., Gellert, R., Berger, J. A., Campbell, J. L., Thompson, L. M., Edgett, K. S., McBride, M. J., Minitti, M. E., et al. (2016). Deconvolution of distinct lithology chemistry through oversampling with the Mars Science Laboratory Alpha Particle X-Ray Spectrometer. *X-Ray Spectrometry*, 45(3):155-161, doi:10.1002/xrs.2681

VanBommel, S. J., Gellert, R., Berger, J. A., Thompson, L. M., Edgett, K. S., McBride, M. J., Minitti, M. E., Boyd, N. I., et al. (2017). Modeling and mitigation of sample relief effects applied to chemistry measurements by the Mars Science Laboratory Alpha Particle X-ray Spectrometer. *X-Ray Spectrometry*, 46(4):229-236, doi:10.1002/xrs.2755

Weitz, C. M., O'Connell-Cooper, C. D., Thompson, L. Sullivan, R. J., Baker, M., & Grant, J. A. (this issue). The Physical properties and geochemistry of grains on aeolian bedforms at Gale crater, Mars. *Journal of Geophysical Research: Planets*, submitted, 2021.

Whitney, D. L., & Evans, B. W. (2010). Abbreviations for names of rock-forming minerals. *American mineralogist*, *95*(1), 185-187. doi: 10.2138/am.2010.3371

Williams, A. J., Eigenbrode, J., Millan, M., Williams, R. H., Buch, A., Teinturier, S., Glavin, D. P., Freissinet, C., et al. (2021). *Organic Molecules Detected with the First TMAH Wet Chemistry Experiment, Gale crater, Mars.* Paper presented at 48$^{th}$ Lunar and Planetary Science Conference, Houston, TX. LPI Contribution 2548, Abstract #1763.

Yen, A. S., Morris, R. V., Gellert, R., Berger, J. A., Sutter, B., Downs, R. T., Bristow, T., Treiman, A. H., et al., (2017). *Hydrothermal signatures at Gale crater, Mars, and possible in-situ formation of tridymite.* Paper presented at AGU Fall Meeting, New Orleans, LA. Abstracts pp. P24B-04.

Journal Geophysical Research: Planets

Supporting Information for

**Statistical analysis of APXS-derived chemistry of the clay-bearing Glen Torridon region and the Mount Sharp group, Gale crater, Mars**

Catherine Deborah O'Connell-Cooper[1], Lucy M. Thompson[1], John G. Spray[1]. Jeffrey A. Berger[2], Ralf Gellert[3], Michael McCraig[3], Scott J. VanBommel[4], Albert Yen[5]

[1]Planetary and Space Science Centre, University of New Brunswick, Fredericton, Canada

[2]NASA Johnson Space Center, Houston, TX, USA

[3]University of Guelph, Ontario, Canada

[4]Washington University, St. Louis, MO, USA

[5]Jet Propulsion Laboratory, California Institute of Technology, Pasadena, CA, USA

## Contents of this file



## Additional Supporting Information (Files uploaded separately)

Tables S1-S7 uploaded as a single Excel file:
Table S1. APXS compositional data for all targets, including location information, errors and operational statistics
Table S2. Mean values for Glen Torridon subunits and facies
Table S3. Pearson correlation coeffience (r), univariate analysis for all data.
Table S4 Variance analysis, incorporating all targets included mean Murray and Carolyn Shoemaker formations (n targets=488).
Table S5. Jura member (GT & VRR) subunits, AHCA, variance analysis results.
Table S6. Knockfarrill Hill member subunits, AHCA and variance analysis results
Table S7. Glasgow member subunits, AHCA and variance analysis results.

## Introduction

Text S1. APXS instrumentation

Text S2. Statistical analysis – derivation of mean Murray and Carolyn Shoemaker formation (mean Mf+CSf); Agglomerative Hierarchical Clustering analysis (AHCA) models.

Figure S1 includes stratigraphic column for Gale crater, Mars and a localization map of showing Glen Torridon drill target locations and Mars Hand Lens Imager (MAHLI) images

Figure S2 shows examples of morphological expression of the Jura member in Glen Torridon, (Jm_GT), Murray formation, and includes both Mastcam and Mars Hand Lens Imager (MAHLI) images.

Figure S3 shows examples of morphological expression of the Knockfarril Hill member, Carolyn Shoemaker formation and includes both Mastcam and Mars Hand Lens Imager (MAHLI) images.

Figure S4 shows examples of morphological expression of the Glasgow member, Carolyn Shoemaker formation, using Mastcam images.

Figure S5 shows examples of diagenetic features within the Hutton interval of the Glasgow member, Carolyn Shoemaker formation and includes both Mastcam and Mars Hand Lens Imager (MAHLI) images.

Figure S6 shows examples of diagenetic features in the Glasgow member, Carolyn Shoemaker formation and using Mars Hand Lens Imager (MAHLI) images.

Figure S7 shows change in concentrations, with increasing elevation, relative to mean Murray and Carolyn Shoemaker formations.

Figure S8 (a-d) summarizes the results of Agglomerative Hierarchical Clustering analysis for the Jura member within Glen Torridon, for all three models (models discussed in Supplementary Text S2b).

Figure S9 compares the Jura member within Glen Torridon (Jm_GT) to that on Vera Rubin ridge (Jm_VRR), using multivariate Principal component analysis (PCA).

Figure S10 (a-d) summarizes the results of Agglomerative Hierarchical Clustering analysis for the Knockarril Hill member, for all three models (models discussed in Supplementary Text S2b).

Figure S11 (a-d) summarizes the results of Agglomerative Hierarchical Clustering analysis for the Glasgow member, for all three models (models discussed in Supplementary Text S2b).

**Text S1.**

***The Mars Science Laboratory (MSL) Alpha particle X-ray Spectrometer (APXS):***
The MSL APXS combines particle-induced X-ray emission (PIXE) and X-ray fluorescence (XRF) to analyze rock and unconsolidated sediment targets for major elements from Z=11 to 26 (Na, Mg, Al, Si, P, S, Cl, K, Ca, Ti, Cr, Mn, Fe) and trace elements (Ni, Zn, Br, Ge, Cu, Se, As, Pb. Ga, Rb, Sr, Y, W and Pb). PIXE is efficient at exciting lower atomic numbers and XRF those with higher atomic numbers [*Gellert et al.,* 2006].
APXS consists of a main electronics unit in the rover's body and a sensor head, with six $^{224}$curium radionuclide sources concentrically surrounding a silicon drift detector, mounted on the robotic arm [*Gellert et al*., 2006]. To analyze a sample, the sensor head is placed on (in contact) or close to ("hovering") the target, for a period of time ranging from 20 minutes to eight hours. Distance from the sample increases the "field of view" (FOV) from the nominal ≈ 15 mm diameter [*Gellert et al*., 2015; *VanBommel et al*., 2016, 2017]. The sample is irradiated with alpha particles and X-ray radiation, resulting in the generation of X-rays with specific energies for each element, producing a spectrum. Observed elemental data are converted into standard oxide data using a specially developed data analysis technique ("Gellert method", originally developed for the MER APXS), by fitting summed spectra into a non-linear least squares fit routine [described in *Gellert et al*., 2006]. The fitting procedure results in peak areas of the characteristic element lines, which are first converted into element and then into oxide concentrations (using calibration tables). The oxide sum (geometric norm) is renormalized to 100% to compensate for the unknown distance of the sensor head to the sample surface, and allow for distance dependent corrections for elemental background contributions [*Gellert et al*., 2006]. The final output of the analysis consists of elemental concentrations (in weight percent), and their 2-sigma statistical error, which represent the precision of the data. Current best estimates for overall analytical accuracy, determined by comparison with a suite of geochemical reference materials: ±3 % (relative) for Si; ±7-% Al, Ca, Fe; ±7 % Mn; ±11 % Na; ±14 % Mg; ±15 % P, S, K; ±16 % for Ni, Zn; ±19 % Cr; ±11 %; ±20 % Ti, Br; ±30 % for Cl [*Gellert et al*., 2006]. Instrument performance is monitored by periodically calibrating to an on-board basaltic calibration slab ("BT-2") [*Campbell et al*., 2012; *Thompson et al*., 2012, 2013].

**Text S2.**

## S2a. Arithmetic mean Murray and Carolyn Shoemaker formation

The arithmetic mean for Murray and Carolyn Shoemaker formation (**mean Mf=CSf**) (Tables 2a, S1) was compiled from 488 representative bedrock and drill fines targets, across the nine members included at time of writing:
Glasgow mbr (Gm), Carolyn Shoemaker fm [Fedo et al., this issue]
Knockfarril Hill mbr (KHm), Carolyn Shoemaker fm [Fedo et al., this issue, 2020]
Jura member (Jm), Murray fm [Edgar et al., 2020]
Pettegrove Point member (PPm), Murray fm [Edgar et al., 2020]
Blunts Point member (BPm), Murray fm [Fedo et al., 2019]
Sutton Island member (SIm), Murray fm [Fedo et al., 2019]
Karasburg member (KBm), Murray fm [Fedo et al., 2019]
Hartmanns's Valley member (HVm), Murray fm [Fedo et al., 2019]
Pahrump Hills member (PHm), Murray fm [Fedo et al., 2019]

Column D, Table S1, indicates targets included in the mean. Targets were identified as outliers using standard (Z) scores to identify targets outside of the 95% confidence interval (±1.96 Standard Error). These samples were then investigated individually, via Mars Hand Lens Imager (MAHLI) images etc. Targets excluded: rubble-sand mixed regolithic targets in Glen Torridon, which often have a degree of sand or soil contributing to the target composition; obvious vein targets; targets with combined $CaO+SO_4$ > 20 wt. %; targets with high $SiO_2$ (> 65 wt. %, typically associated with zones of alteration at Marias Pass [Yen et al., 2017; Frydenvang et al. 2017]; all Hutton interval targets; diagenetic features such as concretions and nodules, including those with MnO >0.75 wt% and $P_2O_5$ >1.95 wt.%; targets with FWHM ≥200 eV.

## S2b. Agglomerative Hierarchical Clustering analysis (AHCA):

AHCA was run to investigate similarities within members (Jm_GT, Section 4.1.2; KHm, Section 4.2.2; Gm Section 4.3.2; Jm_GT and Jm_VRR, Section 5.1). The Euclidean distance metric was used for all models and Ward's minimum variance method was used to define cluster linkages as it defines with clusters with low internal dissimilarity. All data was in the form of $Log_{10}$[element/Si] mole ratios, to minimize closure issues, associated with normalizing APXS data to 100% [Gellert et al., 2006; Chayes, 1971; Aitchison, 1994]. Targets excluded obvious diagenetic features, sand, soil and regolithic measurements from across Glen Torridon, whose compositions may have included contributions from unconsolidated materials. Drill fines were initially included but plotted distinctly for the majority of models and excluded in later runs. The ideal cluster size (K) was determined through the sum of squares method ("elbow method").

For each data set, three model parameters were run. Model A includes all elements routinely reported on by APXS. Following Mittlefehldt et al. [2018, 2021], Model B excludes the volatile elements S, Cl, Br, to minimize the effect of such variable elements on the bedock clustering. Model C excludes S, Cl, Br and the mobile elements Mn, P, Zn, Ni to examine the extent of alteration [e.g., Mittlefehldt et al. 2018, 2021].

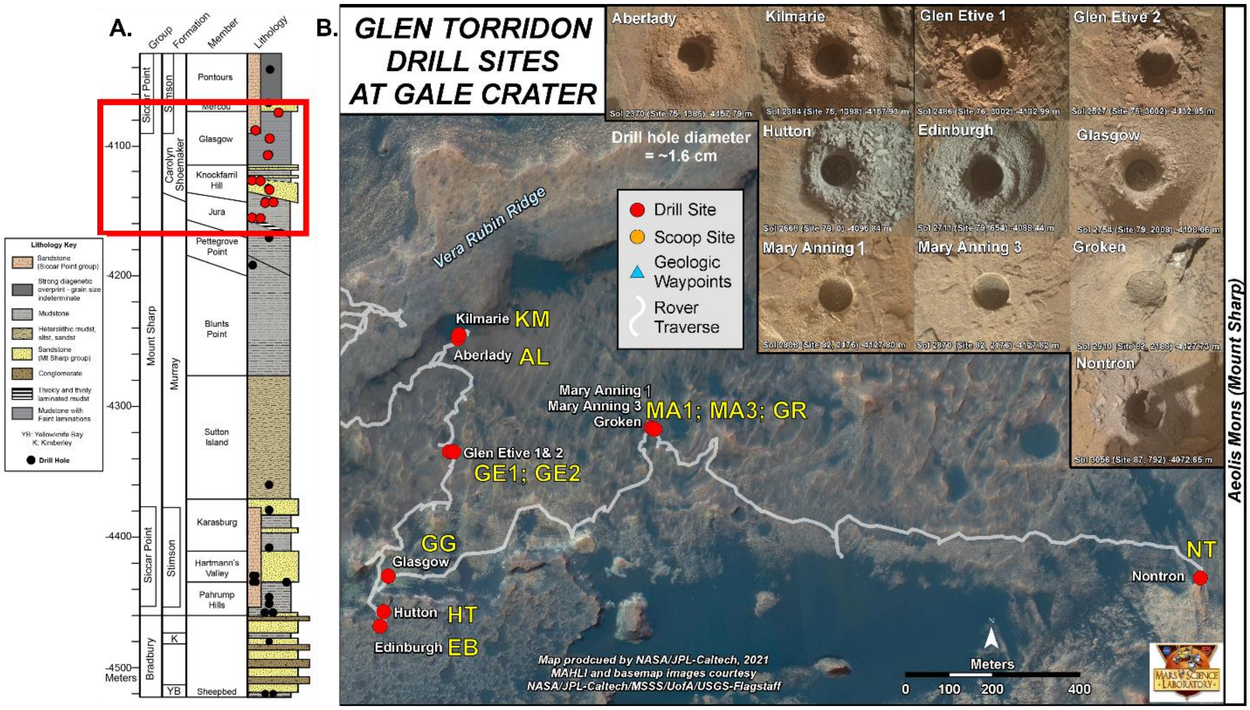


**Figure S1.** Map of Glen Torridon, Gale crater, Mars, showing drill target locations and images. **S1A.** Stratigraphic column [after *Fedo et al., this issue*], with study area highlighted in red. S1B. Localization map, showing drill target locations marked by red circles and official acronyms. Date of drill target acquisition is shown on insert images. Image S1B Courtesy of F. Calef III, and NASA/JPL-Caltech/MSSS/UofA/USGS-Flagstaff.

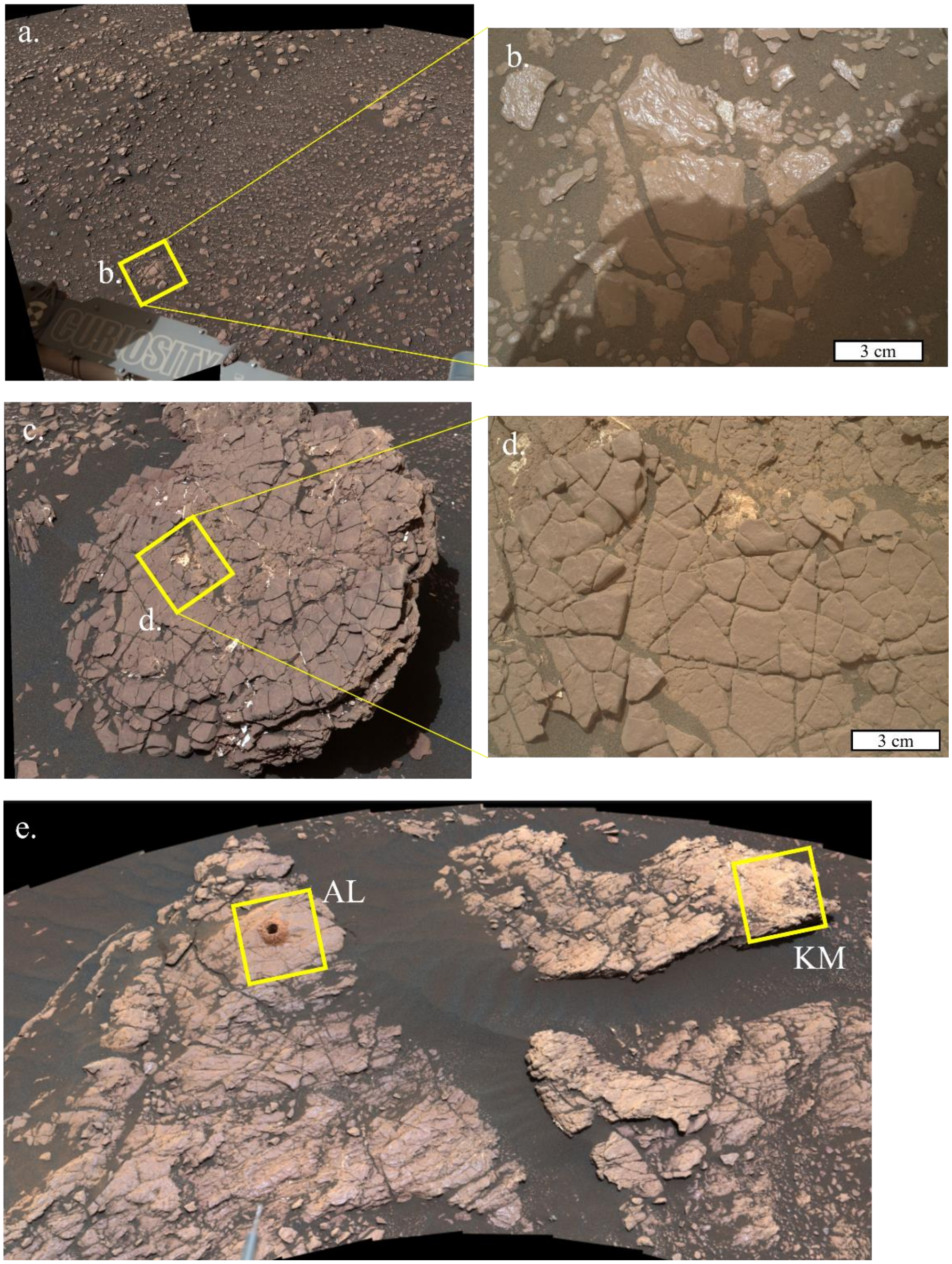


**Figure S2. The Jura member in Glen Torridon, (Jm_GT), Murray (section 4.1.1).** APXS target names are in italics, followed by sol of acquisition and Mastcam or Mars Hand Lens Imager (MAHLI) identifiers in brackets. Mastcam mosaic and MAHLI images: NASA/JPL-Caltech/MSSS. **S2a**. Typical regolithic, rubbly Jm_GT (Mastcam sequence 012509, sol 2361). **S2b**. *Ardmillan*, sol 2361 (2361MH0007060010804640C00). **S2c**. Muir of Ord boulder (Mastcam sequence 12474, sol 2352). **S2d**. *Crieff*, sol 2352 (2352MH0007060020804421C00). **S2e**. *Kilmarie* (KM) and *Aberlady* (AL) drill locale, coherent sandstone bedrock (Mastcam sequence 012571, sol 2371)..

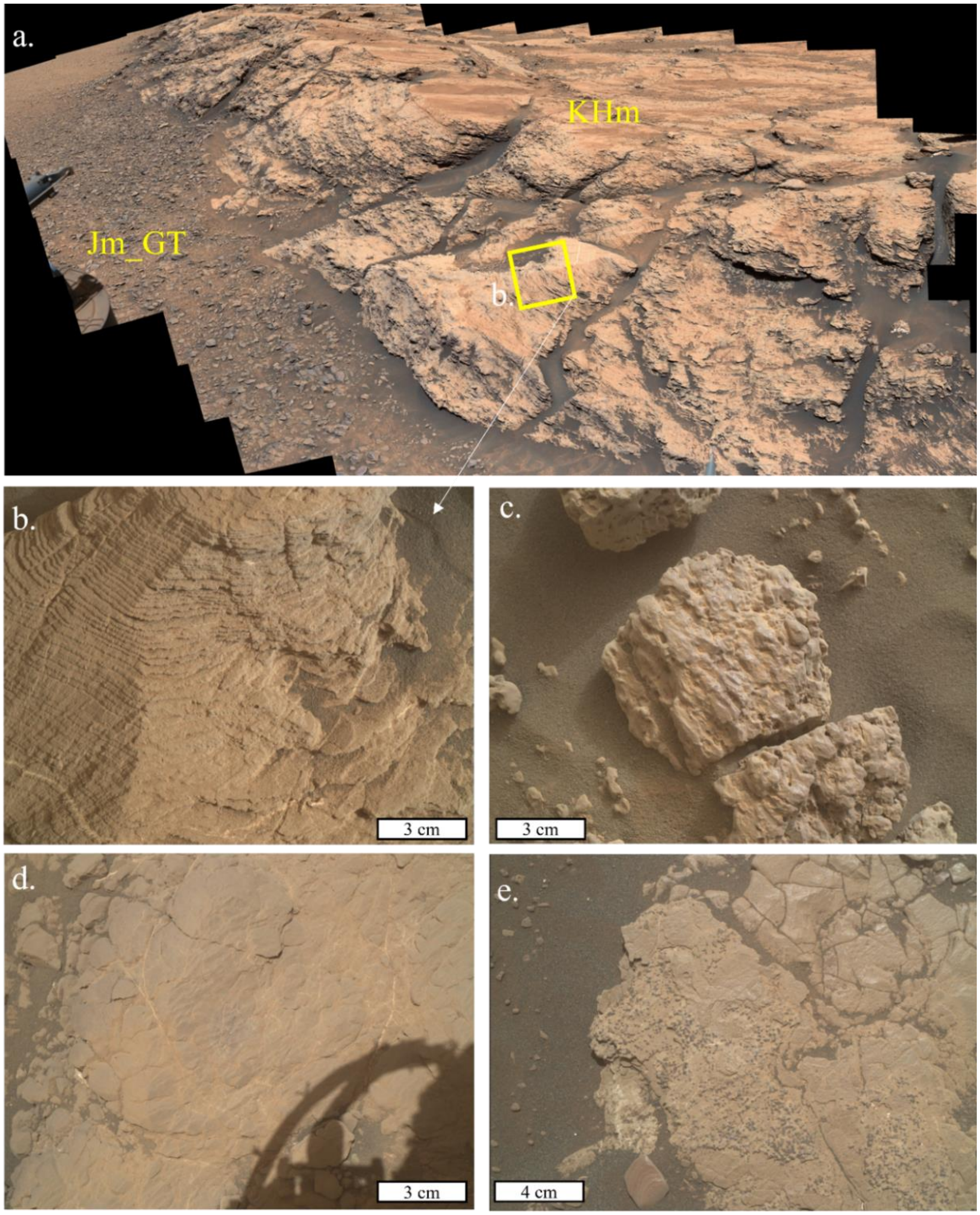


**Figure S3. The Knockfarril Hill member, Carolyn Shoemaker formation (Section 4.2.1).** APXS target names are in italics, followed by sol of acquisition and Mastcam or Mars Hand Lens Imager (MAHLI) identifiers in brackets. Mastcam mosaic and MAHLI images: NASA/JPL-Caltech/MSSS. **S3a**. Teal ridge, showing KHm sandstones overlying regolithic Jm_GT (Mastcam sequence 013416, sol 2553). **S3b**. *Balnakettle*, sol 2443 (2443MH0007060020901544C00). **S3c**. *Shetland*, sol 2564 (2564MH0001900010903636CO). **S3d**. *Nedd*, sol 2590 (MH0007060010904574C00). **S3e.** *Groken*, sol 2906 (2906MH0004240011003483C00).

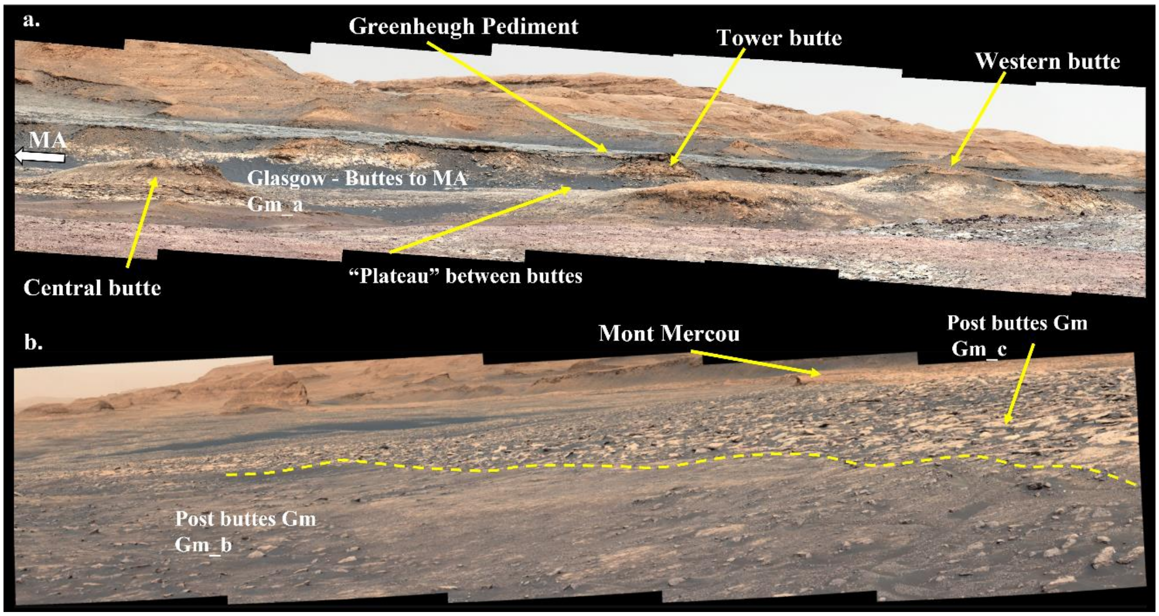


**Figure S4.** The Glasgow member, Carolyn Shoemaker formation (Section 4.3.1). Mastacam image identifiers are in brackets, with sol of acquisition. Mastcam mosaics: NASA/JPL-Caltech/MSSS. **S4a**. Mastcam mosaic (Mastcam sequence 013985, sol 2019) of the approach to Central, Western and Tower buttes, comprised of the main Glasgow member (Gm_a). The Hutton interval and drill locale is at the top of Tower butte, in contact with the overlying Greenheugh pediment. The Mary Anning drill locale is to the left of the buttes complex **S4b.** Approach to Mont Mercou, across the Glasgow member subunits Gm_b and Gm_c (Mastcam sequence 015740, sol 3018).

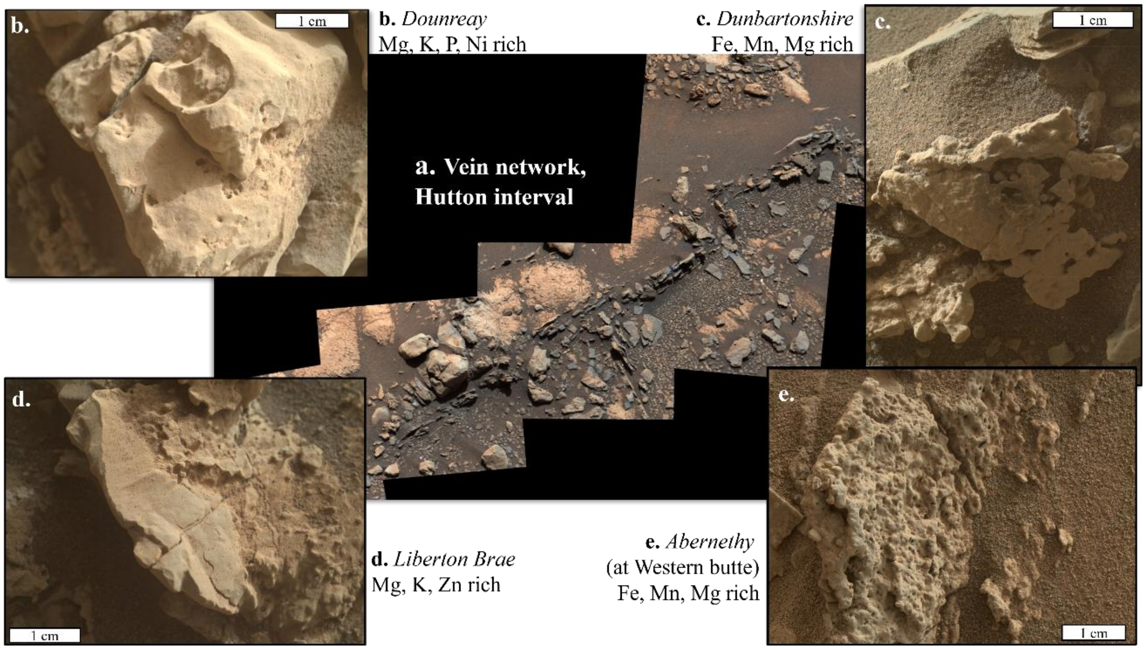


**Figure S5.** Examples of diagenetic features within the Hutton interval, Glasgow member, Carolyn Shoemaker formation. APXS target names are in italics, followed by sol of acquisition and Mastcam or Mars Hand Lens Imager (MAHLI) identifiers in brackets. Mastcam mosaic and MAHLI images: NASA/JPL-Caltech/MSSS. **S5a**. Mastcam mosaic of a complex vein network within the Hutton interval, on Tower butte (Mastcam sequence 013985, sol 2666). **S5b-S5e**: All MAHLI images are from Tower butte, except S5e from Western butte. **S5b**. Dounreay, sol 2690 (2690MH0003060011001889C00). **S5c**. *Dunbartonshire*, sol 2690 (2690MH0001930001001912R00). **S5d**. *Liberton Brae*, sol 2666 (2666MH0002970011001579C00). **S5e**. *Abernethy*, sol 2642 (2643MH0004580001001002R00).

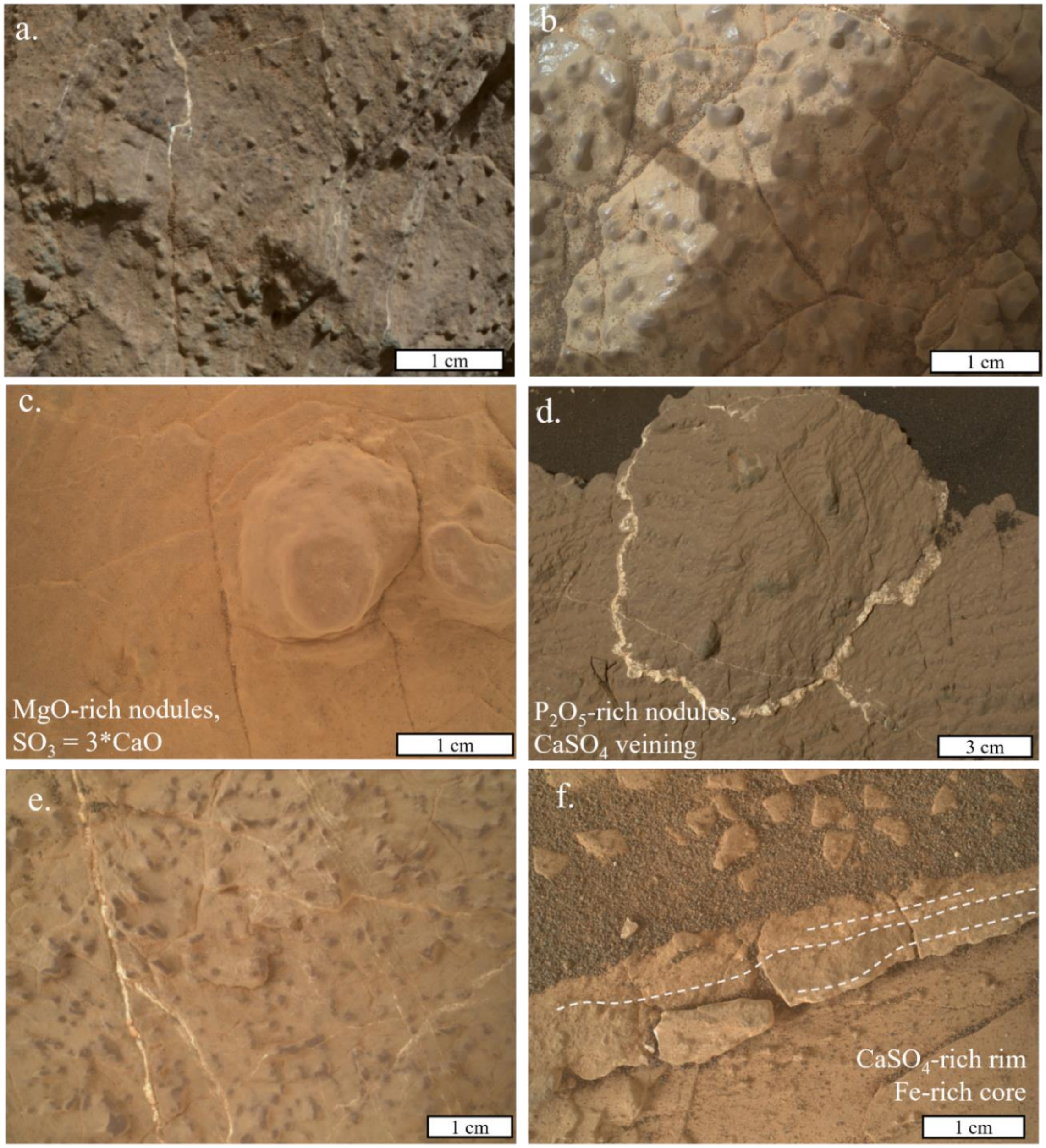


**Figure S6. Examples of diagenetic features within the Glasgow member, Carolyn Shoemaker formation (Sections 4.3.1, 5.5).** APXS target names are in italics, followed by sol of acquisition and or Mars Hand Lens Imager (MAHLI) identifiers in brackets. MAHLI images: NASA/JPL-Caltech/MSSS. **S6A**. *Sourhope*, sol 2583 (2583MH0001930000904258R00). **S6b**. *Achnasheen*, sol 2965 (2965MH0001820011004418C00). **S6c**. *An Dun*, sol 2974 (2974MH0001700000904677R00). **S6d**. *Beaupouyet*, sol 3015 (3015MH0007060011100271C00). **S6e**. *Limeyrat*, sol 3034 (3034MH0006990011100677C00). **S6f**. *Chassenon*, sol 3069 (3069MH0007630011101184C00).

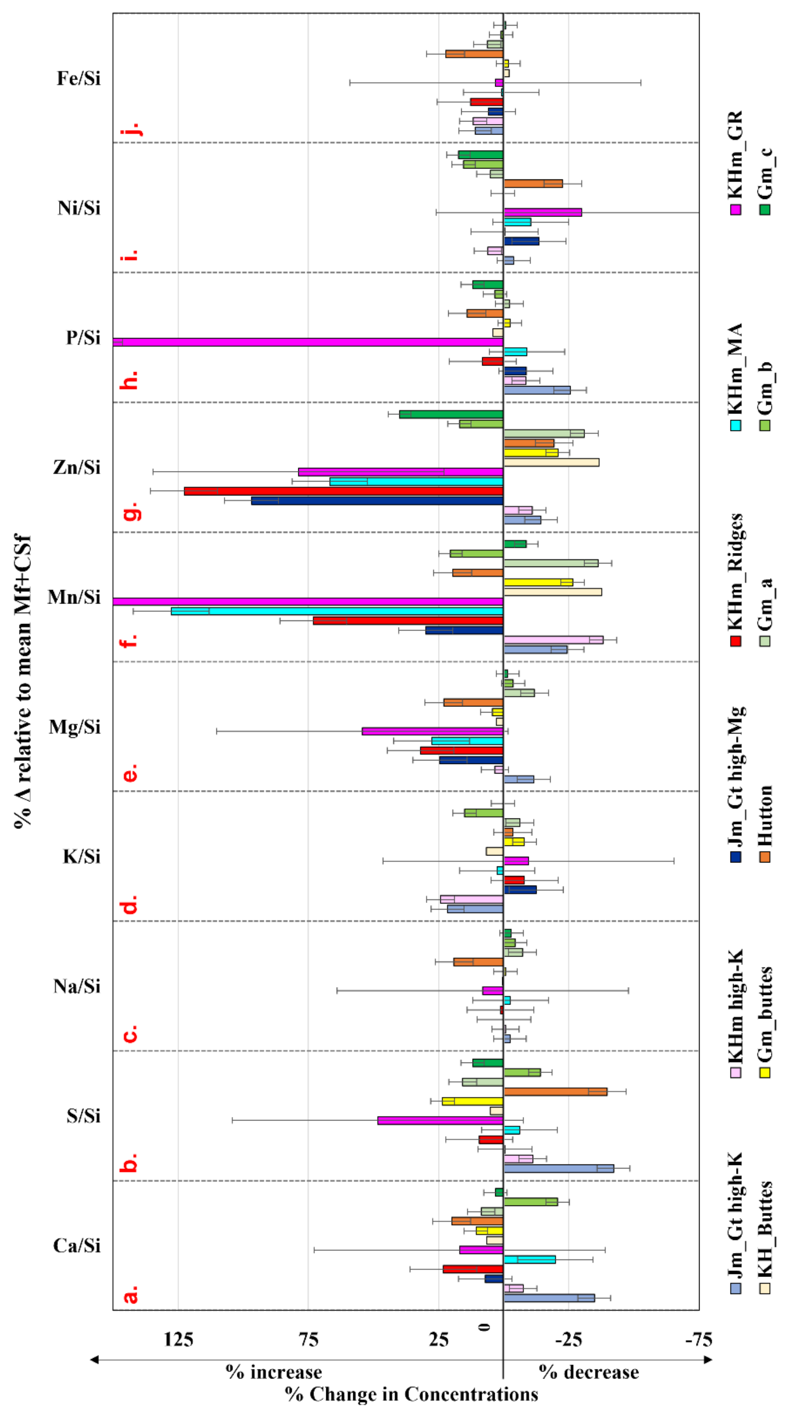


**Figure S7.** Changes in concentration, with increasing elevation, depicted as % change relative to mean Murray and Carolyn Shoemaker formations (Mf+CSf). All data in X/Si (molar) form. Each unit is shown in campaign order, except KHm_MA (shown next to other KHm units, and comparable elevations). KHm high-K unit = South Visionarium and traverse targets.  KHm_Buttes and Gm_Buttes = targets from sols 2570 to 2653.

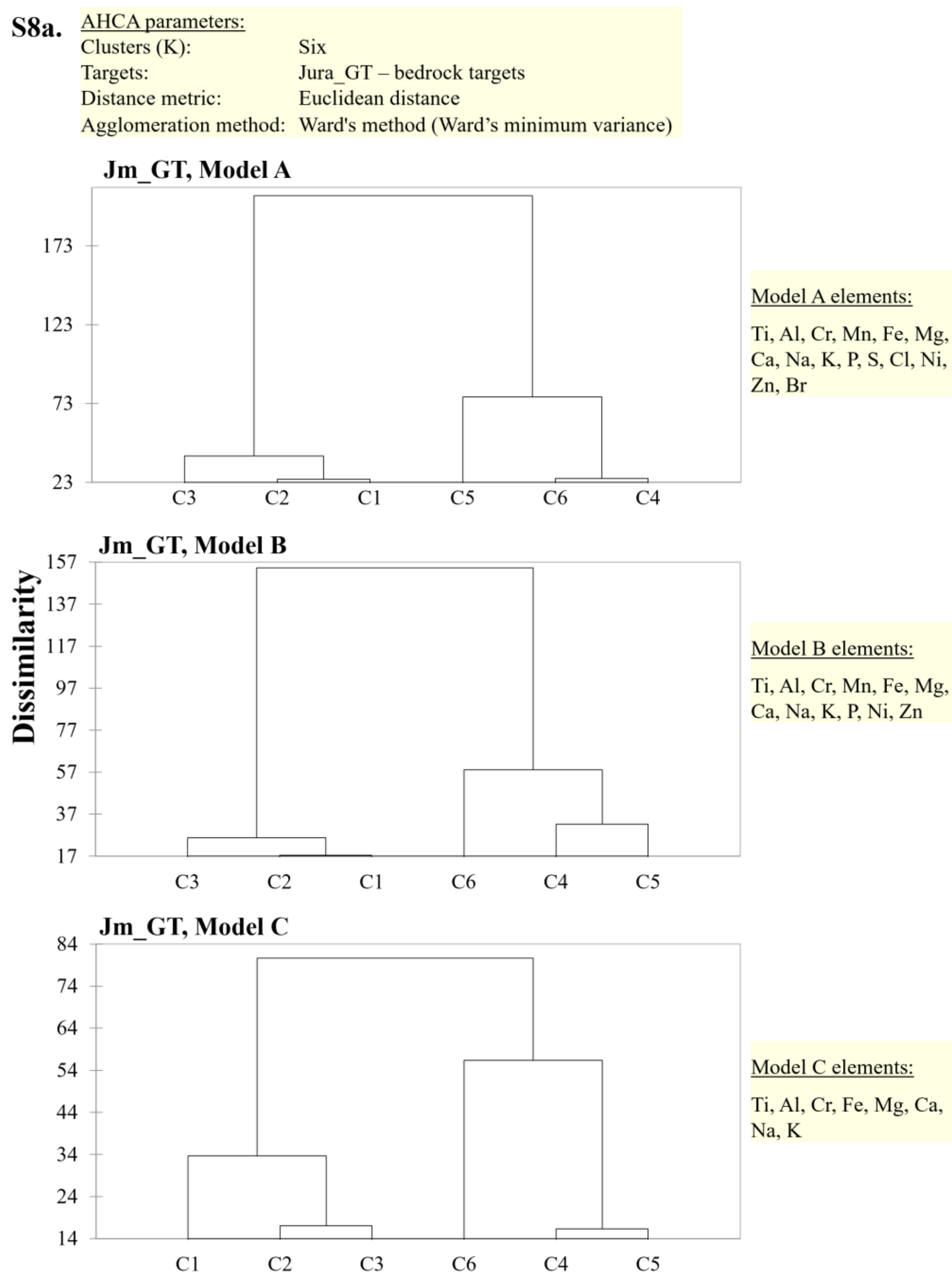


**Figure S8. Agglomerative Hierarchical Clustering analysis (AHCA) dendrograms for Jura member (Glen Torridon) (n targets = 40).** All models were run using Log10 (element/Si) (mole ratios). Model parameters are discussed in Section 3.3 and Supplementary Text S2b; results are listed in Table S5a and discussed in Section 4.1.2. **S8a.** Comparison of dendrograms for Models A-C, with detailed views for each model (with target names in figures **S8b-S8d**.

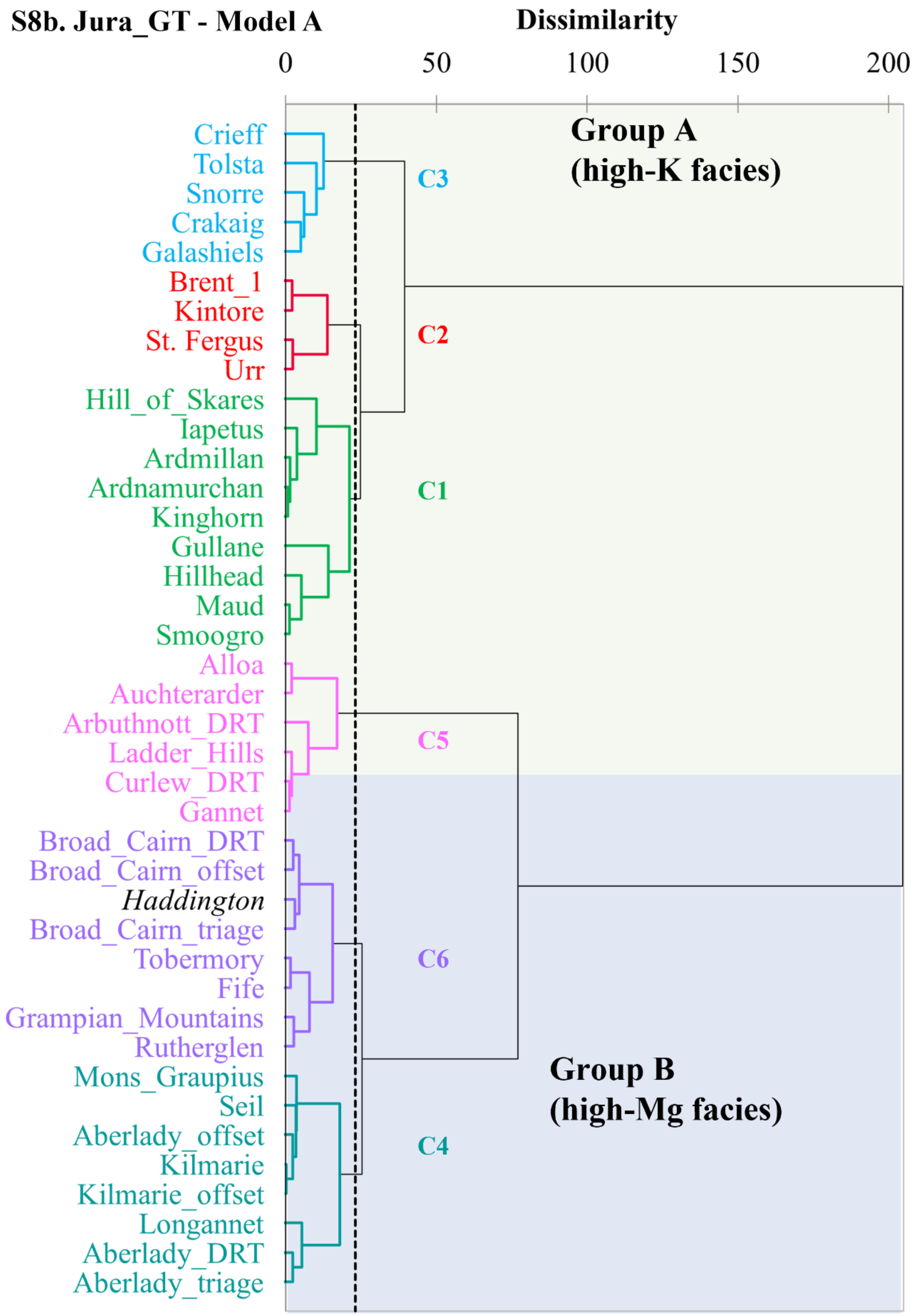
S8b. Jura_GT - Model A
Dissimilarity
0
50
100
150
200
Group A
(high-K facies)
Group B
(high-Mg facies)
C3
C2
C1
C5
C6
C4
Crieff
Tolsta
Snorre
Crakaig
Galashiels
Brent_1
Kintore
St. Fergus
Urr
Hill_of_Skares
Iapetus
Ardmillan
Ardnamurchan
Kinghorn
Gullane
Hillhead
Maud
Smoogro
Alloa
Auchterarder
Arbuthnott_DRT
Ladder_Hills
Curlew_DRT
Gannet
Broad_Cairn_DRT
Broad_Cairn_offset
Haddington
Broad_Cairn_triage
Tobermory
Fife
Grampian_Mountains
Rutherglen
Mons_Graupius
Seil
Aberlady_offset
Kilmarie
Kilmarie_offset
Longannet
Aberlady_DRT
Aberlady_triage

**S8c. Jura_GT - Model B**

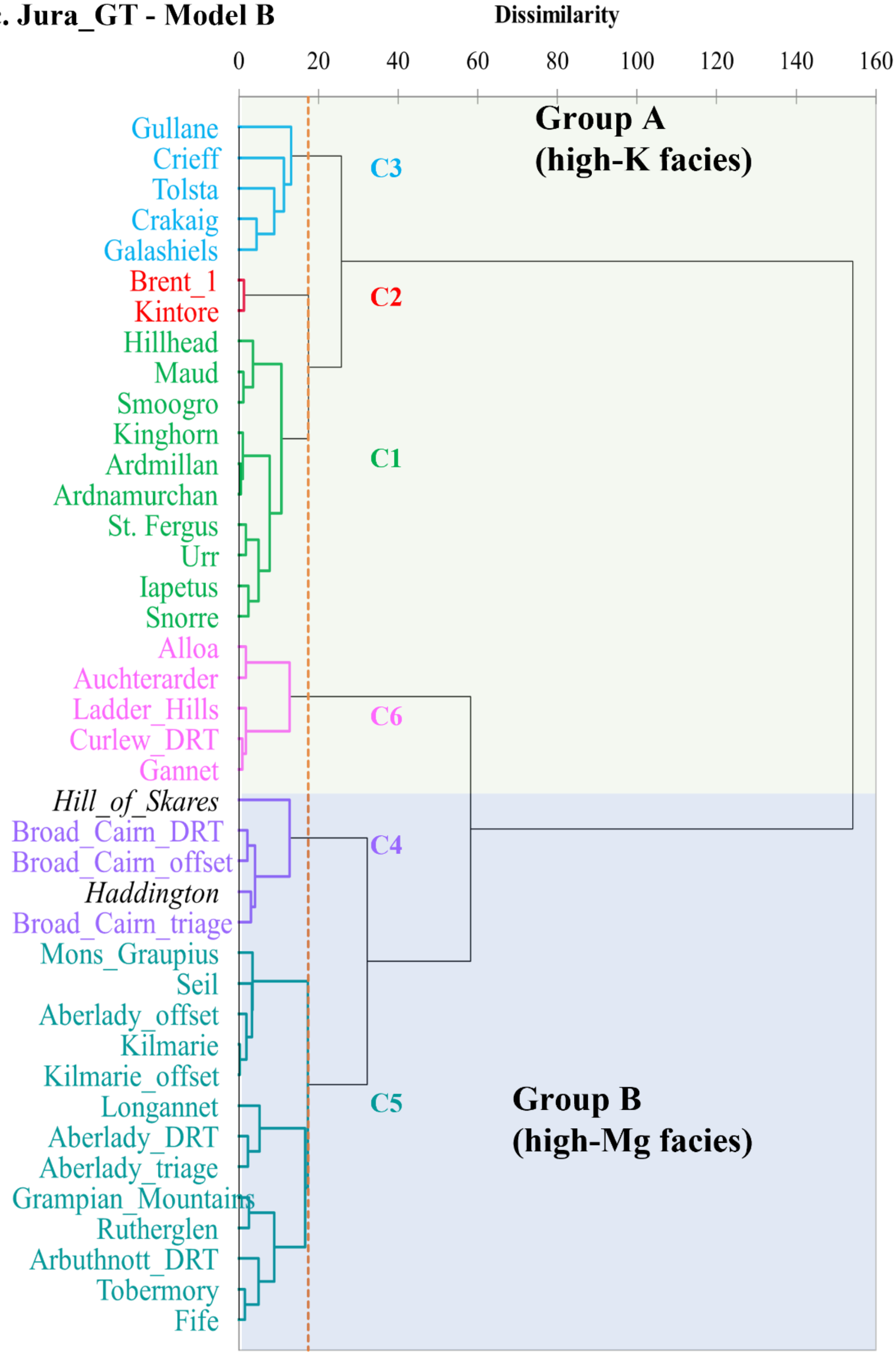

**S8d. Jm_GT – Model C**

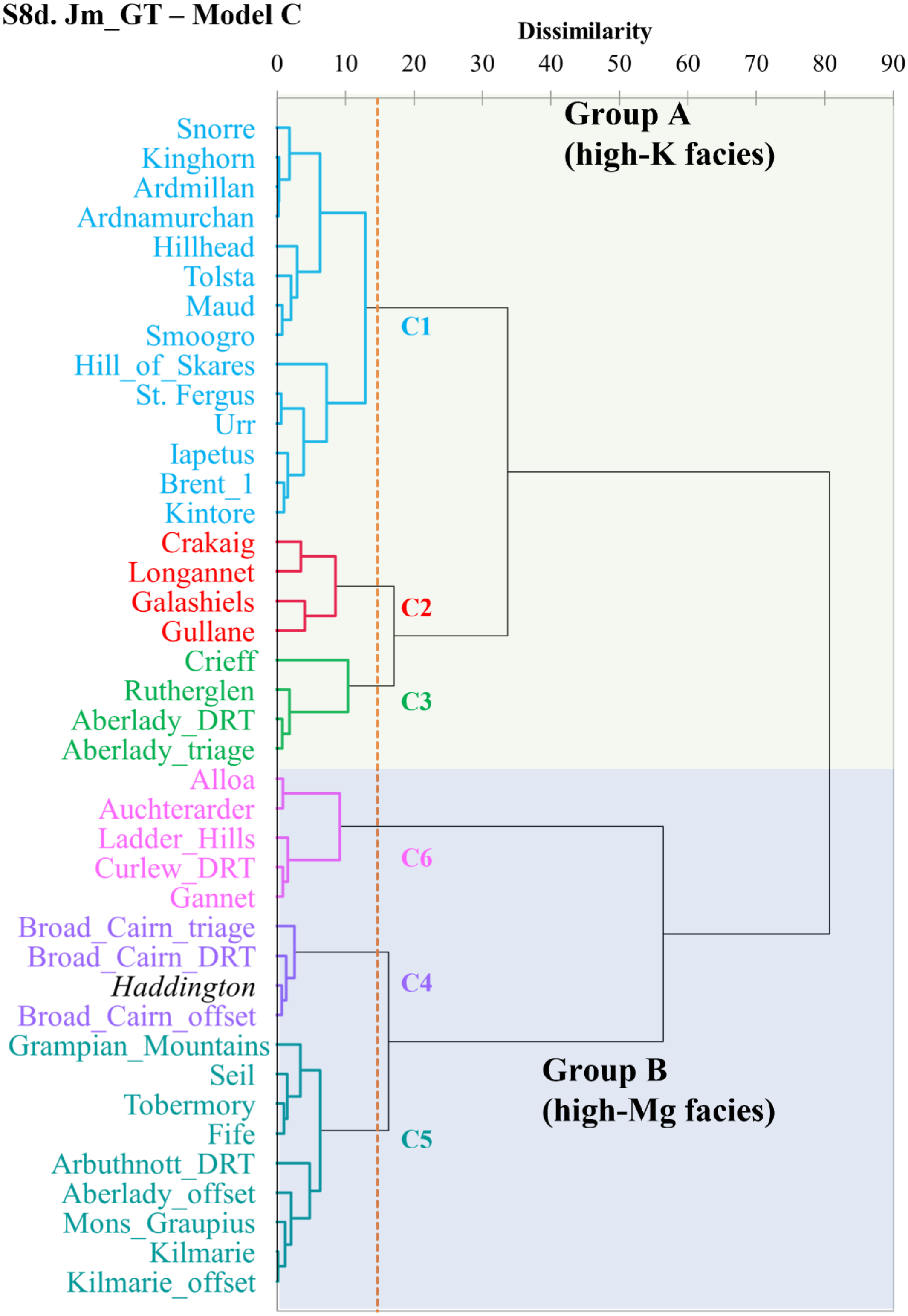

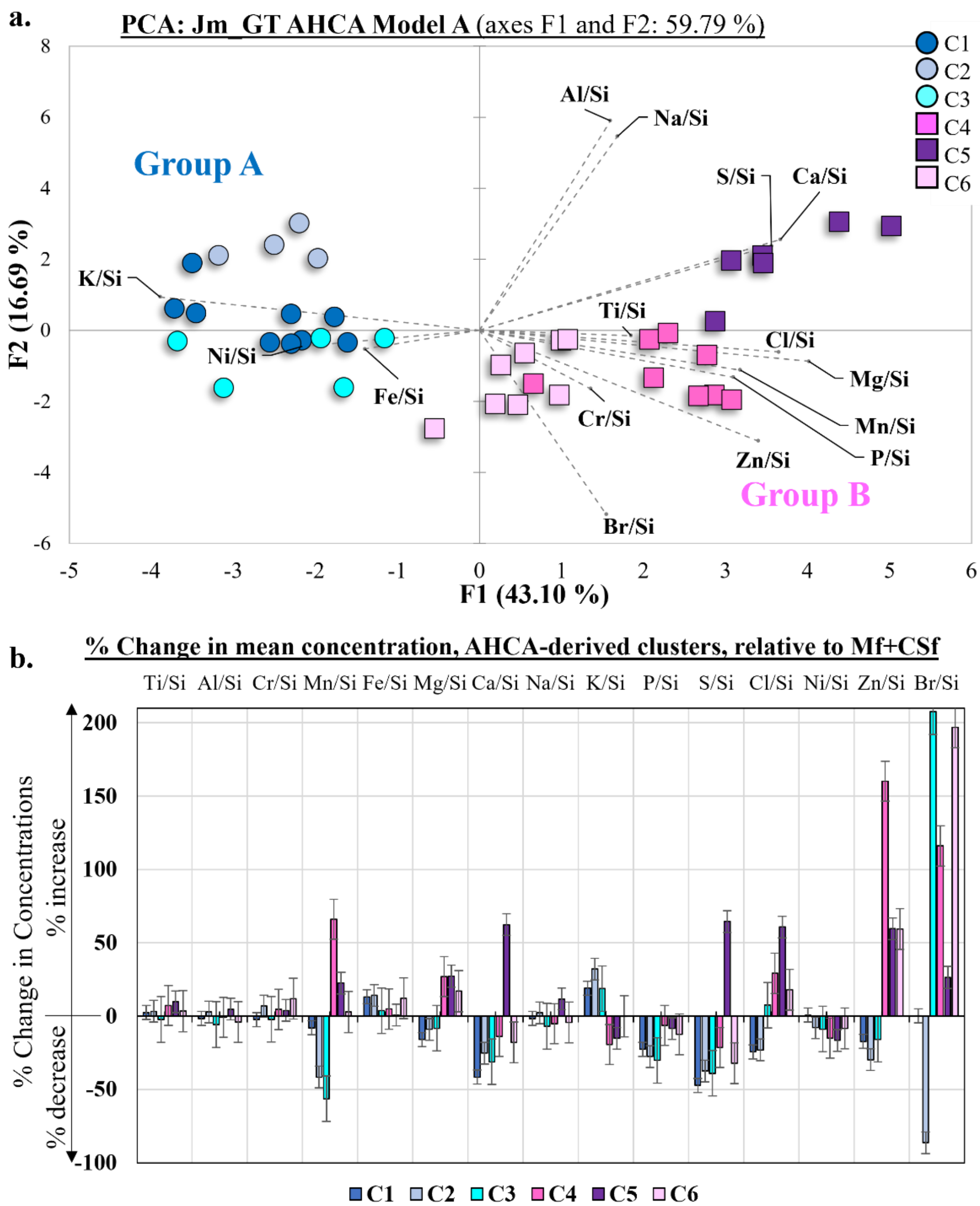


**Figure S9. S9a.** Multivariate Principal component analysis (PCA) of the Jura member, Glen Torridon (Jm_GT), using AHCA derived clusters (Model A parameters, K=6) using Log10 (element/Si) (mole/ratios) (Table S5a; Section 4.1.2). **S9b.** Percentage change in mean concentrations for Model A clusters (Table S5a), relative to mean Murray and Carolyn Shoemaker formations (Mf+CSf) (Table S1), calculated using mean element/Si (mole/ratios) for each cluster.

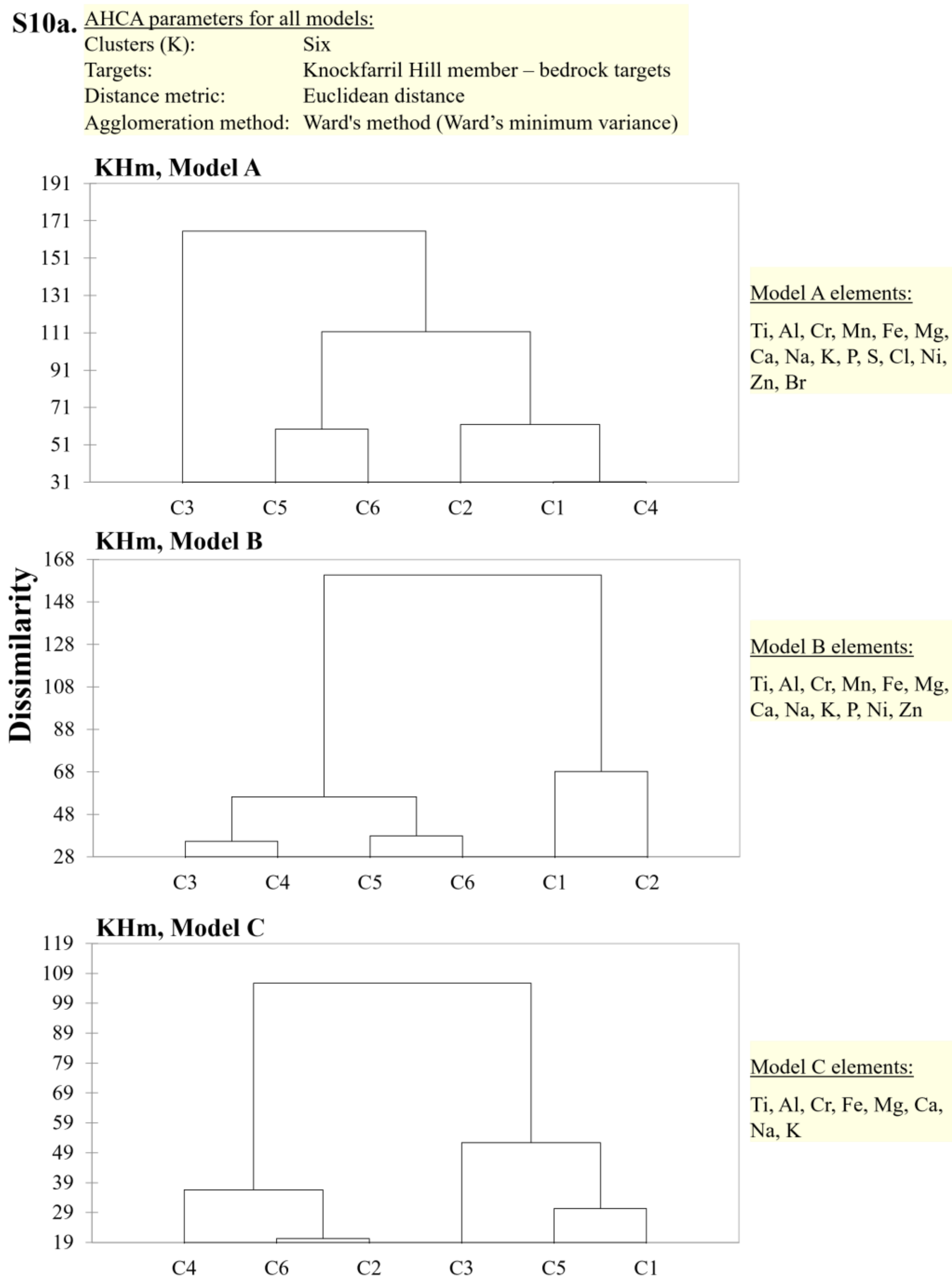


**Figure S10. Agglomerative Hierarchical Clustering analysis (AHCA) dendrograms for the Knockfarril Hill member (Glen Torridon) (n targets = 55).** All models were run using Log10 (element/Si) (mole ratios). Model parameters are discussed in Section 3.3 and Supplementary Text S2b; results are listed in Table S6a and discussed in Section 4.2.2. **S10a.** Comparison of dendrograms for Models A-C, with detailed views for each model (with target names in figures **S10b-S10d**.

**S10b. KHm – Model A**

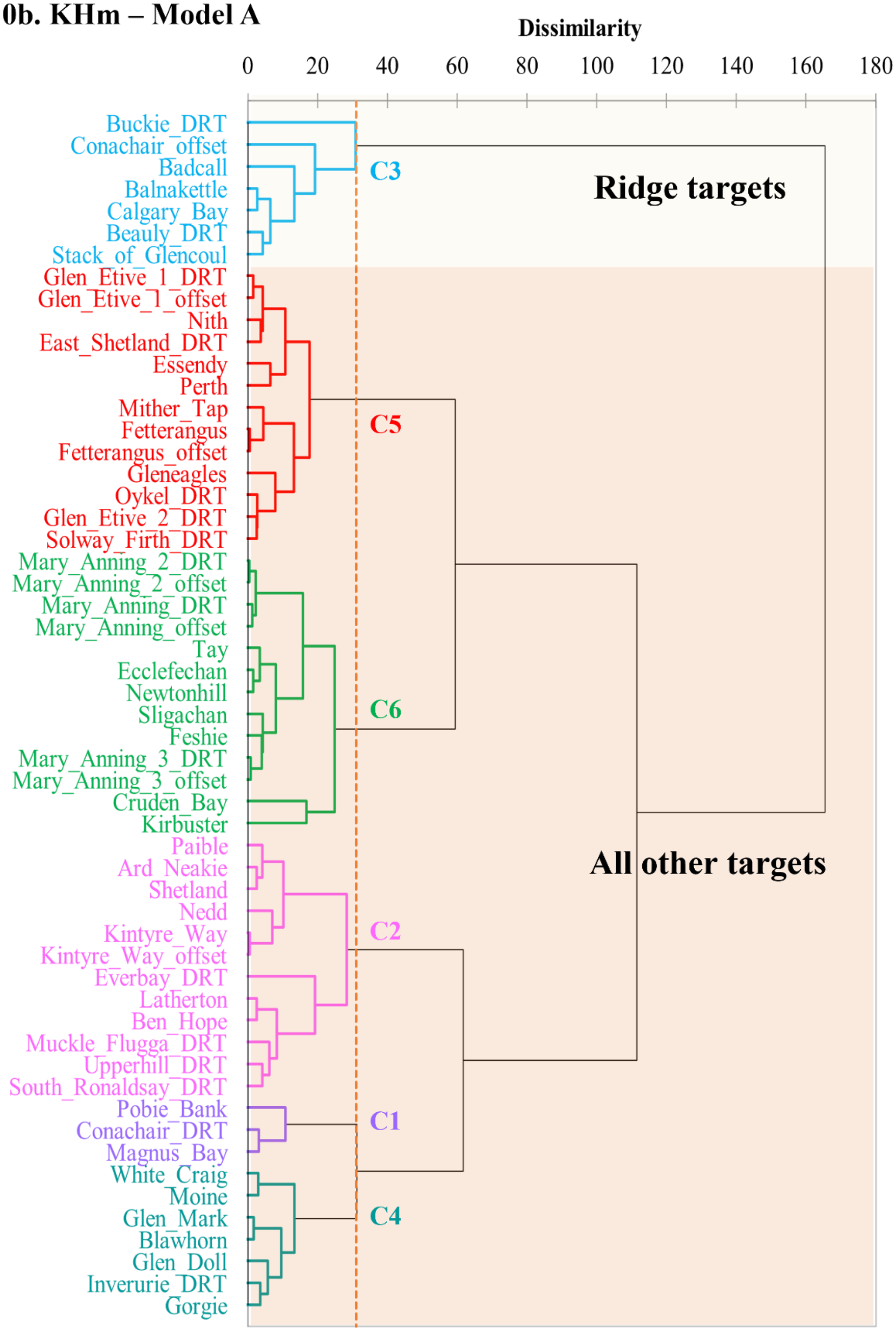

**S10c. KHm – Model B**

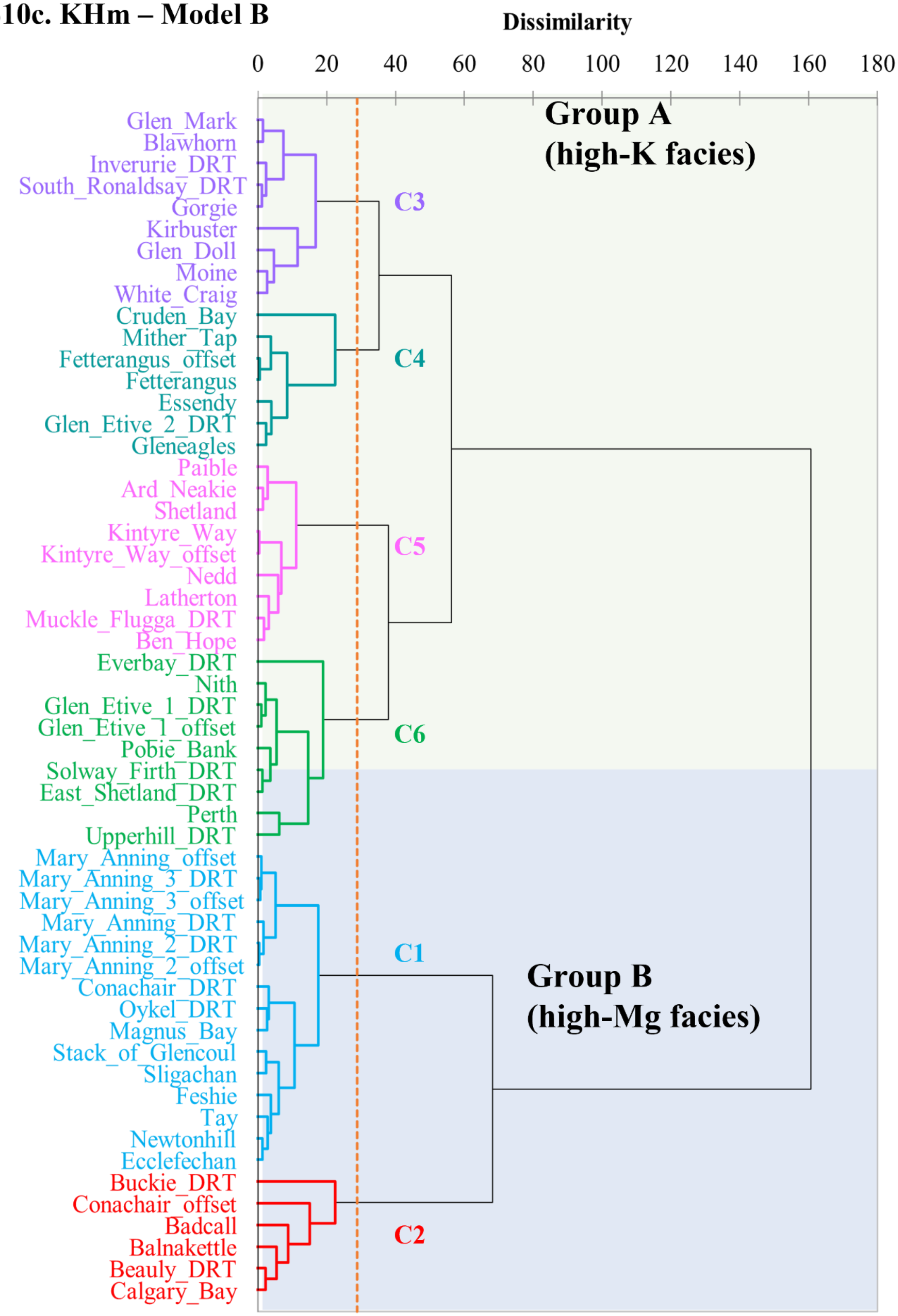

**S10d. KHm – Model C**

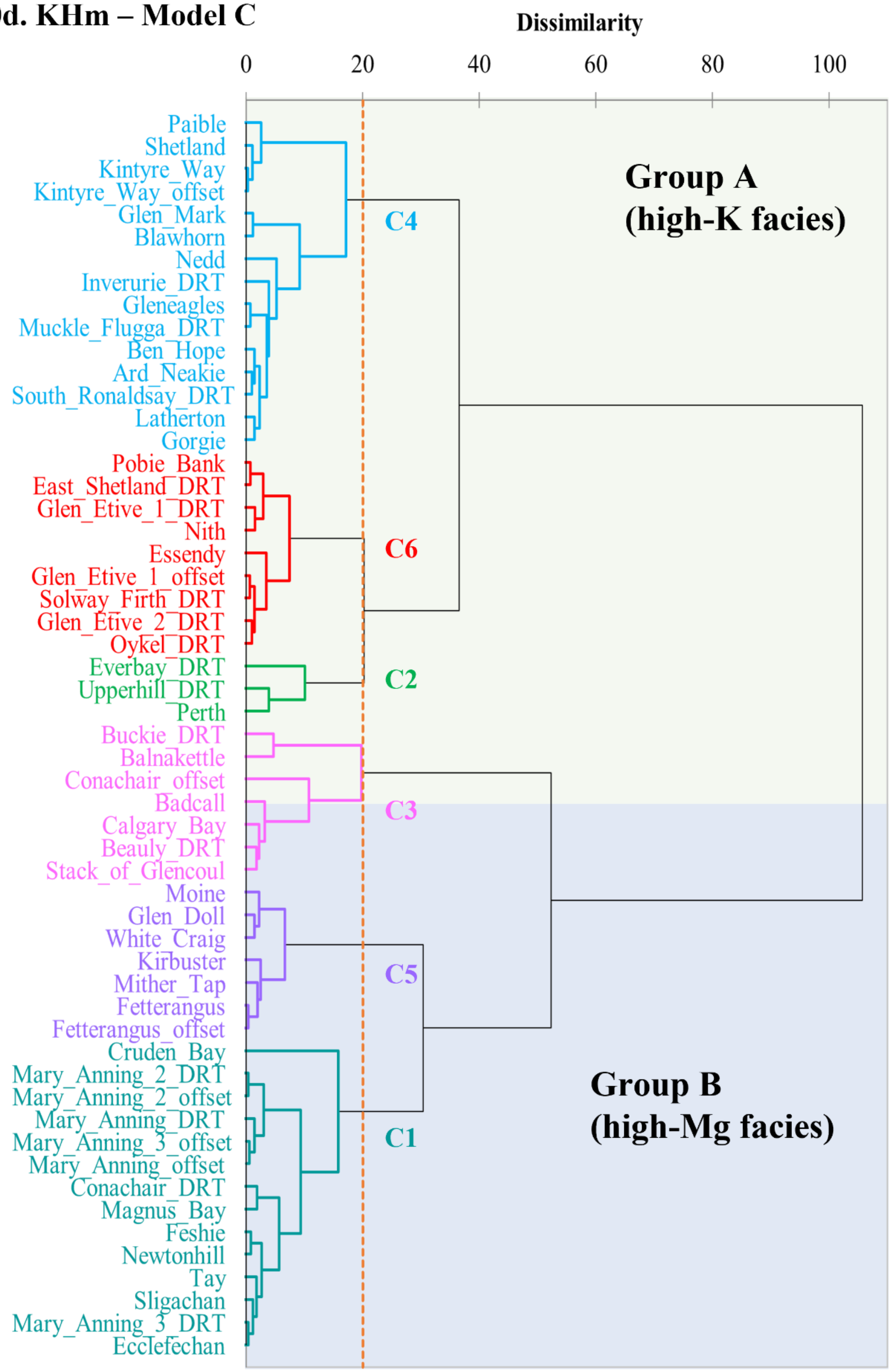

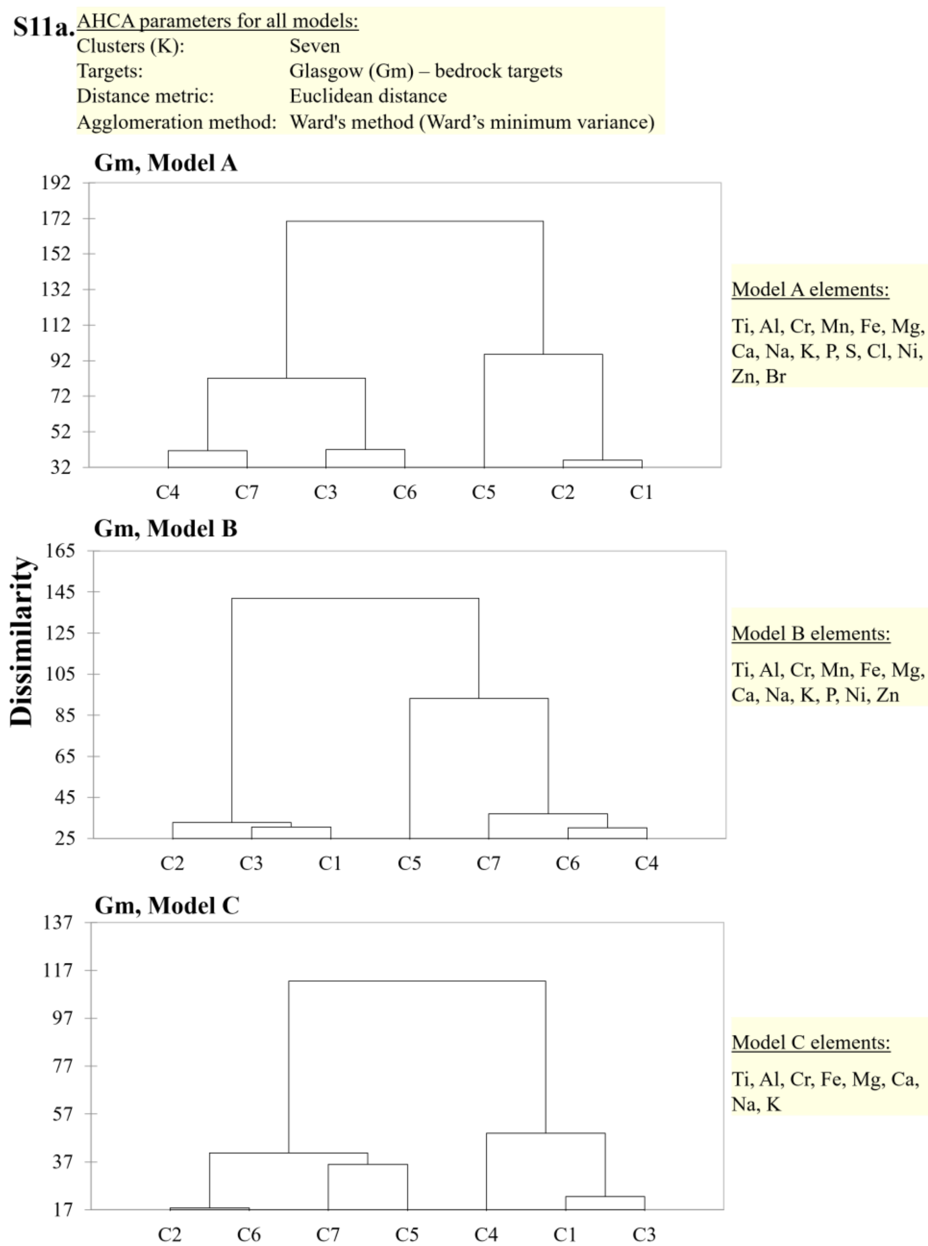


**Figure S11. Agglomerative Hierarchical Clustering analysis (AHCA) dendrograms for the Glasgow member (Glen Torridon) (n targets = 63).** All models were run using Log10 (element/Si) (mole ratios). Model parameters are discussed in Section 3.3 and Supplementary Text S2b; results are listed in Table S7a and discussed in Section 4.3.2. **S11a.** Comparison of dendrograms for Models A-C, with detailed views for each model (with target names in figures **S11b-S11d**).

**S11b. Gm – Model A**

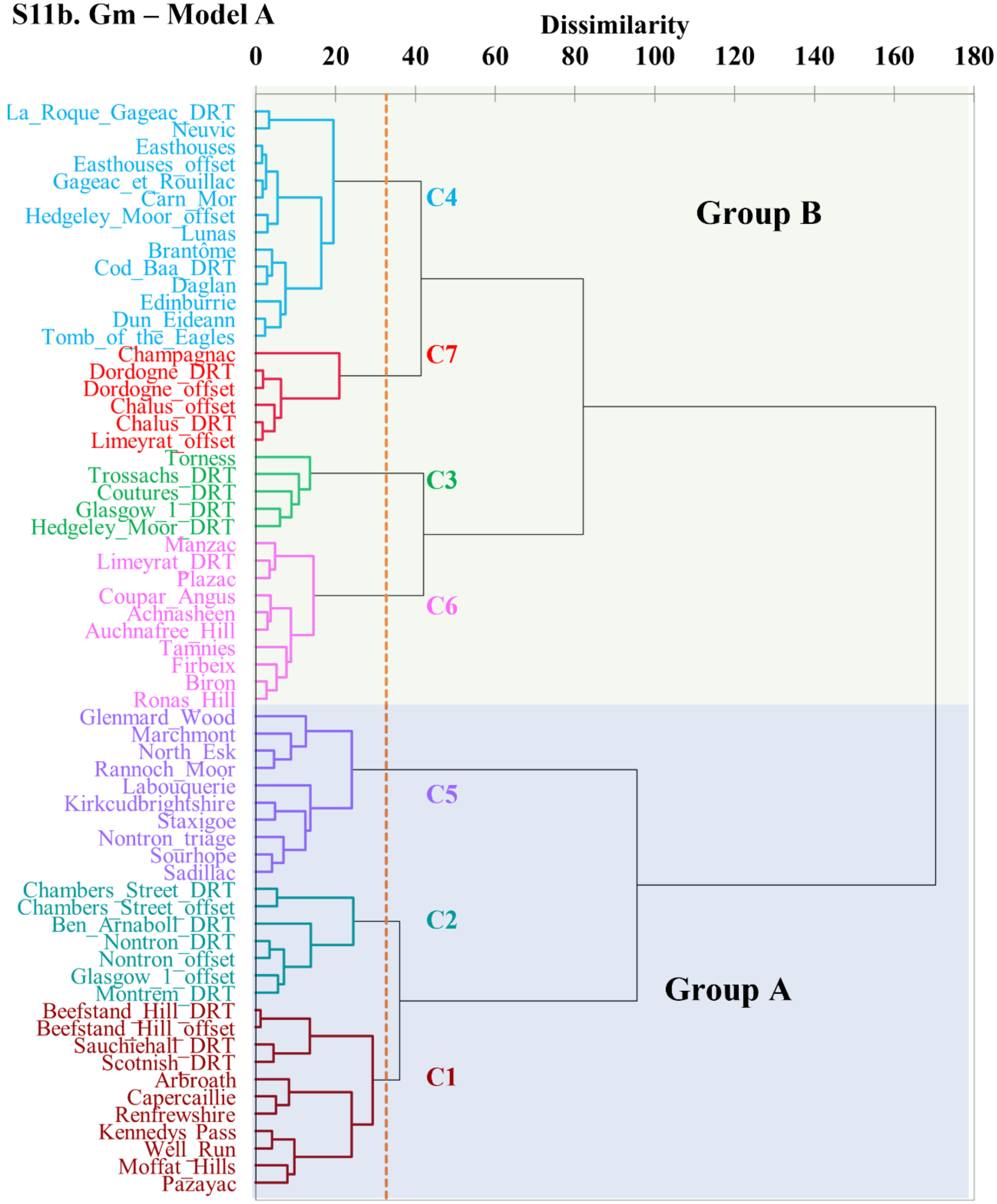

**S11c. Gm – Model B**

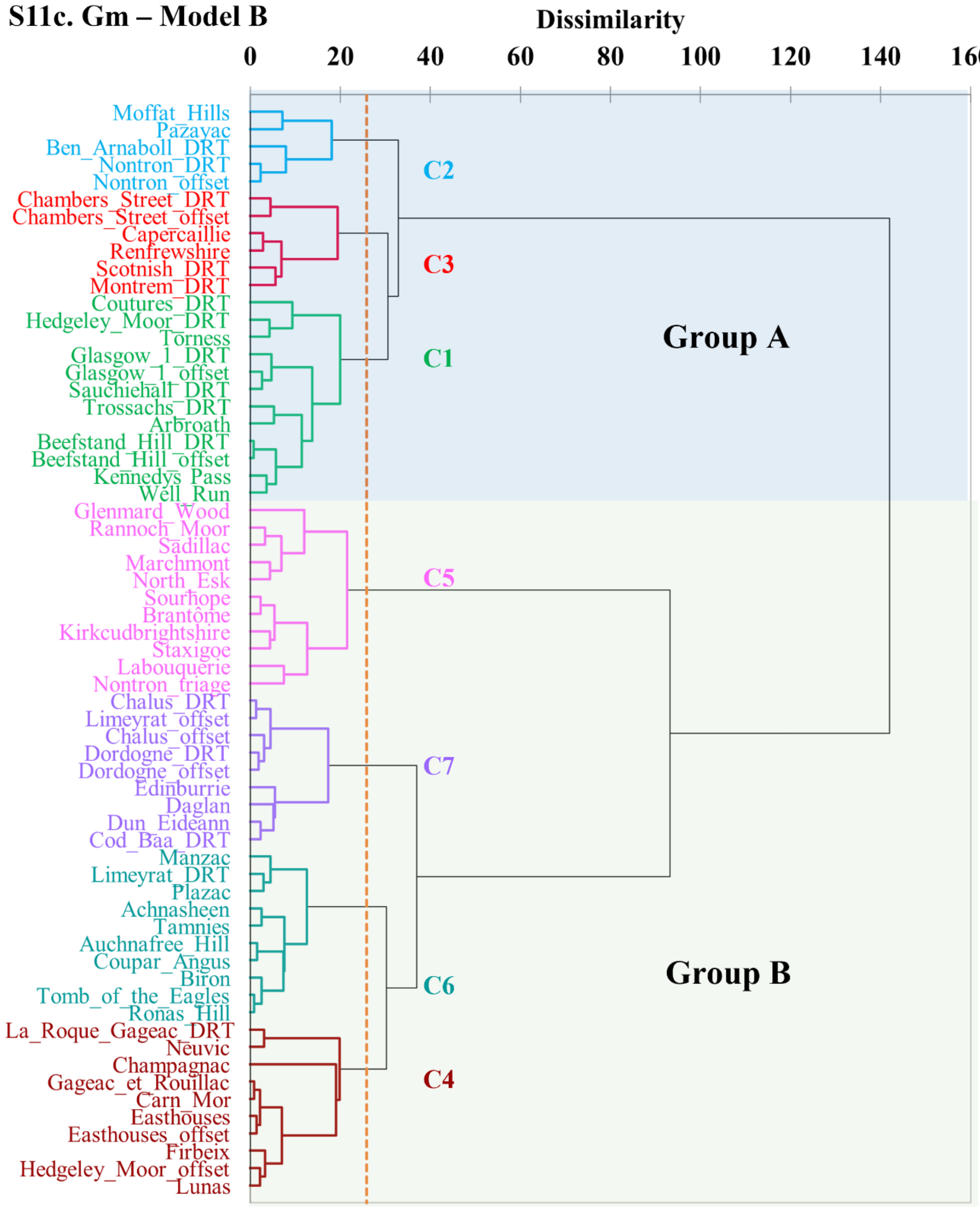

**S11d. Gm – Model C**

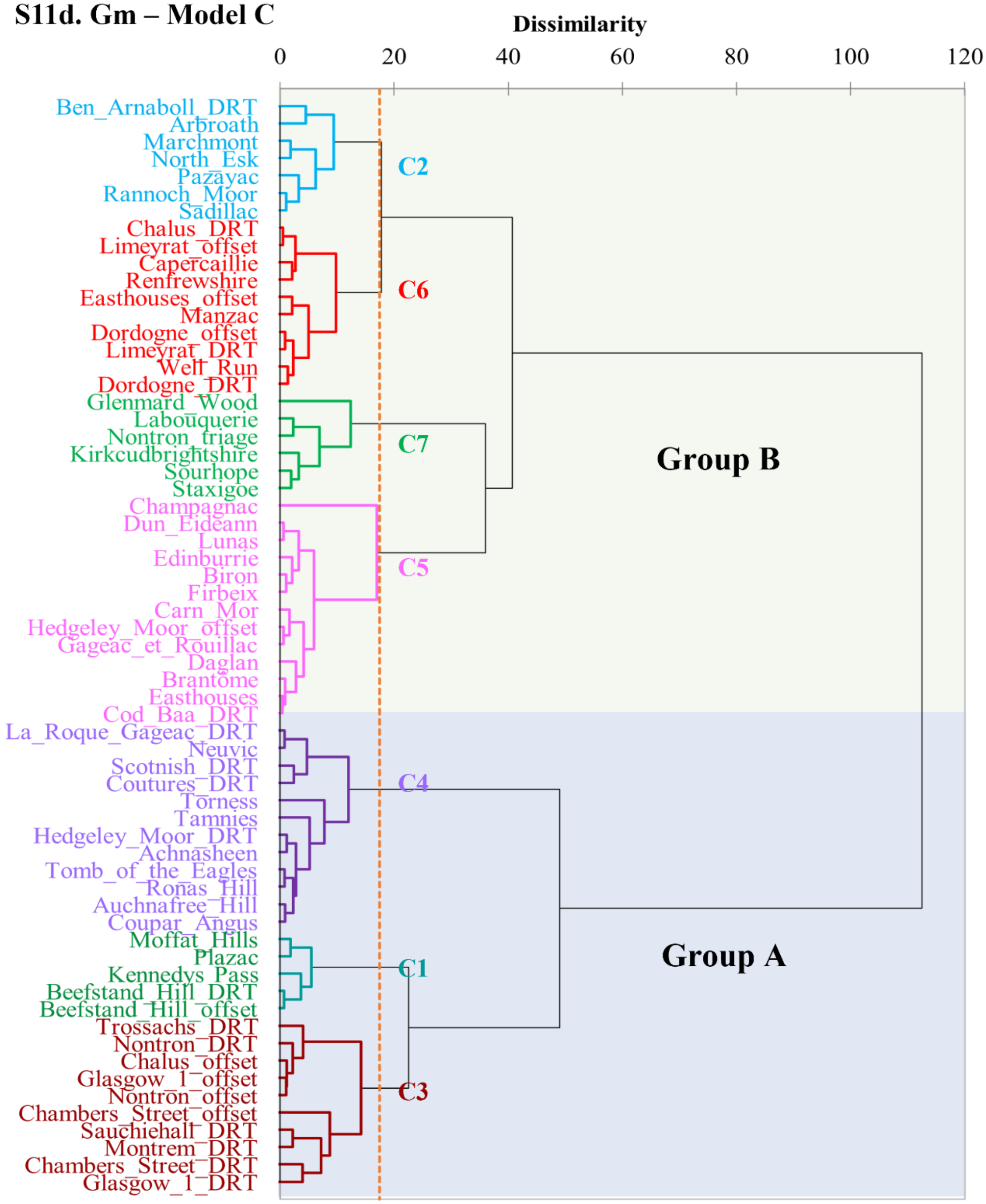

<
Tables S1-7 are uploaded separately as a single Excel file.

**Table S1.** APXS compositional data for all targets, including location information, errors and opearational statistics

**Table S2.** S2. Mean values for Glen Torridon subunits and facies, as defined in O'Connell-Cooper et al., 2022. All data (except Si molar) in element/Si (molar) form. Bedrock targets only included in mean analysis. Fines and diagenetic features (e.g., veins, nodules) are excluded.

**Table S3.** Pearson correlation coeffience (r), univariate analysis for all data. See Table S1 for full compositional data for targets within a given unit.

**Table S4.** Variance analysis, incorporating all targets included in mean Murray and Carolyn Shoemaker formations (i.e., mean Mf+CSf). Supplementary text S2a. for further details.

**Table S5.** Jura member (GT and VRR) subunit divisions, AHCA and variance analysis results. Element/Si (molar) concentrations in Table S1.

**Table S6.** Knockfarrill Hill member subunit divisions, AHCA and variance analysis results. Element/Si (molar) concentrations in Table S1.

**Table S7.** Glasgow member subunit divisions, AHCA and variance analysis results. Element/Si (molar) concentrations in Table S1.